5-2010

RANGE ADAPTIVE PROTON THERAPY FOR PROSTATE CANCER

Adam D. Melancon

Recommended Citation

Melancon, Adam D., "RANGE ADAPTIVE PROTON THERAPY FOR PROSTATE CANCER" (2010). *UT GSBS Dissertations and Theses (Open Access)*. Paper 44.

RANGE ADAPTIVE PROTON THERAPY FOR PROSTATE CANCER

by

Adam Melancon, M.S.

APPROVED:

Lei Dong, Ph.D.
Supervisory Professor

Sam Beddar, Ph.D.

Rajat J. Kudchadker, Ph.D.

Andrew K. Lee, M.D, MPH.

Uwe Titt, Ph.D

Susan Tucker, Ph.D.

APPROVED:

Dean, The University of Texas
Health Science Center at Houston
Graduate School of Biomedical Sciences

RANGE ADAPTIVE PROTON THERAPY FOR PROSTATE CANCER

A

DISSERTATION

Presented to the Faculty of
The University of Texas
Health Science Center at Houston
and
The University of Texas
M. D. Anderson Cancer Center
Graduate School of Biomedical Sciences

in Partial Fulfillment
of the Requirements
for the Degree of

DOCTOR OF PHILOSOPHY

by

Adam Melancon, M.S.

Houston, Texas
May, 2010

Range Adaptive Proton Therapy for Prostate Cancer

Publication No.: ____________

Adam Melancon, M.S.

Supervisory Professor: Lei Dong, Ph.D.

Purpose: The rapid distal falloff of a proton beam allows for sparing of normal tissues distal to the target. However proton beams that aim directly towards critical structures are avoided due to concerns of range uncertainties, such as CT number conversion and anatomy variations. We propose to eliminate range uncertainty and enable prostate treatment with a single anterior beam by detecting the proton's range at the prostate-rectal interface and adaptively adjusting the range in vivo and in real-time.

Materials and Methods: A prototype device, consisting of an endorectal liquid scintillation detector and dual-inverted Lucite wedges for range compensation, was designed to test the feasibility and accuracy of the technique. Liquid scintillation filled volume was fitted with optical fiber and placed inside the rectum of an anthropomorphic pelvic phantom. Photodiode-generated current signal was generated as a function of proton beam distal depth, and the spatial resolution of this technique was calculated by relating the variance in detecting proton spills to its maximum penetration depth. The relative water-equivalent thickness of the wedges was measured in a water phantom and prospectively tested to determine the accuracy of range corrections. Treatment simulation studies were performed to test the potential dosimetric benefit in sparing the rectum.

Results: The spatial resolution of the detector in phantom measurement was 0.5 mm. The precision of the range correction was 0.04 mm. The residual margin to ensure CTV coverage was 1.1 mm. The composite distal margin for 95% treatment confidence was 2.4 mm. Planning studies based on a previously estimated 2mm margin (90% treatment confidence) for 27 patients showed a rectal sparing up to 51% at 70 Gy and 57% at 40 Gy relative to IMRT and bilateral proton treatment.

Conclusion: We demonstrated the feasibility of our design. Use of this technique allows for proton treatment using a single anterior beam, significantly reducing the rectal dose.

Acknowledgements

First, I would like to thank my advisor, Dr. Lei Dong, for his advice, guidance, and patience throughout this project. I would also like to thank the members of my committee: Dr. Sam Beddar, Dr. Rajat Kudchadker, Dr. Andrew Lee, Dr. Uwe Titt, and Dr. Susan Tucker, whose contributions have been greatly appreciated.

Many of my work peers have contributed to my project. I would like to thank Dr. Louis Archambault, Dr. Kishore Mogatadakala, and Dr. Yong Peng, whom I consulted on various technical issues relating to my project. I would like to thank Dr. X. Ronald Zhu and Michael (Brad) Taylor for their assistance at the proton therapy center. I would like to thank all of my peers that have listened to my problems and frustrations, given me valuable advice, and supported me throughout my project.

To my friends and family, I thank you for the love and support you have shown me. And to my wife, Marites, my daughter, Sophie, you are my inspiration. With you, all things are possible.

Table of Contents

List of Figures

List of Equations

List of Tables

Chapter 1: Introduction

Prostate cancer is the most common malignant neoplasm for males in the North America with nearly 200,000 new diagnosis and over 25,000 mortalities in 2009 (1). Over the last century, prostate cancer treatment has evolved to allow curative treatment of the disease without severely affecting the patient's quality of life. Nonetheless, locally advanced and metastatic prostate cancer remains a potential lethal disease, and treatment of early stage disease can potentially recur adding a substantial monetary burden and reduction of the patient's quality and duration of life. Contemporary research aims to definitively treat disease and incur minimal treatment related side effects in a timely and fiscally responsible manner. To this end, we will begin with a brief introduction to contemporary diagnosis and treatment of prostate cancer, the evolution of external beam therapy, the relation of toxicity with uncertainty and treatment margins, the resulting advancement of proton therapy, and culminate with our proposed treatment technique to maximize the advantages of proton therapy for treatment of the prostate.

1.1 The evolution of external beam photon therapy for prostate cancer

1.1.1 Detection, staging, and modality determination

Early detection is the strongest factor for favorable disease prognosis (2). Prostate specific antigen (PSA) testing and digital rectal examination are recommended for screening prostate cancer in men over the age of 50. If the absolute level of PSA detected in the blood or the PSA level relative to a patient's previous tests is abnormally high, multiple samples of prostatic tissue are biopsied from each geographic section of the prostate. Tissue biopsy verifies the presence of the cancer, identifies the disease's location for proper tumor staging, and provides cellular samples for disease prognosis.

By examining the tissue sample from biopsy, the prostate cancer is graded according to the Gleason scoring system to indicate its level of aggressiveness and malignancy. The system ranks the two most prominent cancer cell types according to their level of cell abnormality, and then adds the two numbers to generate the Gleason score. After Gleason scoring, the disease's stage is determined with the TNM system. The TNM staging determines the progression of the disease within the organ of origin (T), the regional lymph nodes (N), and distant metastasis (M). Prostate cancer is often confined to the prostatic capsule; however the malignancy may extend into the extra-prostatic tissue, seminal vesicles, pelvic lymph nodes, and may metastasize to skeleton or brain. T2-weighted MRI and bone scans are often used to supplement CT pelvic scanning and biopsy results for proper tumor staging.

Based on the previous three tests, patients are assigned a PSA level, Gleason score, and tumor stage. From these three factors the patients are stratified according to risk. Low risk prostate cancer is defined as PSA levels of less than 10 ng/ml, Gleason scores less than 7, and T1 or T2 stage disease on only one side of the prostate. Intermediate risk cancers have slightly higher PSA levels (10-20 ng/ml) or a Gleason score of 7. Seminal vesicle invasion, a

Gleason score greater than 7, or a PSA level greater than 20 ml/ng place the disease within the high risk stratification.

Clinicians consider the disease's risk classification, the patient's health, and treatment side effects when choosing their patient's treatment modality. There are several effective treatment options for low-risk locally confined disease of the prostate including brachytherapy and radical prostatectomy. Both approaches offer a safe treatment option with an excellent chance of local tumor control. Both of these modalities have the potential to spare small critical structures that are related to the patient's urinary and reproductive function such as the penile bulb, neurovascular bundle, and urethra. However, both carry the risk of leaving residual tumor untreated, the risk of infection, and potentially delay the patient's recovery. Additionally, tumor mis-staging is not uncommon, and locally confined treatments carry the risk of mistreatment of extraprostatic disease and risk subsequent disease recurrence. For these reasons, external beam radiation therapy is often used to treat low-risk disease and is the modality of choice for intermediate and high-risk diseases. . HT is often used as an adjunct to external beam radiation therapy to ablate the tumor volume (neoadjuvant hormone therapy, NAD), relieve the patient of disease-related symptoms, reduce the overall treatment volume thus sparing normal tissue, and potentially reduce the overall stage of the disease (3). Several studies even suggest the local control and survival benefits of their combined treatment are much greater than either treatment alone (4, 5). The exact mechanism for the observed supra-additive effect of combination radiotherapy and hormone therapy is a topic of debate, however some in vitro evidence suggests that hormone therapy may potentiate cell death following curative level of radiation dose by enhancing the cellular apoptotic pathway (6). Our in-house study demonstrated the dosimetric advantages of post-NAD treatment planning and the risk of treating based on pre-NAD treatment images (Figure 1).

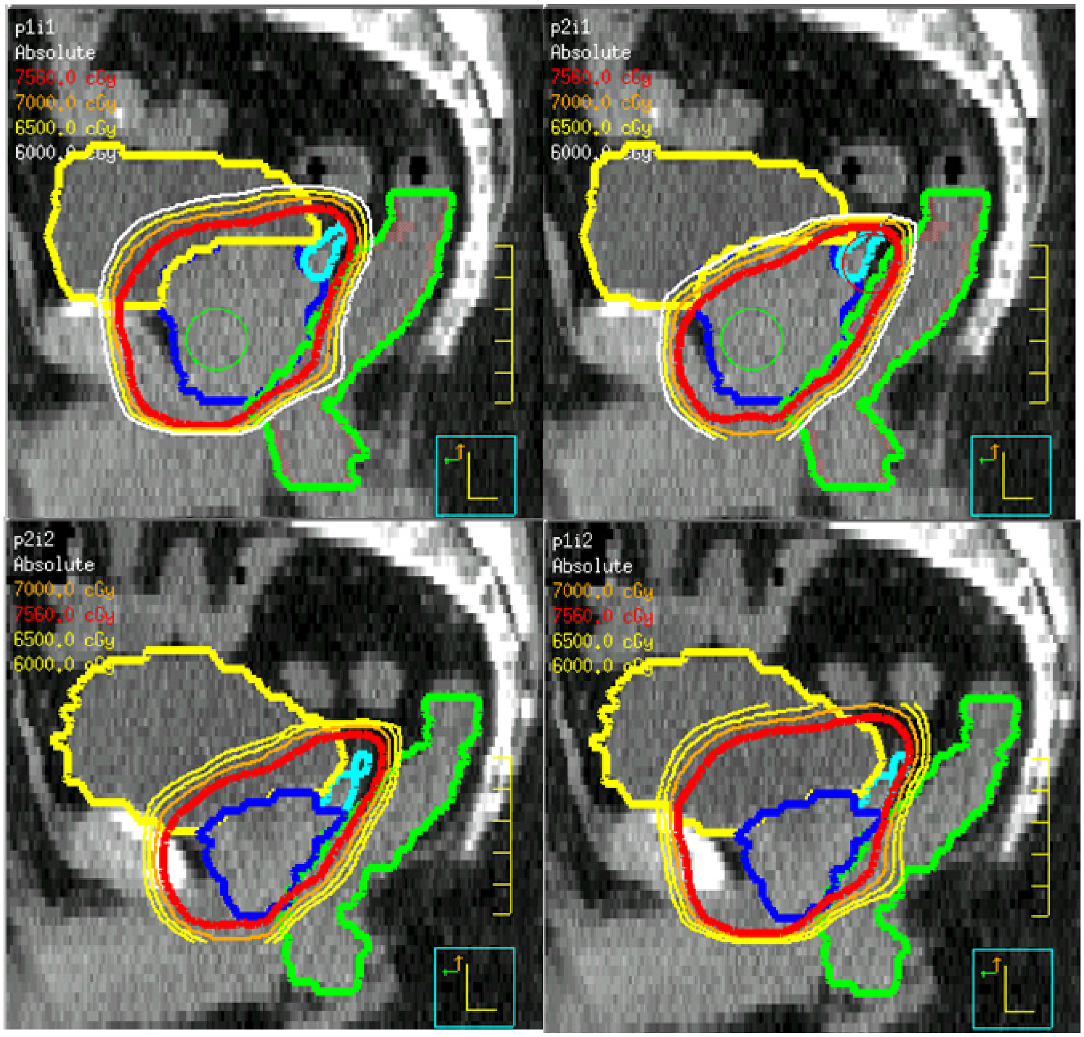

Figure 1: NAD-induced target volume reduction and the importance of treatment planning after HT.

The top left of Figure 1 illustrates the pre-NAD plan on the pre-NAD anatomy. The top right shows the same plan applied to the anatomy after 108 days of NAD resulting in increased bladder dose with little change of the rectal and bladder volumes or the rectal dose. The bottom left illustrates the post-NAD plan on the post-NAD anatomy. The bottom right shows the post-NAD coverage of the pre-NAD tumor bed. Areas of both the prostate and SV were not treated to the full prescription dose. Pre-NAD planning does not ensure coverage despite its large treatment volume.

1.1.2 Dose-escalated radiotherapy, toxicity, and treatment margins

The escalation of dose to target organs was one of the first and most critical steps to definitive radiotherapy of advanced prostate carcinoma (7). Early retrospective studies of dose escalation (8, 9) without the benefit of conformal technologies indicated that escalated radiation dose may improve survival in advanced cases. The early Phase I single institution clinical trials of Hanks et al (10) and Zelefsky et al (11) showed an increased biochemical freedom from relapse (BNED) among high-risk patients. The Phase III clinical trial by Pollack et al. (12) showed an improvement in freedom from failure (FFF) within the dose escalation arm, however this particular study was not sufficiently powered to demonstrate efficacy of dose escalation in low-risk patients. A more recent study demonstrated escalation to 79.2 Gy from 70.2 Gy, halved the risk of biochemical recurrence in 393 patients with disease staged T1b-T2b and PSA levels less than 15ng/ml (80.4% vs. 61.4% BNED)(13). These studies demonstrated the benefit of treating with higher dose, even in low-risk disease, to reduce disease recurrence. Survival advantage was difficult to establish in short term studies with low-risk patient population. However, local control of prostatic disease has shown to reduce metastatic dissemination(14) and subsequent metastasis-free survival(15, 16).

Unfortunately, high dose treatment arms in early non-conformal dose escalation studies resulted in severe rectal complications (17-19). Rectal late effects included many factors including bleeding, incontinence, diarrhea, oily discharge, colic, and increased voiding frequency. Non-IMRT dose escalation trials demonstrated an approximate 2-fold increase in Grade 2 and 3 late rectal toxicity including two trials with greater than 26% incidence (11-13, 20). A few of the early trials found correlation of dose with late bladder toxicity (18, 21, 22); however, most of the following clinical trials found similar bladder toxicity in escalated and non-escalated treatment arms (12, 13, 23).

The efficacy of dose escalation and the corresponding risk of morbidity for all disease sites was the impetus for the development of modern conformal radiotherapy. While two dimensional computer calculations and dose models were available in the 1960's, the development of computed tomography (CT) and the introduction of the beam's eye view (BEV) concept in the late 1970's and early 1980's let to the development of the first three-dimensional treatment planning system (24). 3DCRT treatment included physical collimation with cerrobend or lead blocks attached to the head of the gantry, new plan evaluation tools such as the dose volume histogram (DVH), and new biological effect models such as tumor control probability (TCP) and normal tissue complication probability (NTCP). These advances improved the therapeutic ratio and allowed, to some extent, dose escalation without severe adverse effects to surrounding critical structures.

The emergence of intensity modulated radiation therapy (IMRT) began with the development of the multi-leaf collimator (MLC). With the MLC, collimation could be dynamically changed or segmented to create non-uniform beam intensities. New software developments enabled treatment-planning systems to optimize the beam intensity according to desired dose distribution input by the user. These advances led to greater conformation of the treatment field to the tumor (25) and further reduced rectal and bladder dose during therapy (26, 27). The highly conformal dose distributions achievable with an IMRT system made treatment planning highly sensitive to target position uncertainties (28-30), which led to a need to characterize, immobilize, and localize the target organs during radiotherapy.

Conformal radiotherapy technologies required a new set of nomenclature to describe volume-based treatment. ICRU Report 29 was published in 1978, defining a target volume that included gross tumor, movements, variations, and uncertainties in treatment (31). The advent of CT simulation and computer technology prompted ICRU Report 50, which split the target into 3 parts, the GTV, CTV, and PTV (32). The GTV included the gross tumor volume, the clinical target volume (CTV) included the GTV plus uncertainty in microscopic spread, and the planning target volume (PTV) included the CTV plus geometric (patient movement and setup) uncertainties. ICRU Report 62 was published in 1999 as a supplement to ICRU Report 50(33). This report refined the definition of the PTV by segregating the single PTV expansion into two expansions of the CTV, one for organ motion and one for patient set-up and other uncertainties (34).

1.1.3 Treatment uncertainty and its management

Although the ICRU defined the nomenclature used in radiotherapy, the clinical and research community was still responsible for determining the uncertainty values and the corresponding treatment margins to apply. The three primary sources of uncertainty in photon radiotherapy are target volume delineation, setup error, and organ motion. Since these sources are independent, the total target uncertainty is approximately the square root of the quadratic sum of each source. The composite treatment uncertainty is used to calculate the proper treatment margins to ensure coverage of the treatment target with a specified statistical confidence, usually 95%. Since the relative amount of dose the normal tissues receive during treatment and the confidence of target coverage are directly related to the size of the treatment margins utilized, much of contemporary medical physics research is aimed at the reduction of treatment uncertainty to improve the therapeutic ratio of treatment (35).

Treatment uncertainty begins with delineation of the disease volume. Several factors contribute to the uncertainty in target delineation beginning with the limitations of the imaging device (36). Many imaging modalities have limited spatial resolution particularly in the direction perpendicular to the slice plane. Anatomic information within the coarse voxel is averaged leading to a partial volume effect. The process of target delineation, i.e. contouring, is also a major source of uncertainty. Repeat contouring of a single physician or contouring differences between physicians can greatly affect both treatment planning and dose reporting in radiotherapy. The most common ways to manage target delineation uncertainty is with the use of functional imaging (PET, MRI, etc.) co-registered and rendered into CT for improved target definition or the use of automated delineation, or “segmentation” tools, to improve the consistency of target definition.

Setup uncertainty involves registration of the external surface of the patient, the room, and the treatment couch. Patient set-up is achieved with the use of external immobilization for proper registration of treatment with the patient’s external anatomy and for reduction of the patient’s movement during the treatment. Some of the more common external immobilization devices include the body cradle, thermoplastic shells, knee wedge, and Vac-Lok bag (37-40). These devices are made of foam or plastics that tightly conform to the patient’s body, immobilizing them during treatment.

Even with careful immobilization and alignment of the patient, significant changes occur because of the non-rigidity of anatomy, bowel gas movement, feces, and the variable filling of the bladder (41-43). Some institutions attempt to control the fullness or emptiness of the rectum during treatment, and most institutions treat with a full bladder to improve dosimetry of the bladder wall and the small bowel and to potentially immobilize the bladder. Although rectal and bladder filling induced treatment uncertainties are less when treating patients in the prone position, most institutions elect to treat in the supine position to minimize treatment uncertainty caused by respiratory motion (44, 45). Organ motion is categorized into motions that occur between fractions, interfractional motion, and those that occur during the fraction, intrafractional motion. Previous studies indicate that interfractional motion is the greater of the two types of motion (45), which is fortunate because it is simpler to manage.

One method for the management of interfractional motion is image-guided target localization. In traditional clinical practice, patient positions are adjusted based on periodic portal imaging. This localization device consists of a flat-panel detector attached to the gantry of the linear accelerator, allowing for convenient megavoltage x-ray imaging of the patient in the treatment position. Many corrective and adaptive procedures have been developed for improving treatment quality including offline correction to the patient's bony anatomy, online correction of the patient in conjunction with implanted fiducials, and the monitoring of motion for future planning adaptation. The disadvantages of the EPID include poor soft tissue contrast and the lack of proper three dimensional tissue density information needed for the recalculation of dose. Because of poor soft tissue contrast of kilo- or mega-voltage x-rays, bony landmarks are generally used for patient setup. However, bony landmarks do not accurately represent the positions and shapes of the target and normal tissues. Implanted radio-opaque markers may improve registration of the treatment to soft tissue targets such as the prostate, however, they may exhibit migration or positional instability when organ shape variation occurs (46, 47). For these reasons, many manufacturers have moved to more advanced on-board technologies that address these limitations (48).

Current clinical practice for prostate radiotherapy also includes the use of trans-abdominal ultrasound systems (49-51). The ultrasound system sends and receives sound waves, which are used to identify the tissue interfaces between organs for daily target localization. However, inter- and intra-user variability in the operation of ultrasound devices (52), the inherently poor quality of ultrasound images, and anatomic distortions resulting from the pressure on the abdomen (50) reduce the effectiveness of these devices.

An alternative to target localization techniques are internal immobilization devices. These manage both interfractional and intrafractional motion by stabilizing the volume of the rectum and bladder. There are a wide variety of internal immobilization devices for the pelvic anatomy, yet the most common are catheters, enemas, and balloons. Catheters are used to control the volume of the bladder, ensuring that the prostate receives the prescribed dose and that the bladder and small bowel remain out of the high dose region. Rectal balloons and enemas are used to control rectal filling. An enema empties the rectum of feces and reduces the generation of gas in the upper bowel. Rectal balloons help maintain a constant rectal volume during treatment in addition to pushing the lateral and posterior rectal walls away from the radiation. These may help in controlling internal soft tissue variations(53-57), however, residual target motion may still compromise a patient's daily treatment fraction ,.

The most precise forms of contemporary target localization are those that utilize on-board kilovoltage volumetric imaging for precise daily image-guide set-up such as “cone-beam” CT (58) and the “CT-on-Rails” (59). Cone-beam technology utilizes a point x-ray source and a flat panel detector to reconstruct three-dimensional objects. The “CT-on-Rails” system is a CT-linear accelerator combination treatment system that allows for daily diagnostic quality CT tumor localization without removing the patient from the treatment couch. Both allow for daily target registration with millimeter precision, however, both methods are limited by delineation uncertainty, target deformation, and intrafractional anatomic variation.

Our in-house studies of intrafractional prostate motion addressed the limitations of on-board CT imaging for daily correction of treatment uncertainties (60, 61). We observed anterior and inferior displacement of the target organs strongly correlated with gaseous build-up of the rectum ($P<0.001$) in a cohort of 46 prostate cancer patients (Figure 2). The top of figure 2 illustrated an axial slice of the patient’s anatomy near the base of the prostate and the proximal seminal vesicles. The arrows indicated the deformation of the patient’s pelvic anatomy to the image of the patient’s post-fraction CT (bottom). The rectum expanded shifting prostate and proximal SV anteriorely and superiorly. The mean time interval in between CT image acquisitions was 21 minutes. One standard deviation of anterior displacement was 2.9 mm and 4.1 mm for the prostate and seminal vesicles respectively. One standard deviation of intra-user contouring uncertainty was 0.9 and 1.3 mm anteriorely for the prostate and SV and 1.4 and 1.7 mm inferiorely for the prostate and SV respectively. These results suggested that our current margins do not completely correct for variations of the target during treatment and warranted further investigation.

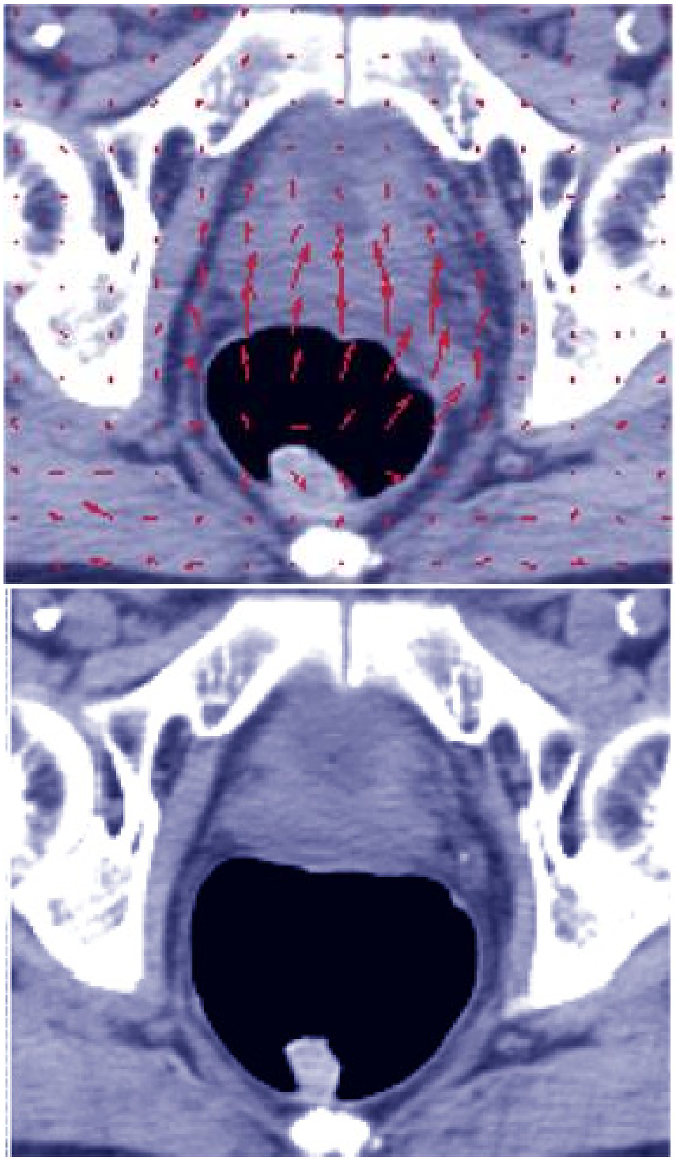

Figure 2: Intrafractional gaseous build-up in the rectum.

To test the sensitivity of prostate IMRT to intrafractional variations, we simulated patient treatment on a CT obtained before the patient's daily treatment fraction and applied this plan to their post-fraction anatomy. We used a three-millimeter internal target volume, ITV, based on the results in our first study and approximation of our current clinical margins that address intrafractional organ motion. Of 46 patients treated to 75.6 Gy, 3 patient's prostates and 8 patient's seminal vesicles were not covered at the 70 Gy isodose level (92.5% of prescription). An example is shown in Figure 3. The top of figure 3 illustrates the deformation field of the pre-fraction anatomy onto the post-fraction anatomy in the pelvic. Gas migration along with bladder filling has pushed the target organs (PTV (blue), prostate (red), SV (orange)) anterior and superior to the 60 Gy isodose and deformed the shape of the target.

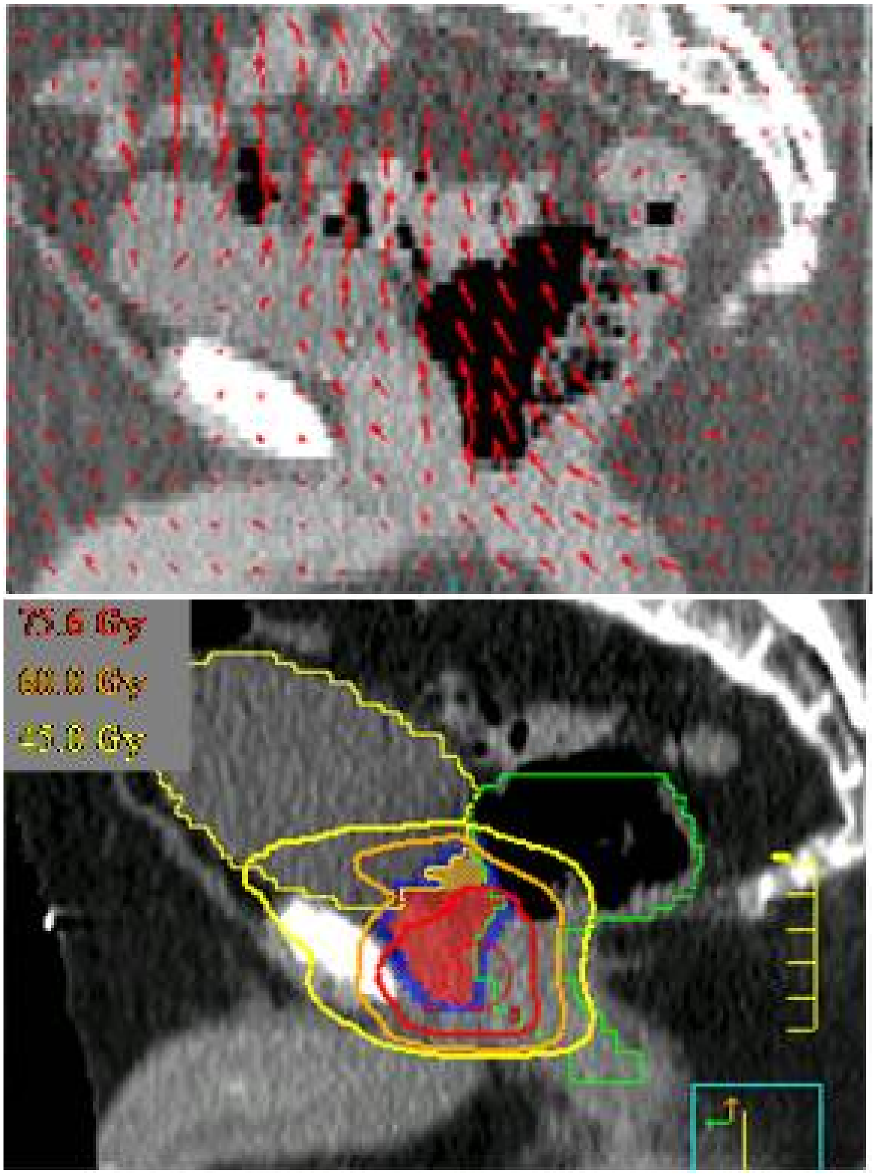

Figure 3: Intrafractional prostate deformation and resultant treatment fraction.

This study addressed the theoretical limits of what sophisticated on-board imaging can achieve if used daily before a treatment fraction. Thus, the treatment margins and resulting therapeutic ratio of external beam radiotherapy for the prostate has approached a limit of approximately 3 mm. Further improvement would be extremely difficult without radically improving the way the prostate is treated. These limitations have contributed to the development of proton facilities world-wide to further spare normal tissue and improve treatment effectiveness.

1.1.4 Summary: The evolution of external beam photon therapy for prostate cancer

Prostate cancer patients and their physicians may elect numerous ways to treat prostate cancer, but external beam photon therapy has evolved as a favorable choice for low risk disease and the preferred choice for intermediate and high risk diseases when combined with neoadjuvant or concomitant hormone therapy. Early dose escalation trials with 3DCRT led to unacceptable morbidities of the rectum and bladder. These treatment morbidities led to the development of IMRT. Modern conformal radiotherapy was more sensitive to treatment uncertainty and required new treatment margin definitions. Additional technologies were developed to reduce target delineation, patient set-up, and organ motion uncertainties and therefore reduce margins and improve the therapeutic ratio of treatment. These technologies included multi-modality imaging, segmentation tools, external immobilization devices, two dimensional image-guided localization, internal immobilization devices, and volumetric image-guided target localization. Even with daily image-guided target localization, residual uncertainties limited further reduction of margins and improvement of external photon beam treatment of prostate cancer. These limitations contributed to the development of proton facilities world-wide to potentially further spare normal tissue and improve treatment effectiveness.

1.2 The development of modern proton therapy for prostate cancer

1.2.1 Advantage of protons to spare normal tissues

The reduction of inter-fractional motion and set-up uncertainty in external beam photon radiotherapy has led to the reduction of treatment margins, the ability to escalate target dose for improved local control of disease, and the reduction of normal tissue doses adjacent to the target organs. However, the therapeutic ratio of external beam photon therapy is ultimately limited by the physics of photon attenuation as the photon beam enters, irradiates, and exits the patient's body. The depth dose of photons rises abruptly upon entering the patient and reaches a maximum when the number of charged particles entering a volume is equivalent to those ionized that exit the volume, a condition known as electronic equilibrium. This depth can be as great as three centimeters in the case of 18 MV photons. Photons attenuate en route to the target volume, resulting in considerably less absorbed dose inside the target. Photons then pass though the distal portion of the patients anatomy relatively unimpeded, resulting in further irradiation of normal tissues as they exit the patient. Therefore, clinicians utilize multiple beams to spread entrance and exit photon dose over a large volume of normal tissue. Clinicians assume that these tissues can tolerate a moderate dose and patients will experience few or no adverse effects as a result of their treatment.

In the 1940's, Robert Wilson suggested that proton therapy dose distribution might result in superior treatment for cancer patients (62). Therapy with charged particles can circumvent some of the limitations of photon radiotherapy treatment. Protons deliver the majority of their dose at the Bragg peak near the distal end of the beams range. The normal tissue dose is reduced proximal to the target and eliminated just millimeters distal to the target. Therefore, proton therapy offers a theoretical advantage over photon therapy for reducing the irradiated volume of non-target tissues. Additionally, the distal falloff of a proton beam is considerably sharper than the lateral penumbra of a photon beam, theoretically allowing for rapid dose falloff near adjacent critical structures (63).

1.2.2 Proton delivery technology

Passively scattered proton delivery relies on many technologies to deliver conformal treatment to the entire tumor volume. The first technology is the scattering foils which turn a proton pencil beam into a flat field of uniform fluence at the surface of the target (Figure 4). The first scattering foil spreads the beam resulting in a wide field with Gaussian fluence. The second scattering foil flattens the fluence by scattering protons near the center of the field. The distance between the first and second foil, second foil and patient, and the lateral scatter of the protons results in a beam of uniform fluence for a specified source to surface distance (SSD).

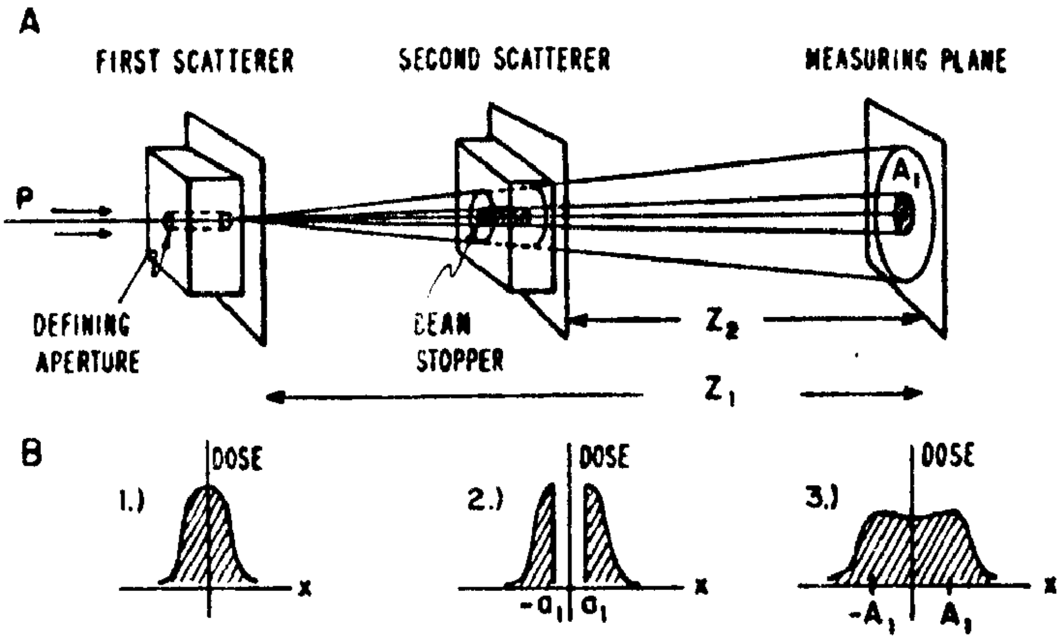

Figure 4: Dual scatter design to generate a large flat field, (64)

The second technology is the range modulator. The range modulator is a rotating wheel with varying thickness (steps) of attenuating material that degrades the initial proton energy to cover the target uniformly from its proximal to distal end (Figure 5). The relative weighting of each of the Bragg peaks is computed to generate a uniform treatment of a tumor volume. The sum of these degraded peaks is termed, the spread out Bragg peak (SOBP). The proper SOBP width is achieved by gating the proton beam with a specific window of thickness on the rotating wheel. The same range modulation can be achieved with spot-scanning systems by directly varying the initial energy of the beam and weighting these beams appropriately.

Figure 5: Range modulator wheel

The third technology that allows for conformal proton delivery is range compensation. Range compensation corrects for the shape of the patients surface, tissue inhomogeneites in the beam's path, and the shape of the distal target volume. The compensator achieves conformal treatment by degrading the beam along each ray path to precisely match the distal end of the target volume (Figure 6). In the absence of heterogeneity along the proton beam-path, the compensator shape will closely match the shape of the distal edge of the target. The compensator in figure 5 is much thinner in the area upstream from the high-density structure to correct for its relatively high radiological thickness.

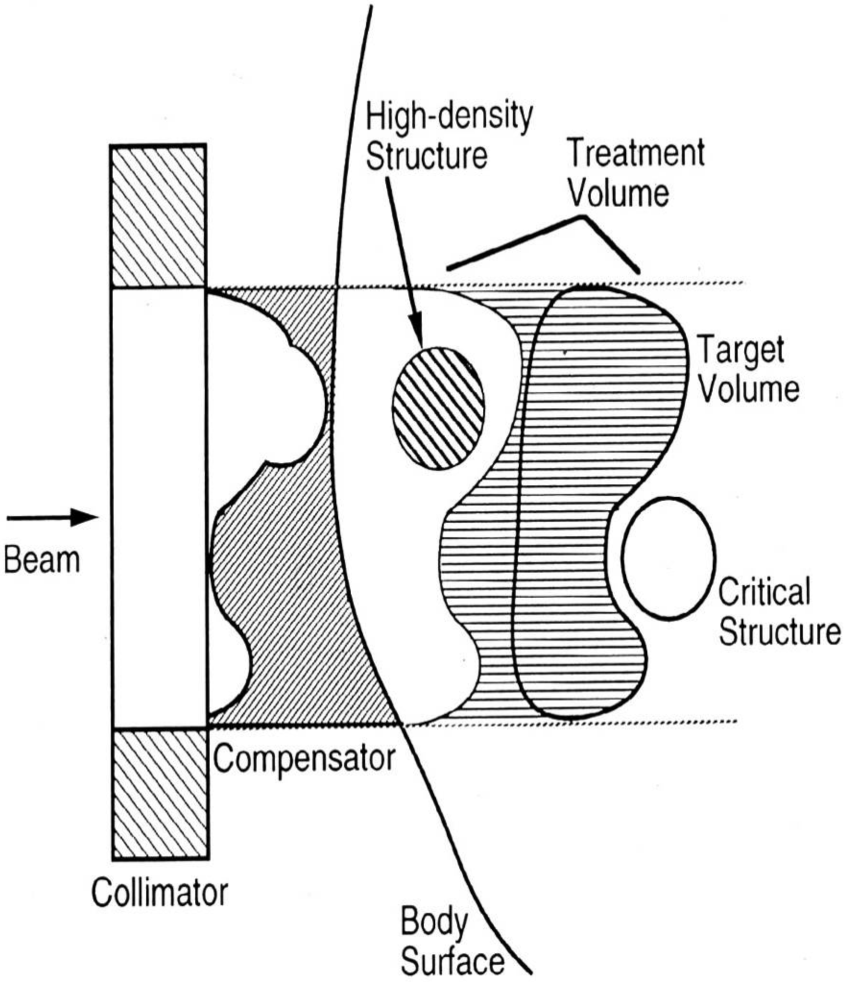

Figure 6: Range compensation for conforming a proton beam to the distal target, (65)

1.2.3 Proton range uncertainty and its management

Since protons deliver their energy over a relatively short area and their range is highly sensitive to variation in density and proton stopping power along the path of the beam, management of all set-up and organ motion uncertainties are critically important. One type of range uncertainty is caused by variation of tissue heterogeneities, usually air or bone, in the direction perpendicular to the beam path. Since the range compensator is unique for each beamlet, variation in the radiological pathlength to the distal edge of the target will result in a variation in the proton range and either a loss of dose in the target or unnecessary dose to distal normal tissues.

In the case of prostate treatment, femur and femoral head rotations have typically been neglected in positioning studies for prostate cancer patients because their impact on patient dosimetry is minimal for photon therapy unless they result in geometric translation of the pelvis or internal pelvic organs. However, femur and femoral head (FH) rotations may be critical to treatment uncertainties in prostate proton radiotherapy. We performed an in-house study to investigate the variation of the femur and femoral heads during treatment and its effect on bilateral proton treatment (discussed fully in Appendix B). The range defined by the Bragg peak in proton therapy is roughly proportional to the radiological path length in the beam path. Range uncertainties in the bilateral proton therapy of the prostate can potentially compromise the distal coverage of the target. In addition, dense bony structures, such as the femur and FH, in the beam path can also cause uncertainties in dose distributions because the Bragg peak becomes degraded (66). This degradation, in turn, affects the final dose distribution (67). Hence, depending on the type of immobilization device used, changes in daily patient setup during the course of proton radiotherapy could introduce varying amounts of bone in the treatment field due to FH rotation.

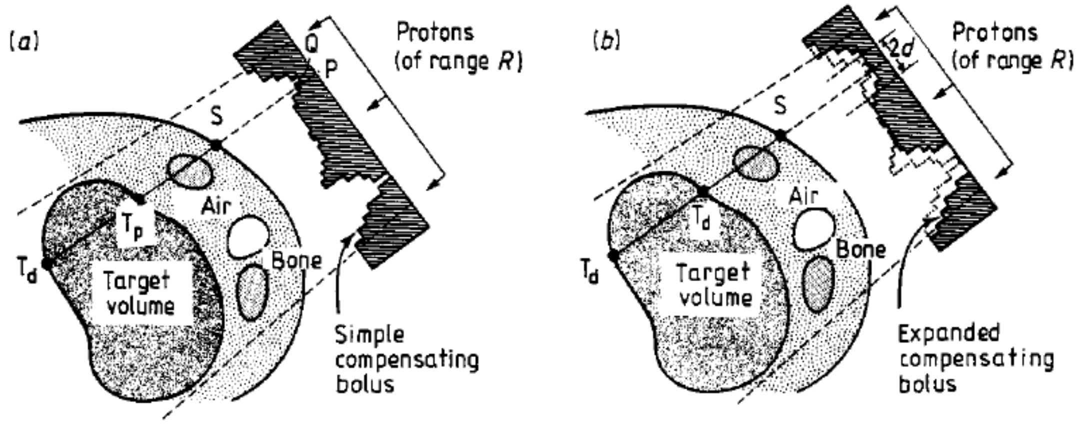

Figure 7: Smearing of a range compensator (68)

It should be noted that in proton radiotherapy “smearing” (68, 69) is typically applied to the range compensator design in an attempt to resolve the range uncertainty (Figure 7). Range compensators are used in proton radiotherapy to conform the distal edge of each beam to the target while accounting for the heterogeneities along each beam path. With the appropriate application of smearing in the design of each compensator, the changes in radiological path length resulting from tissue motion should not lead to insufficient proton penetration, thus maintaining distal coverage of the target. However, compensator smearing is usually two-dimensional and orthogonal to the beam path, so a significant anatomical rotation may not be fully compensated. To illustrate this, we designed a single lateral proton beam plan with the greatest rotational misalignment found in our study (Fig. 8). Figure 8 (a) shows the reference CT image set and plan in colorwash (top) and linear (bottom) isodose lines. Figure 8 (b) shows the reference plan recalculated on a daily CT image set in the Eclipse treatment planning system (Varian Medical Systems, Palo Alto, CA). We found that the typical 6.6-mm smearing in our routine proton plan for prostate treatment did not preserve the dose coverage in this case: The dose coverage for the prostate dropped from 75.6 Gy (prescription dose) to only 60 Gy. While a single fraction of treatment with the misaligned FH may not have clinical impact, a large systematic error in FH position would present a problem. It is worth mentioning that the dosimetric impact of FH/femur position in proton therapy cannot be resolved by simply using image-guided setup techniques. Range uncertainties due to daily radiological path length variations require the design of better immobilization devices or range verification to ensure accurate delivery of prescription dose to targets.

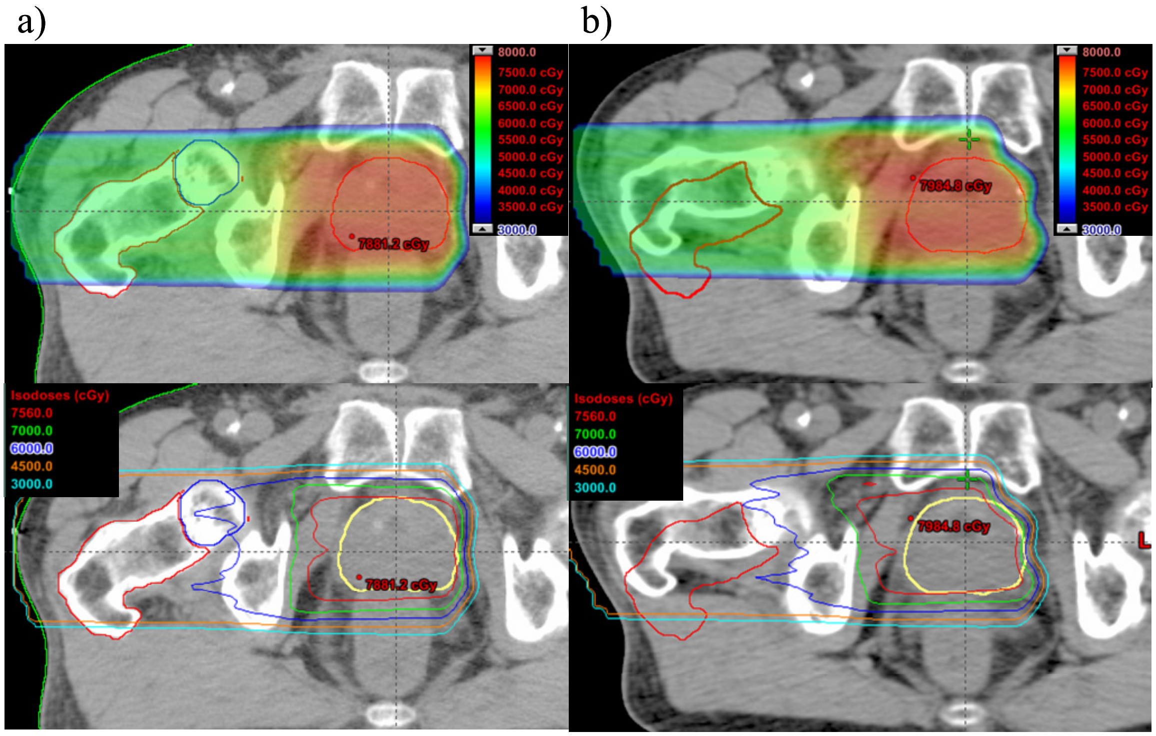

Figure 8: Changes in dose distribution after a 20-degree femoral head rotation.

Another type of range uncertainty is caused by uncertainties in determining the relative stopping power ratios for various tissue from CT Hounsfield units (HU). CT reconstructs the photon linear attenuation coefficient at each voxel within the patient. The measured HU is then used to determine the electron density of the material. Even in homogeneous material, variation in the HU can be 1 to 2% (70) and up to 3% depending on the location within the phantom (Moyers 1993). The proton stopping power is then approximated from the estimated electron density. This approximation is usually accomplished with a stoichiometric calibration method with tissue equivalent materials described by Schneider et al (71). Even with rigorous calibration of CT to approximate proton stopping power, uncertainty in the calculation of the proton's range persists. If the stopping power ratio is questionable or the water-equivalent path length varies, the proton beam may not stop at where you think when designing the proton treatment. Thus, we apply a generous margin, 3 and one half percent of the protons total range plus 3 millimeters, to account for the uncertainty in range calculation from CT Hounsfield units (69)(Figure 9).

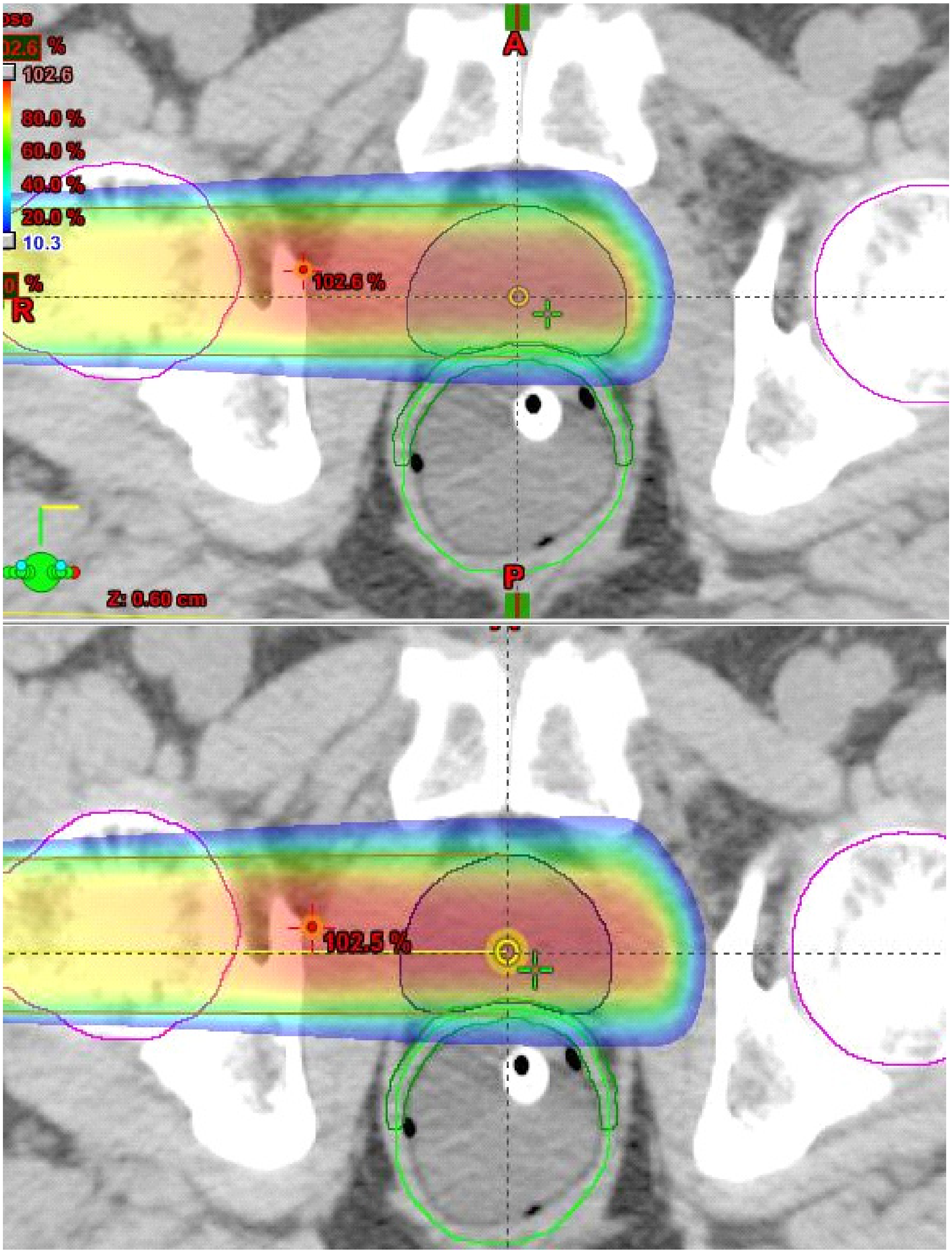

Figure 9: Distal margin applied to a lateral proton beam

The previous sections discussed the advantages of proton treatment and the challenges unique to the modality, i.e. range uncertainty. Unfortunately, the primary tool of protons to maximally spare adjacent critical structures, the abrupt distal fall-off, cannot be easily utilized in most clinical conditions, such as in the sparing of the rectum in prostate cancer treatment. This is because the range uncertainties in proton therapy require large treatment margins and thus limit the normal tissue sparing capabilities for organs just adjacent to the target. The range uncertainties are caused by uncertainties in determining the relative stopping power ratios for living tissues from CT Hounsfield units or the daily organ variations. The variation of physical depth from variation of the pelvic anatomy is demonstrated in Figure 10.Figure 10 illustrates interfractional prostate motion caused by bladder filling in a patient with endorectal balloon immobilization. Even with the balloon the distance from the anterior rectal wall to the skin surface at the mid-sagittal slice has increased by more than 1 cm. The prostate has shifted more than 5 millimeters posteriorely.

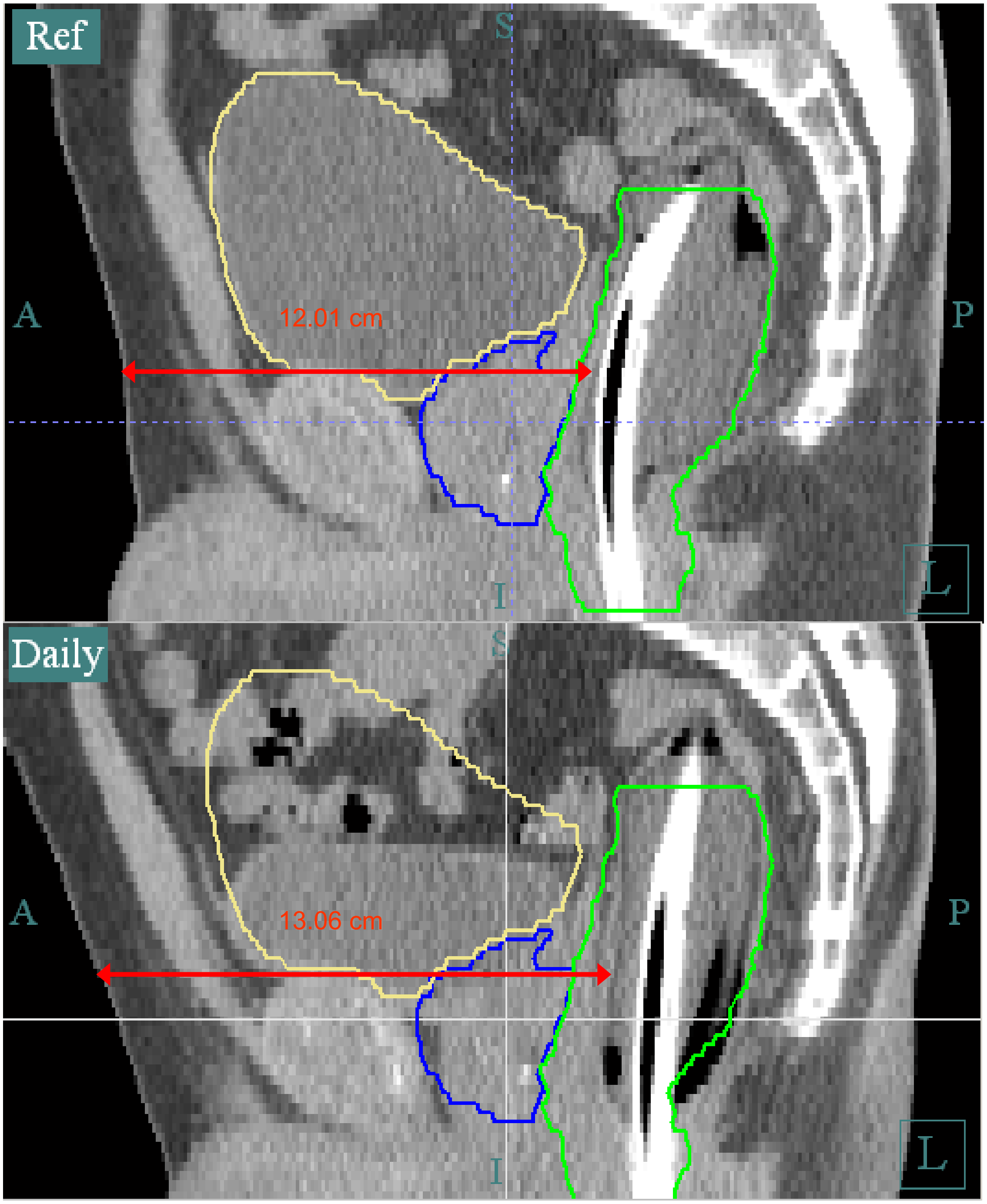

Figure 10: Anatomic variation in the depth to the anterior rectal wall

If the proton beam is directly pointing towards the rectum from the anterior direction, the range uncertainty of the Bragg peak can either over-irradiate the rectum or miss the posterior portion of the prostate target (adequate dosing of the peripheral zone is important in prostate treatment). Therefore, all current proton treatment techniques for prostate cancer use a lateral beam arrangement method,(13, 72, 73) which do not fully take the advantage of the sharp fall-off of proton beams. Proton therapy for prostate cancer using an anterior field is achievable only if one can accurately control the location of the sharp distal fall-off, as illustrated in Figure 11. The proposed anterior proton beam treatment would utilize the sharp distal fall-off of the proton beam to maximize sparing of the rectum during radiotherapy.

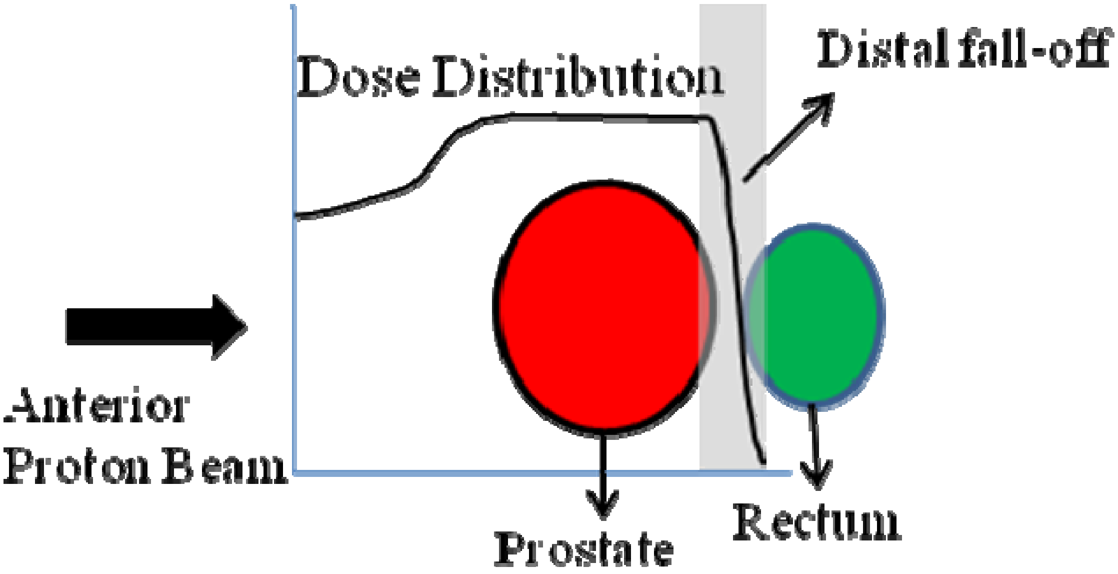

Figure 11: Prostate treatment using an anterior proton field

1.2.4 Summary: The development of modern proton therapy for prostate cancer

Protons deliver sub-maximal dose proximal to the target, maximal dose at treatment depth, and nearly no dose distal to the target. Therefore, protons have a theoretical advantage over treatment with photons. Conformal proton treatment is achieved with the use of dual scattering foils to generate a flat fluence profile, range modulator wheel to treat to a volume, and range compensator to conform a beam to the distal edge of the target organs. The proton's range is extremely sensitive to the stopping power of tissues in the path of the beam. The first source of range uncertainty is variation of heterogeneous material such as bone and air in the direction perpendicular to the beam path. Therefore the range compensator designed so that distal coverage of the target organs is maintained when tissue heterogeneities vary. However, rotations of highly dense objects, such as the femurs in the treatment of bilateral prostate treatment, may increase the radiological pathlength beyond those observed at reference CT and generate mis-coverage in the target organs. The second source of uncertainty is determination of proton stopping power from CT Hounsfield units. A generous distal margin is applied to the target organs to ensure coverage. The distal margin in conjunction with anatomic variation in the path of the beam prohibits clinicians from aiming proton beams directly at critical organs. In the case of the prostate, an anterior proton beam could treat the target while using its abrupt distal fall-off to maximally spare the rectum. However, without accurate control of the proton's range, treatment with the anterior beam either risks loss of treatment in the distal prostate or over exposure of the rectum.

Chapter 2: Hypothesis and Specific Aims

This chapter will begin with the purpose of the dissertation, state our hypothesis, state our specific aims to test our hypothesis, and conclude with the anticipated impact of the dissertation.

2.1 Purpose

The long-term objective of research in radiation oncology is the improvement of patient treatment, both in terms of biological outcome and quality of life. The proposed project has the potential to achieve both, for prostate cancer patients. The objective of this research is to reduce rectal dose delivered to patients receiving proton radiotherapy of the prostate, while providing dose enhancement to the prostate target. To achieve this goal, we will develop a novel system to reduce proton range uncertainty and enable the treatment of prostate cancer with an anterior proton beam arrangement. The proposed system uses a liquid scintillation filled rectal balloon to detect the distal edge of an anterior proton beam *in vivo*. The liquid-filled rectal balloon has a dual function. The first function is to act as an internal immobilization device for the rectum and the prostate. Liquid-filled rectal balloon will proactively stabilize both the rectum and the prostate. In addition, measurement of real-time scintillation light produced by the radiation interacting with the scintillation fluid reaching the rectum, will allow for continuous adjustment of the proton beam's fall-off position with a computerized range shifter. A schematic of the system design is shown in Figure 12. Real-time range detection and adaptively adjusting the proton penetration depth from the anterior beam allows for a minimal distal margin, resulting in superior rectal sparing over conventional bilateral proton treatment or IMRT.

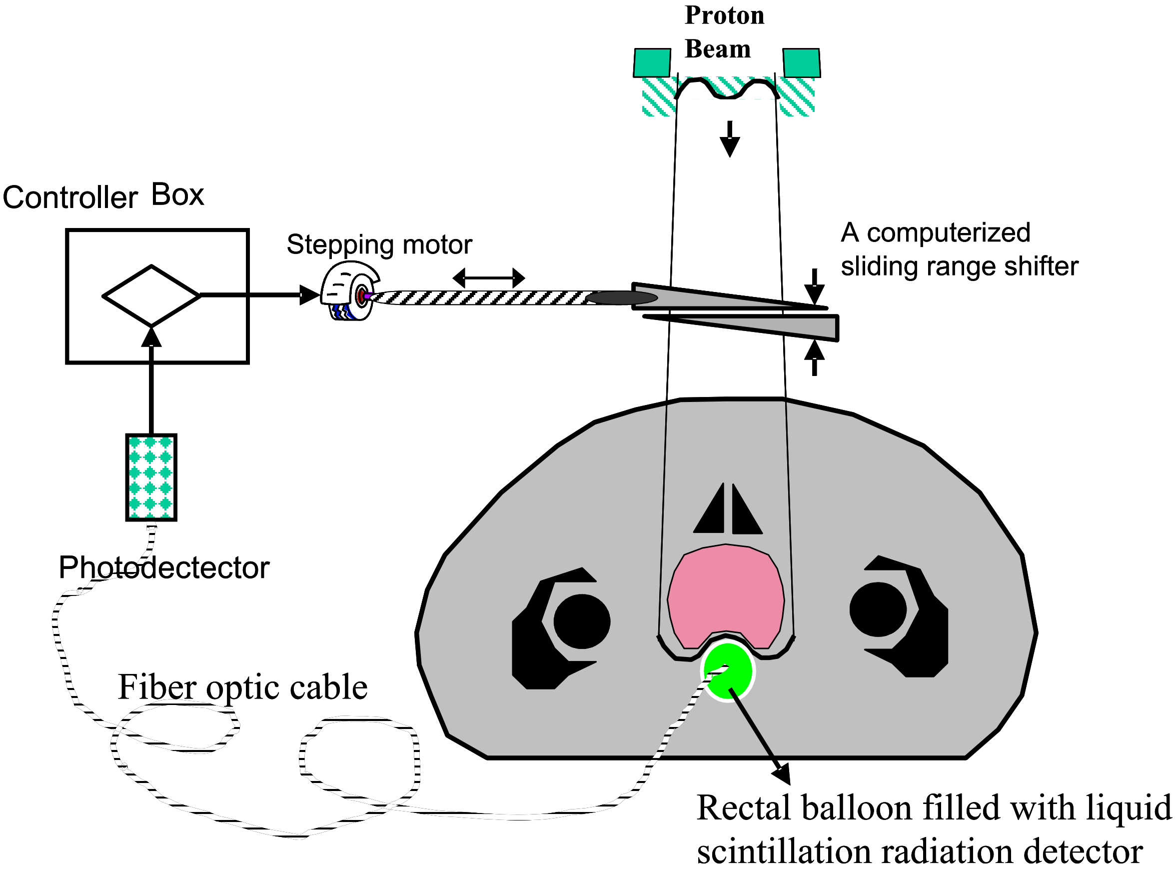

Figure 12: The *in vivo* proton beam positioning system

2.2 Hypothesis

The use of in vivo proton beam detection within a rectal balloon and dynamic range modulation of an anterior proton beam will enable the use of a reduced distal margin, reducing the mean rectal dose by 20% over conventional bilateral proton treatment and IMRT.

2.3 Specific Aims

1. Develop an *in vivo* proton beam detection device located within a rectal balloon.

*Working hypothesis: A*n *in vivo* proton beam detection device located within a rectal balloon can detect the distal fall-off of a proton beam within 2 mm (95% confidence interval).

2. Develop a computerized external proton beam range shifter to modulate proton beam energy/range.

*Working hypothesis: A*n external proton beam range shifter can modulate proton beam energy/range and localize the distal fall-off of a single anterior proton beam to the anterior rectal wall within 2 mm (95% confidence interval).

3. Determine dosimetric benefit of utilizing the *in vivo* proton beam detection device and external proton beam range shifter,

Working hypothesis: Using the measured precision of the *in vivo* proton beam detection device and external proton beam range shifter, the reduced margin planning treatment strategies reduce mean rectal dose by 20% over conventional bilateral proton and IMRT photon therapies.

2.4 Impact

The proposed *in vivo* patient positioning system will have an immediate impact on the treatment quality of current and future prostate cancer patients. The ability to spare extra volume of rectum during radiation treatment will substantially improve the patients' quality of life by reducing the incidence of radiation induced rectal toxicity and potentially secondary malignancies. The advantages of rectal sparing on patient rectal toxicity and quality of life were demonstrated with widespread adoption of IMRT over 3D-conformal photon therapy (26, 27, 74). Several studies have quantified the relation dose-volume in the rectum with probability of rectal toxicity and suggest that rectal toxicity is directly tied to volume of the rectum receiving near prescription doses (53, 75-78)). Conventional bilateral proton treatment provides little improvement over IMRT, with the exception in the low dose region. Our proposed anterior beam treatment substantially improves rectal sparing over both modalities. This treatment strategy takes advantage of the abrupt distal fall-off a proton beam. By detecting the distal falloff of a proton beam *in vivo*, we eliminate the need for the large distal margin and allow treatment with a highly conformal anterior proton beam. The system may also benefit future spot scanning and intensity-modulated proton therapy techniques, which provide further dose conformality to reduce normal tissue toxicity.

Chapter 3: Detection of an anterior proton beam for range determination

3.1 Introduction

Specific Aim 1: Develop an *in vivo* proton beam detection device located within a rectal balloon.

*Working hypothesis: A*n *in vivo* proton beam detection device located within a rectal balloon can detect the distal fall-off of a proton beam within 2 mm (95% confidence interval).

The first part of our detection system includes the endorectal balloon, scintillating solution, and photon detection system. With this system, if the anterior proton beam over-shoots through the prostate, a portion of the proton energy will be absorbed by the liquid scintillator, which tightly wraps around the anterior rectal wall and produces light emission within the scintillation liquid. The light produced can be captured and transmitted to the photo detector using a fiber optic light guide. The emitted light will be transmitted to a photodetector, at which the light signal will be converted into electric signal. If the proton beam range is too short, the proton beam will not penetrate the rectal balloon, therefore, there will be no signal detected by the system.

This chapter will begin with a description of scinitillation liquids emphasizing the scintillating fluid that was selected for this work, light capture with our chosen fiber, and photodection with our photodiode module. Then methods to verify dose rate and spatial invariace with photons, the relation of anterior beam SOBP depth and photocurrent collected, and estimation of our technique to register the prostate-rectal inferface using patient CT data, will be described. The results of these experiments will then be presented, followed by a discussion of study limitations, scintillation dosimetry, alternate range verification techiques, and scintillation quenching. We will conclude this chapter by evaluating our working hypothesis for specific aim 1.

3.2 Materials and methods

3.2.1 Light emission with scintillation

Scintillators are materials that exhibit luminescence when exposed to ionizing radiation (79). The ideal scintillator should convert energy to light linearly and with high efficiency, should be transparent to its emission spectra, emit scintillation photons promptly, and have a refractive index close to glass for good optical coupling with a light guide or photocathode window (80). There are three types of luminescence: prompt fluorescence, phosphorescence, and delayed fluorescence. Of the three types, prompt fluorescence has the shortest decay time of 10^{-9} to 10^{-7} seconds. The latter two types exhibit longer decay times of 10^{-3} to 10^{2} seconds. In the case of pulse mode photodetection, prompt fluorescence is the decay mode of use and delayed fluorescence and phosphorescence are considered extraneous noise. In the case of current mode photodetection, long decay luminescence is proportional to incident ionizing radiation and therefore a useful fraction of the signal, however background noise must be removed between each measurement to remove residual luminescence or wait a sufficiently long time to ensure the majority of trapped excitons decay(80).

While there are several forms of scintillators including inorganic crystals, plastic-based organic scintillators, and other potential detectors such as metal oxide semiconductor field effect transistors (MOSFET's) and thermoluminescent dosimeters (TLD's), liquid scintillator was selected for several reasons. The detector needed to be inserted either inside or on the rectal balloon, which prohibited the use of large solid detectors. The detector had to conform to the shape of the rectal balloon and the interface of the prostate and rectum. The detector had to be sensitive in the SOBP region of the proton beam in real time as the patient is treated. The real-time measurement requirement eliminated the use of TLD or film since these have to be removed to process the dose measurement (81). The use of scintillating fibers (82-85) or MOSFET's (86-88) for range determination was possible, however, these measured ionizing radiation over a small volume and are therefore only sensitive in the fall-off region of the proton beam. All treatments required a treatment margin, so these detectors would only be useful for initial daily set-up. The last reason to use liquid scintillation over other detectors was its relative insensitivity to radiation damage. The detector remained in the beam for the entire treatment and was resistant to exposures as high as 10^5 Gy (80). This radiation resistance enabled the re-use of the liquid resulting in substantially lower cost if the technique was used for daily fractionated radiation treatments.

For these reasons, liquid scintillator was selected as our radiation detector for range determination during treatment. The fluorescence process of the organic scintillators occurred in conjugated, aromatic molecules with rich π-electron structures. Fluorescence occurred when valence electrons are excited by ionizing radiation into their singlet energy states (Figure 13). These molecules then lost energy in the form of vibration and internal conversion before decaying back to ground from the S1 state with the emission of a scintillation photon within nanoseconds. Some excited valence electrons transitioned to triplet states through inter-system crossing and decayed to ground state by phosphorescence in milliseconds and at a longer wavelength. From the T1 state, some electrons were re-excited to the S1 state and decay by delayed fluorescence. Because all excited electrons decayed to S1 or T1 before luminescing, the overlap of absorption and emission spectra in scintillators was minimal resulting in very little self-absorption (80).

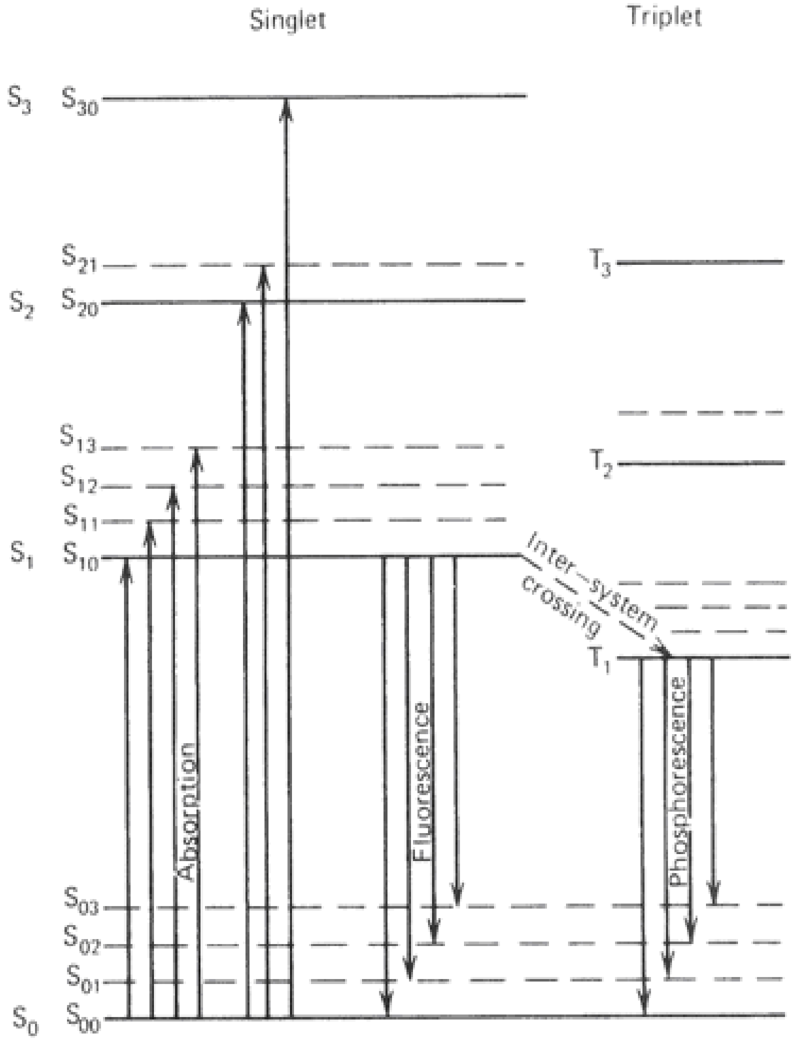

Figure 13: Diagram of the scintillation process (79)

The BC-531 liquid scintillation solution was selected (Saint Gobain Crystals, Newbury, OH) for this experiment. The primary reason for the choice was the solvent that is used in this solution, linear alkyl benzene. Most organic solvents used in commercially available scintillating solutions were highly toxic and carcinogenic such as benzene, toluene, xylene, cumene, and pseudocumene. Linear alkyl benzene was a bound form of benzene that was considerably less toxic that other solvents. It was also safe to use with most solid commercial plastics. Its National Fire Protection Agency (NFPA) health hazard classification was level 1 and its Hazardous Materials Identification System (HMIS) health hazard classification was level 1. These classifications indicated a slight risk for temporary injury from exposure. It was not listed as an acute or chronic health hazard by state and federal regulation. Exposure may cause slight irritation of the eyes, skin, or lungs. Ingestion may cause diarrhea, nausea, or gastrointestinal upset. Considering the stated toxicity of the solution, our physicians were comfortable using this technique with appropriate prophylactic measures such as use of a secondary condom around the balloon and the use of gloves when handling the solution.

Although safety and reactivity with plastics were the primary factors for determining the proper solution for our project, the other properties of the BC-531 solution also matched the stated aims of our project. The scintillator output efficiency was 59% of anthracene, which is comparable to other commercially available solutions from Saint Gobain Crystals. Its emission spectrum was peaked in the visible blue region (Figure 14). The refractive index of the solution was 1.47 which is very close to the refractive index of glass (1.5). Matching these indexes was important for proper optical coupling between the scintillator, light guide, and photodetector. The solution's electron density is 2.93 X 10^{23}, per cubic centimeter which was slightly lower but comparable to that of water. This was ideal because the proton dose and range may be simulated with a water-filled balloon, and a large difference in electron density could have modified the proton's dose and range in the balloon from the predicted values at treatment simulation.

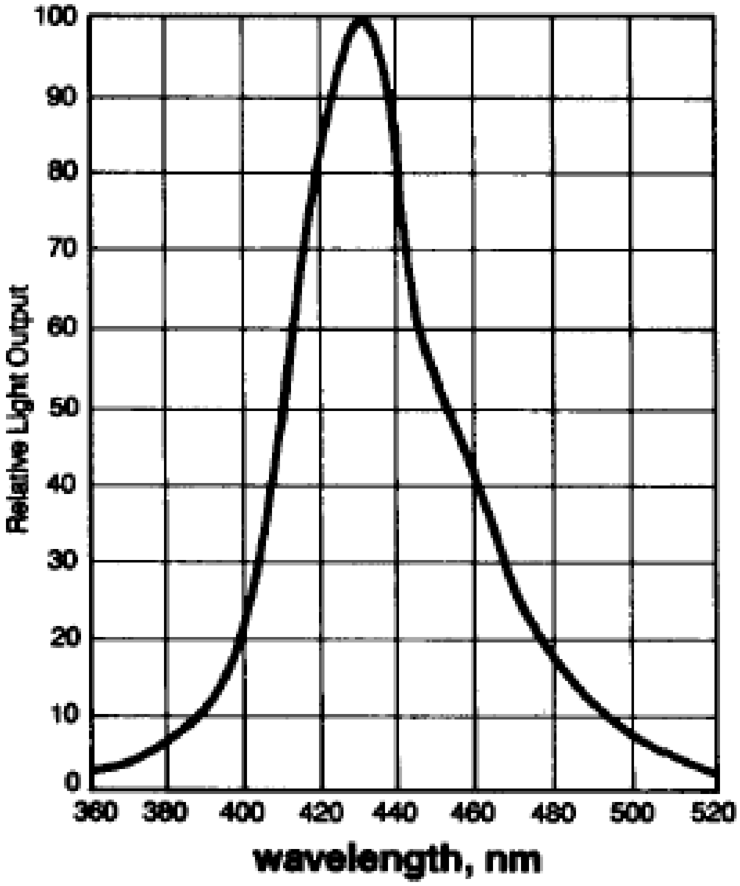

Figure 14: Emission spectra of liquid scintillating solution BC-531.

3.2.2 Light capture with fiber optics

In order to convert collected light into an electronic signal, it was first captured. To achieve light capture in our detector, a single fiber optic cable was fit through a commercial balloon stem (Radiadyne®, Houston, TX). Water-filled rectal balloons were used in proton radiation therapy in our clinic as prostate immobilization devices. Initial studies of patients using water-filled balloons and receiving repeat CT imaging confirmed the reproducibility of the shape and volume of the balloon on subsequent treatment fractions as well as the durability of the device in routine daily use (89). 35 patients were analyzed with a total of 105 repeat CTs during treatment. The planning CT was registered to each repeat CT using an in-house developed 3D image registration method. The one standard deviations (1SD) and (mean; range) are 1.1 mm (1.1; -1.0 to 3.0 mm) in anterior-posterior (AP), 1.3 mm (-0.8; -3.4 to 2.0mm) in superior-inferior (SI), and 0.5mm (-0.1; -0.1 to 1.0mm) in right-left (RL) directions respectively. The balloon was expected to maintain its immobilization function when water was replaced by scintillation liquid.

Light was emitted isotropically when ionizing radiation excited electrons within the scintillating solution. The fiber was positioned such that it faced the anterior rectal balloon wall and the majority of the light emission. A small fraction of the emitted light was incident on the face of the fiber, and this fraction was approximately the surface area of the fiber divided by the surface area of a sphere, $4\pi r^2$, where r was the distance from the emitted light to the fiber face. A small portion of the incident light on the fiber face was reflected back into the solution. The fraction of light polarized perpendicular to the plane of incidence, R_s, and inside the plane of incidence, R_p, were calculated with Snell's Law (Equation 1) and Fresnel's equations (Equation 2) as a function of the solution refractive index (n_1), fiber core refractive index (n_2), angle of incidence (θ_i), and angle of transmittance (θ_t) (90).

$$\frac{\sin\theta_1}{\sin\theta_2} = \frac{v_1}{v_2} = \frac{n_2}{n_1}$$

Equation 1: Snell's law

$$R_S = \left[\frac{\sin(\theta_t - \theta_i)}{\sin(\theta_t + \theta_i)}\right]^2 = \left[\frac{n_1\cos\theta_i - n_2\cos\theta_t}{n_1\cos\theta_i + n_2\cos\theta_t}\right]^2$$

$$R_P = \left[\frac{\tan(\theta_t - \theta_i)}{\tan(\theta_t + \theta_i)}\right]^2 = \left[\frac{n_1\cos\theta_t - n_2\cos\theta_i}{n_1\cos\theta_t + n_2\cos\theta_i}\right]^2$$

Equation 2: Fresnel's equations

Once incident photons were transmitted and refracted, they encountered the normal surface of the cladding with an angle greater than the critical angle (Equation 3) for total internal reflection (Figure 15). This angle was set by the ratio of the indexes of the fiber core and cladding. Those photons incident to the cladding at acute angles were partially transmitted through the cladding and the reflection portion quickly fell to zero after several reflections. The net result of these two interfaces (solution/core and core/cladding) was that photons emitted within an acceptance cone were incident to the solution-core interface acutely for transmittance and the core-cladding interface obtusely for reflection to propagate the fiber length and reach the photodetector. The half-angle of this acceptance cone is illustrated in figure 3 and expressed in equation 4 (90).

$$\theta_{crit} = \sin^{-1}\left(\frac{n_2}{n_1}\right)$$

Equation 3: Critical angle for total internal reflectance

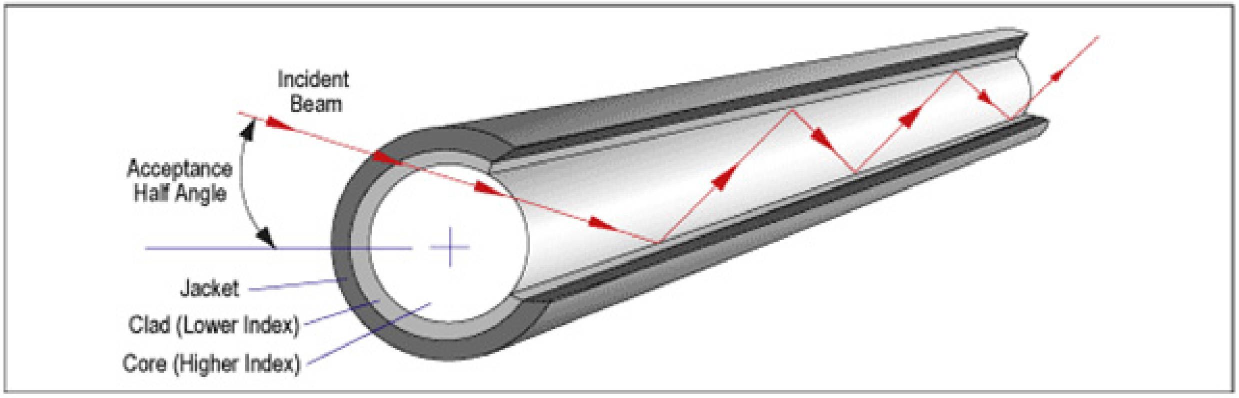

Figure 15: Internal reflection of a captured photon

(www.edmundoptics.com)

$$\sin\theta_{HA} = \frac{\sqrt{n_1^{\ 2} - n_2^{\ 2}}}{n_0}$$

Equation 4: Half-angle of acceptance in a fiber optic cable

Considering the previous conditions for light collection within our fiber, a step-indexed, multimode, optical grade fiber from Edmund Optics (Barrington, NJ) was selected. This fiber had a large difference in the refractive index of the core (1.492) and cladding (1.402) for a large acceptance cone (half-angle: 30.5^{o} in air). The calculated critical angle for internal reflection was 20^{o} and the corresponding half-angle of acceptance in the solution was 20.3^{o} for meridional rays, or rays that passed through the central axis of the fiber. The half-angle of the fiber was slightly larger than this value if skew rays, or rays that are internally reflected but do not cross the fiber axis, are considered. The reflection coefficients calculated with equation 2 are displayed in figure 16 as a function of angle of incidence. Since the refractive index of the solution and core were similar, this value was close to zero and nearly all incident acutely angled photons were accepted.

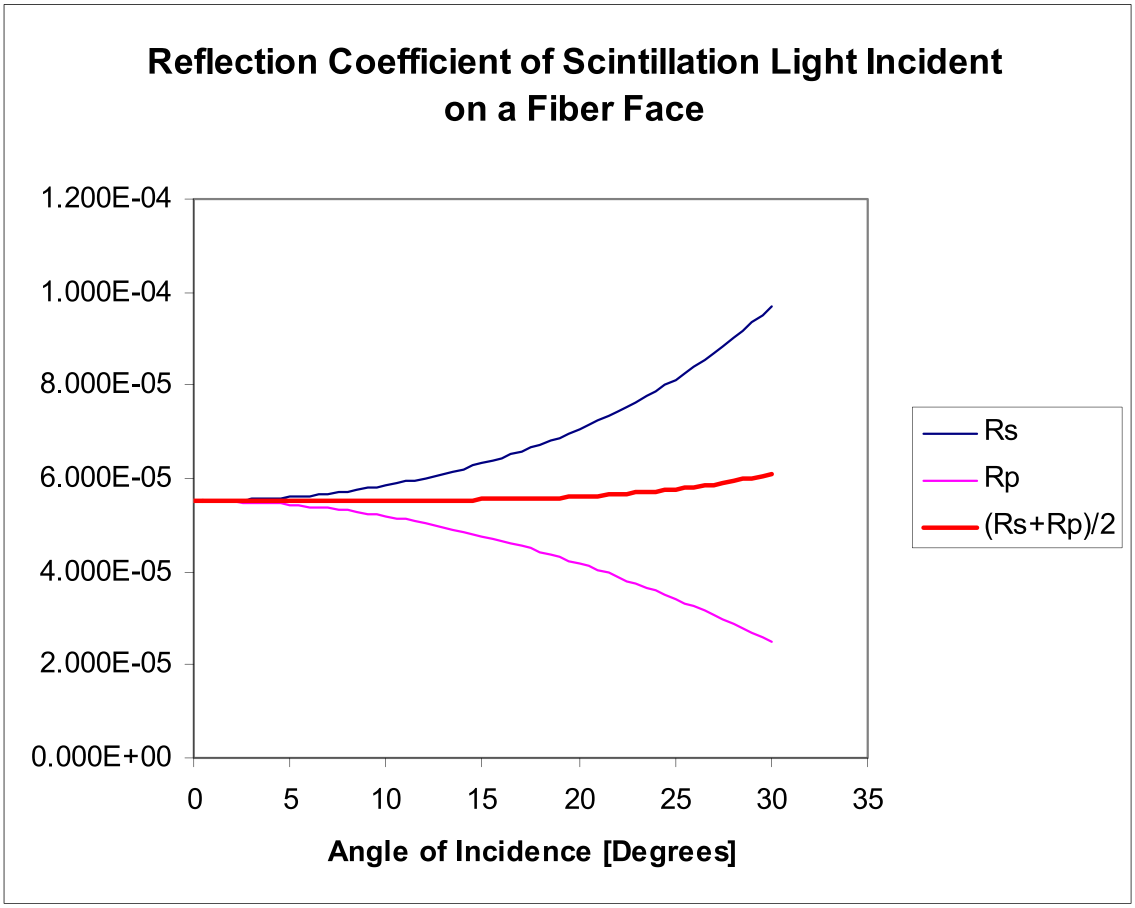

Figure 16: Reflection coefficients of photons emitted inside the solution incident on the fiber face

This particular fiber was the largest diameter fiber (2 mm) offered by this vendor with a protective plastic sheath. Although larger fibers could potentially increase the fraction of light captured, they required a larger bend radius to avoid damage (Figure 17). The minimum bending radius for these fibers was 25 times their outer diameter, slightly greater than 5 cm. For the fiber to face the anterior rectal wall, it must bend nearly 90 degrees in the distance from the balloon base to the middle of the stem. The use of the 2mm fiber was the limit that we can use for controlled *in vitro* purposes. For insertion into a patient, our detector would have to utilize a smaller fiber to ensure the fiber was not damaged during the insertion process. Bending the fiber did have some positive benefit. When the fiber was bent as shown in figure 17, the angle of incidence along the outer diameter was decreased, resulting in a rejection of modes with characteristic angles close to the critical angle of the fiber and a narrowing of the collection cone (90). Normally this would be detrimental to light collection and users of the detector would have to ensure that the fiber remains straight during use. Bending the fiber acutely, as in our detection volume, automatically rejected the highest order modes. This ensures that subsequent bends down the fiber did not affect the light output and that our light collection was consistent. Even though fiber bending decreased total light collection, it ultimately increased the robustness of our detector.

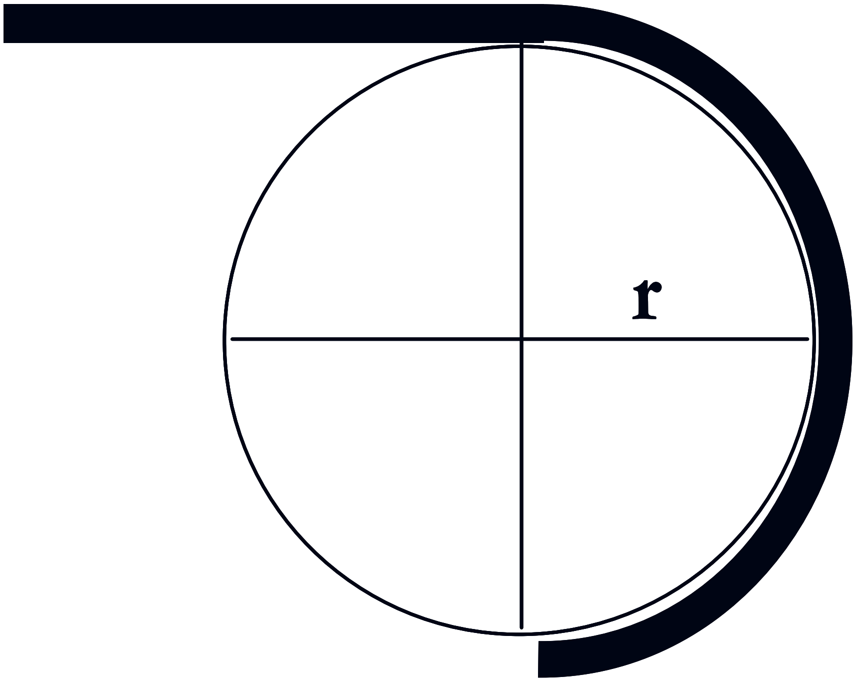

Figure 17: Bend radius of a fiber optic cable

Since the dose deposition of a flat anterior proton beam inside our solution and the corresponding light output was known along with the light collection of a fiber facing the anterior balloon surface, we could mathematically express the light collection within our fiber (Equation 5).

$$Light(d) = \mu_{sc\,\mathrm{in}} \int_0^k \varepsilon_{Sc\,\mathrm{in}}\, Dose(d,x) * \frac{\pi * r_{fiber}{}^2}{4\pi (k-x)^2 C_{(k-x)^2 \to r^2}} * (\, k-x)\tan\, \theta_{HA})\, ^2 dx$$

Equation 5: Expression for two-dimensional light collection

The total light emitted by our solution was proportional to the energy deposited [Joules] and scintillation efficiency [~ constant 3-5 %](79). Thus, light emitted was the product of dose in units of the scintillation efficiency [~ 3-5 %], Grey [Joules/kg], the density of the solution [kg/cc], and volume [cc]. Not all emitted light was collected. Only the light within the collection cone was accepted into the fiber. The volume of the cone subtended by the beam was the product of the distance of the fiber to the beam, k – x, and the tangent of the fiber's half-angle of acceptance squared, multiplied the thickness of the cone, dx (Figure 18). The portion of light incident on the fiber face from an isotropically emitting source was inversely proportional to the distance to the fiber face, ~ (k-x), squared. A term was included in the denominator to scale (k-x) to the average radial distance on the cone at the point, (k-x). This value was approximately 1.08. Therefore, light collected was independent of the distance from the fiber face to the anterior surface of the detector, k. The remaining terms were product of constants, dose (x), and dx. Thus for a large flat one-dimensional beam, light collected in our fiber was proportional to the integrated depth dose within the detector. For a uniformly distributed dose, such as the proton SOBP, light collected was linear with depth of the beam within the detector.

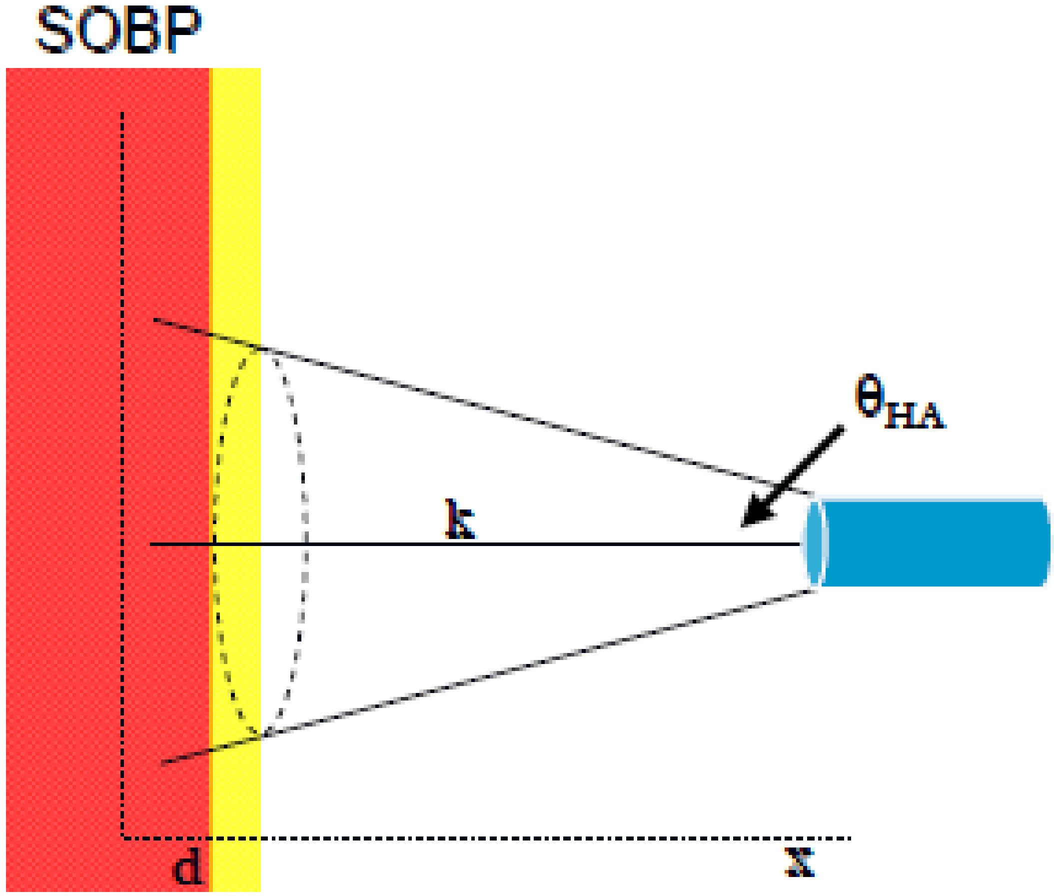

Figure 18 Expression for light collection of a fiber facing the anterior detector surface

3.2.3 Light conversion to current with photodetection

Though, there were several options to choose from, to detect scintillation light, a photodiode was selected for several reasons. Photodiodes were cheaper than alternatives such as photomultiplier tubes (PMT) or charge-couple device (CCD) cameras. They were also insensitive to magnetic fields. This was extremely important if the detector was inside the treatment room during measurement. They typically had a greater fractional yield of photoelectrons per incident photon, or quantum efficiency, than PMT's. They were mechanically rugged and required only battery power for operation (80). These features were very important if the device was used daily during a patient's fractionated treatment. PMT's required a stable high voltage source because the detector's gain was highly dependent upon the applied voltage to the dynode structures during electron multiplication (Hamamatsu PMT handbook). The supporting electronics for PMT operation were bulky and non-ideal for clinical use. CCD cameras required external cooling to achieve a sufficient signal-to-noise ratio for precise scintillation detection. The cooling process can take more than 30 minutes, which may be impractical for repeated use.

Photodiodes ideally generated current proportional to the light incident on their photocathode. As scintillation light reached the photocathode of the photodiode, valence electrons originating from the doped impurities in the crystal lattice were excited from the valance band into the conduction band (80). The energy difference between these bands was called the band gap energy and was 1-2 eV for silicon photodiodes. The typical energy of an incident scintillation photon was typically 3-4 eV, sufficient to generate electron-hole pairs in the cathode. The bias voltage then forced current across the depletion region to the diode's anode. This current could then be measured with a digital volt meter or oscilloscope across a load resistor or directly with a current measurement tool such as an electrometer.

We chose the DET36A biased detector (Thorlabs, Newton, New Jersey) for our measurements. This detector was a silicon PIN photodiode that had a 3.6 mm by 3.6 mm active area sensitive to photons from 350 to 1100 nm (Figure 19). The specified dark current was 0.35 nA with a 10V bias voltage. The internal electronics was enclosed in rugged aluminum housing and included a BNC output, a battery check switch, and a threaded optical coupler for adapting lenses, filters, or SMA/FC fiber adapters. The output of the detector was linear with incident light intensity up to 1 mA output. The lifetime of the included 12 V bias battery was stated 40 hours at 1 mA output current.

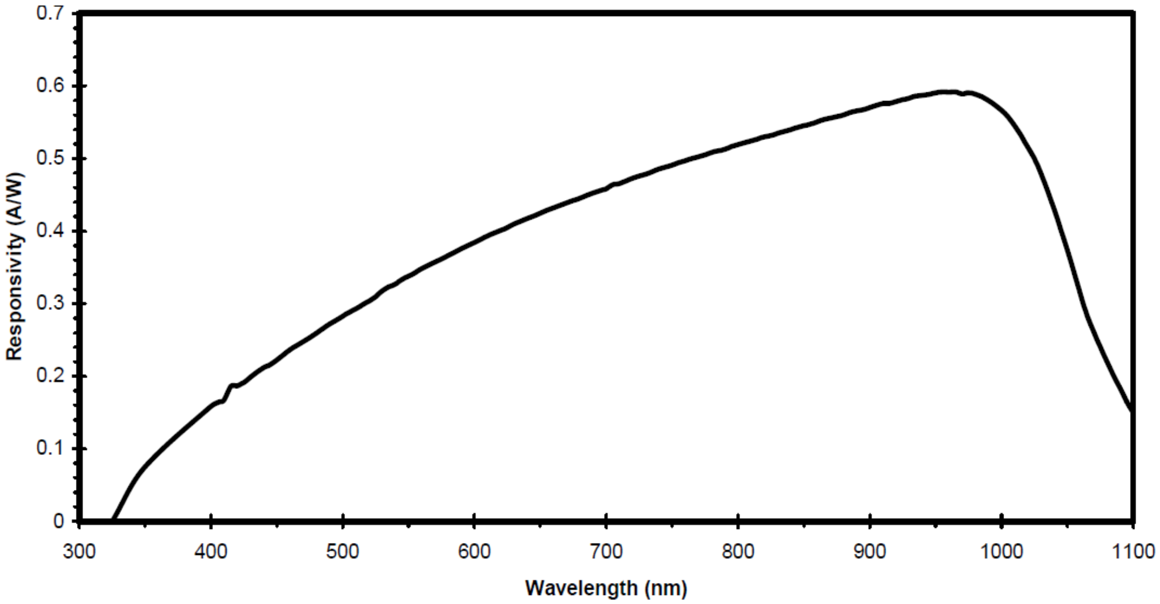

Figure 19: Spectral response of the DET36A module (www.thorlabs.com).

An SMA adapter was threaded into our detector. The SMA connector was then drilled to 2 mm in diameter to match the diameter of the selected optical fiber (Figure 20 top). The fiber was then glued into the connector and its face was polished incrementally with 800 to 2000 grade abrasive paper to provide quality optical coupling to the surface of the photodiode. After threading the fiber to the surface of the diode, black electric tape was applied over the connector and thread to maintain the coupling. An additional layer of aluminum foil and electric tape was applied to shield the residual light leakage.

The photocurrent generated by our detector was measured with a Keithley 602 electrometer (Keithley Instruments, Inc, Cleveland, Ohio). To connect the detector to the electrometer, a male/male BNC adapter and female BNC to a 2 lug triaxial male adapter was used to mate the female BNC output of the detector to the female triaxial input of the electrometer (Figure 20 middle). The electrometer was set to current mode in nanoamperes (10^{-9} A) for all measurements.

To generate a digital signal for data analysis, the analog output on the rear side of the electrometer was connected to an analog-to-digital converter (ADC). The analog output of the electrometer provided voltage representing the selected scale of the front of the instrument, The DATAQ DI-158 programmable ADC was selected for USB interface with our computer. This four-channel ADC had 12-bit resolution over +/- 64 Volts, an internal gain range from 2^0 to 2^9, and a maximum sampling frequency of 14.4 kHz. Based on preliminary photon measurements with our detector system, photocurrent from 0 to nearly 1 nA was observed at maximum dose rate with an open field. Therefore the internal gain was set to 64 to best match the estimated current range and to optimize the 12-bit resolution (+/- 2048 steps) of the ADC for approximately 0.488 picoampere measurement precision.

Figure 20: Photodiode module (top), electrometer (middle), and analog-to-digital converter (bottom) for converting emitted light into a digital signal

Operation of some of the programmable features on the ADC required the use of Dataq's WinDAQ software (DATAQ Instruments, Inc., Akron, OH). Use of the free version of the software throttled our sampling frequency to 240 Hz; however the software had an option to average the sampled data (at 14.4 kHz) to the 240 display frequency. This significantly reduced variation of the background noise, and increased the signal-to-noise ratio for the detector. The vendor software also provided recording features and data processing options. However, we interfaced both devices with LABVIEW (National Instruments, Austin, TX) for future integration of the detector with the dual wedge range shifter.

With the WinDAQ software operating in the background, the LABVIEW drivers provided by the vendor passed the scaled data to our LABVIEW virtual instrument (Figure 21). The LABVIEW virtual instrument had an on/off switch, channel selector, numerical data register and graphical data real-time display. The virtual instrument used the ActiveX controls of the driver to initialize the ADC, select the measurement channels, and obtain the scaled data from WINDAQ. The program used a timed loop and shift register to retrieve the data, display the data on the front panel, and generate an array with the measurements. The program then exported the array in a tab-delimited spreadsheet for subsequent analysis.

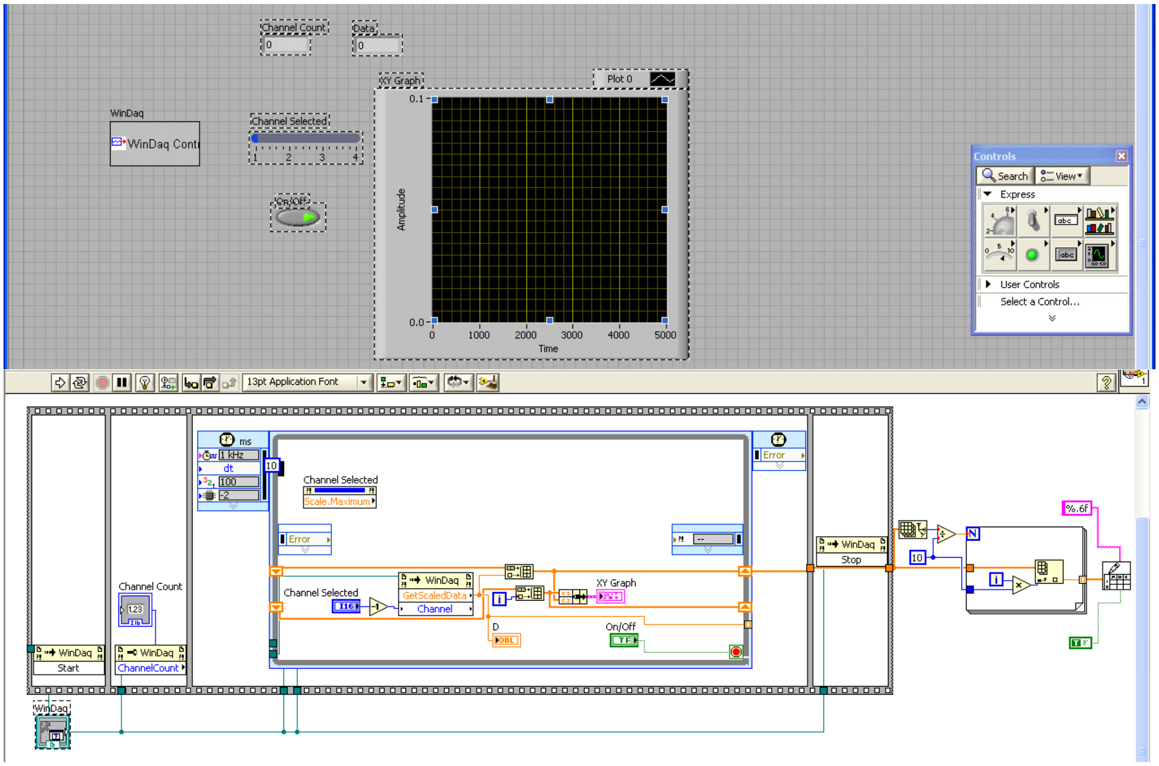

Figure 21: Labview virtual instrument for our detector.

3.2.4 Experiment methodolgy

Before beginning the experiments, 60 mL of liguid scintillation solution was inserted into commercially available endorectal balloons to test the compatibility of the balloon material with the chosen scintillation solution. The first balloon selected, a latex balloon from MEDRAD (MEDRAD, Inc., Pittsburgh, PA), was damaged after the solution was left several days in the balloon. When the balloon was removed from the experimental phantom, the stem ripped from the balloon at the base. The same test was then attempted with the Radiadyne (RadiaDyne, LLC, Houston TX) balloon made of a plastic material. After two weeks of holding the solution, the balloon maintained its shape and structural integrity.

The preliminary measurements were made in a light shielded IMRT film phantom (Figure 22). A 2 mm fiber was inserted into the vial straight down from the top of the volume, collecting light from most of the detector volume. External fiducials were used to mark align the center of the detector volume and the treatment isocenter for the first measurements. After the fiducials were affixed to the phantom and the vial was in its permanent position, the phantom was imaged with a CT scanner. Using the CT data, the dose delivered to the vial during the measurements was calculated and compared with the generated photocurrent.

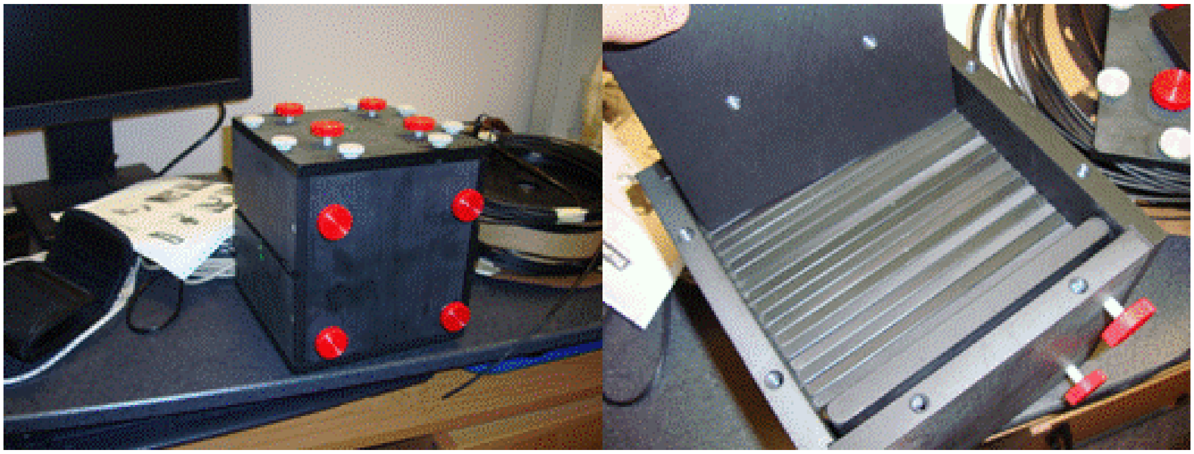

Figure 22: IMRT film phantom for preliminary measurements

For the first set of measurements, the 10 X 10 cm^2 open field generated photocurrent was measured with dose rates of 100, 200, 400, and 600 monitor units per minute for 50, 100, 200, and 300 monitor units respectively. The real-time current generated by these measurements was background subtracted and correlated with the dose rate delivered to the solution with the Pearson parametric correlation.

Once dose linearity was established, the next set of photon measurements investigated the sensitivity of light collection as a function of position within our detector. The MLC shaper software (Varian Medical, Palo Alto, CA) was used to vary the position of the beam in real time. This software conveniently modified the multi-leaf collimator control points within the Pinnacle treatment planning system (Royal Philips Electronics, Amsterdam, The Netherlands). Using the preliminary detector prototype and IMRT film phantom, we measured the photocurrent with a 3 mm wide MLC window that traveled at a constant rate across the field width from the anterior to posterior portions of the phantom (Figure 23). Figure 23, illustrated the 3mm sliding window segment delivered to the test phantom in the Pinnacle treatment planning system with isodose lines ranging from 60% (red) to 10% (white) of the max point dose within the phantom. The length as well as the width of the sliding window was varied to investigate these factor’s effects on the measured current. To investigate the relation of light collection as a function of distance from the fiber face, the collimator was rotated 90 degrees and a 4 cm by 3 mm sliding MLC window was delivered superiorly from the bottom of the vial (top of figure) past the face of the fiber. These measurements suggested that redesign of the detector with the fiber facing the anterior detector surface may result in superior performance.

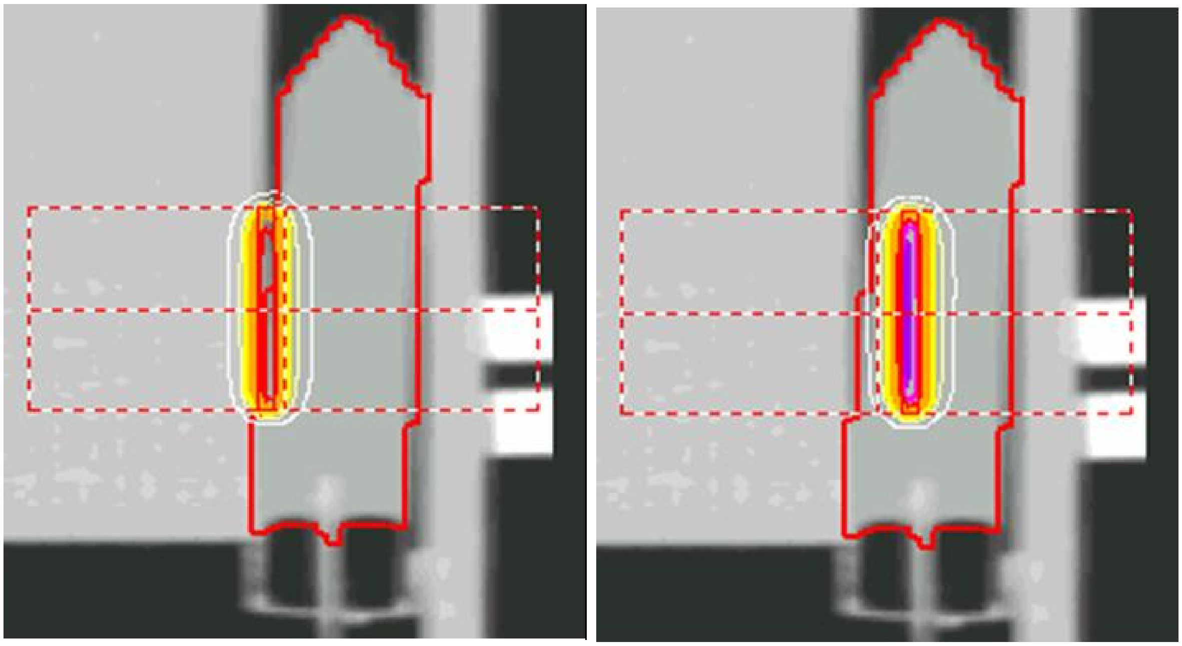

Figure 23: MLC sliding window in the test phantom

After the previous measurements, a second detector was fabricated with the fiber facing the anterior detector wall. The Radiadyne outer balloon was removed and a hole was drilled through the stem at 45 degrees. A light-tinted glass vial of comparable volume and length to the commercial balloon was used as a surrogate in all of the measurements. The plastic cap of this vial was drilled with holes to the exact dimensions of the balloon stem and fiber to ensure that the vial would remain liquid tight during our experiments. After threading the balloon stem and fiber through the plastic cap, the fiber was inserted into the 45 degree hole drilled into the stem of the balloon and fixed into position with Krazy glue. The holes at the base of the vial cap were also coated with Krazy glue to close the residual gap between the fiber, stem, and cap. The vial was then filled with 60 mL of liquid scintillator. The vial remained closed for the duration of all experiments. The position of the stem and fiber within the balloon was subsequently verified by CT (Figure 25).

A custom-made deformable phantom simulating a male pelvis, was used to measure radiation doses in the (simulated) prostate target and anterior rectal wall. The phantom, as shown in Figure 24, was made of tissue substitute materials by blending epoxy resins, urethanes, water based polymers and other proprietary materials (CIRS, Inc., Norfolk, VA). The phantom had an opening for inserting the rectal balloon and scintillation detectors designed in this study. When the balloon was inflated, the rectum displaced the prostate target anteriorely, which simulated the conditions of rectal filling in a patient treatment. The deformable phantom was used to simulate a patient treatment and test our scintillation detectors system before applying this technique to real patients.

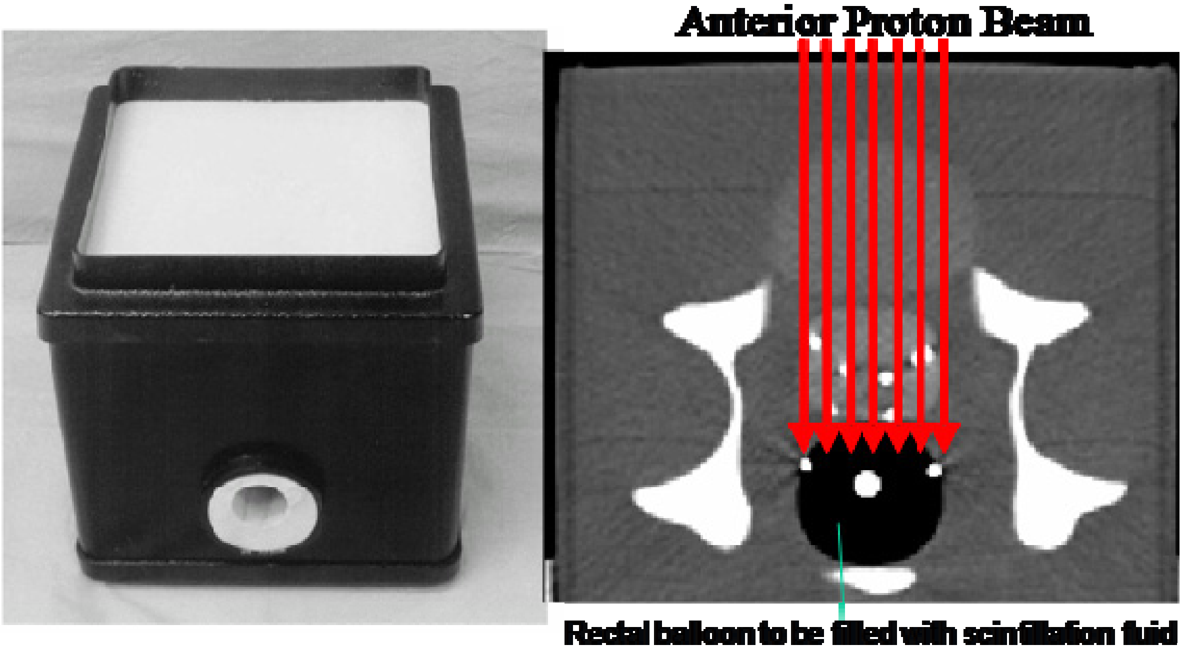

Figure 24: A custom-built deformable pelvic phantom

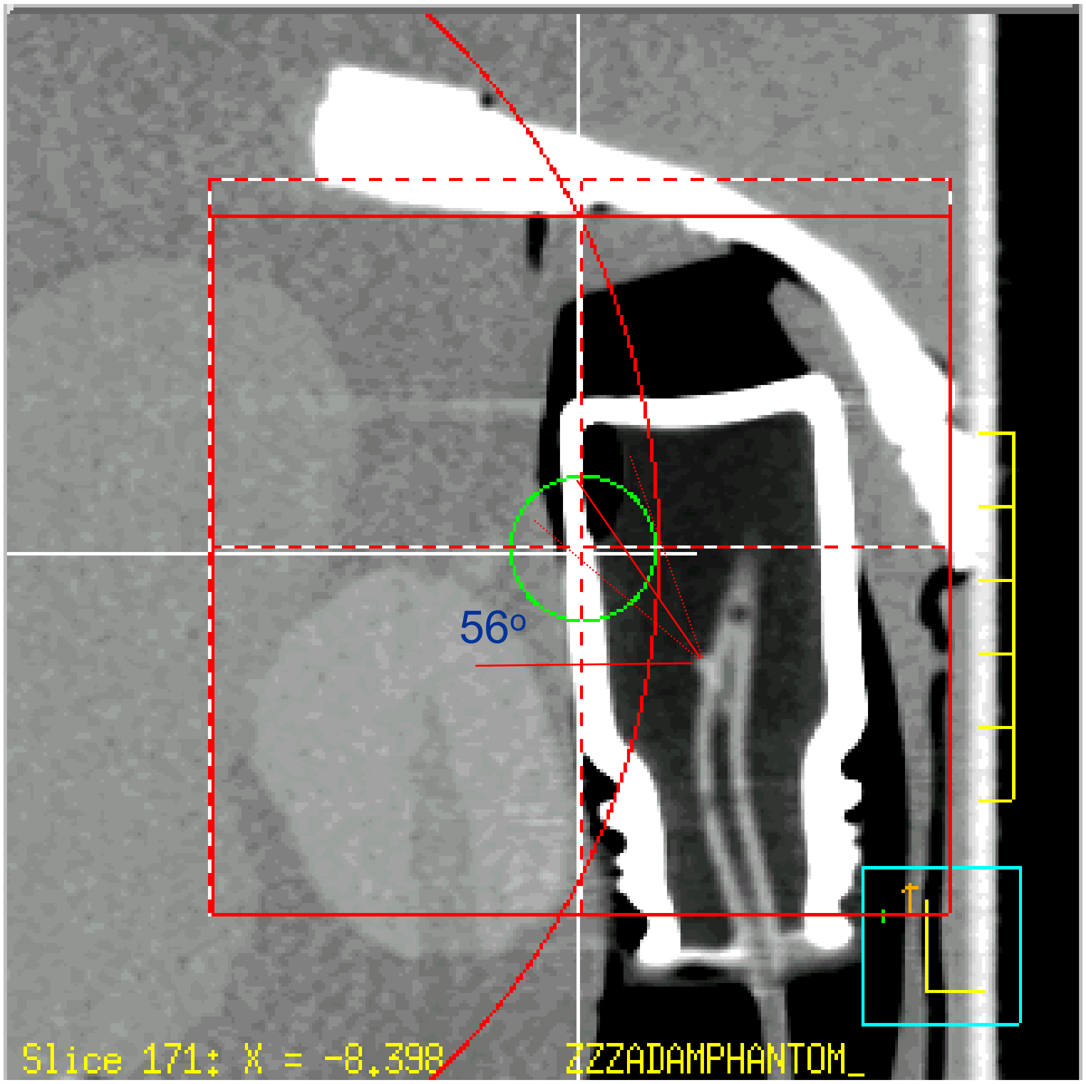

Figure 25: Light vial with machined stem and fiber inserted into our anthropomorphic phantom

After construction of the light detection portion of the beam positioning device, the precision of the detector was measured. To measure the precision, a measurement was performed with a single proton beam incident upon a water phantom that holds the scintillation detector (Figure 26). The phantom was irradiated at the University of Texas M D Anderson Proton Therapy Center in Houston, TX on the G1 rotatable beam gantry. The beam delivered 200 MU to a depth of 17.7 cm with a 10 cm square field size and 10 cm SOBP at approximately 270 cm SAD in physics mode. Physical depth to the anterior detector interface was 11.7 cm. A variable thickness of known attenuator (polystyrene slabs) was repeatedly moved into the distal fall-off of the beam in order to determine the detection threshold as a function of beam depth. The initial build-up thickness was 6 cm. The current was then measured with build-up of 5.5 cm to 6.5 cm in 1 mm increments. We then measured with build-up thickness of 5 cm, 4.5 cm, and 4 cm. Pulses were background subtracted and integrated over the 200 MU delivered to generate the photocurrent as a function of SOBP depth into the detector. Since the radiological depth to the detector surface was unknown, the known relation for light collection was exploited to determine the point where the SOBP reaches the detector. Since the relation is linear and builds in the fall-off region, a bilinear fit of the SOBP and fall-off portions of the relations was used to find the point where the relation diverges. The origin was then reset to this point.

The reproducibility of the light output as a function of beam position determined the uncertainty of the light collection device. Since treatment in physics mode resulted in uneven proton spills, each spill was normalized to the number of monitor units delivered. The standard deviation of these normalized pulses was then measured for each SOBP position and the coefficient of variation at each point was calculated. For illustration purposes the error bars on the SOBP depth versus photocurrent reflected the coefficient of variation of the proton spills for each point. Using these error bars and the measured gradient of the relation when the SOBP is inside the detector, the spatial resolution of our technique was determined assuming a single proton spill was used to determine depth.

Figure 26: Experimental apparatus for measuring the photocurrent as a function of SOBP depth

Although phantom measurements provided an estimation of the device's precision as a function of SOBP depth within the detector, it did not take into account the variation of dose and subsequent light emitted as the balloon and target organs deform in shape. For this experiment, the worst case scenario was assumed, that the scintillated light emitted and captured is proportional to the mean dose in the detector volume. Estimation of *in vivo* uncertainty of the light output of our scintillator is the worst case scenario because light collection was specific to the depth of the proton beam within the detector. The prototype was theoretically insensitive to some deformation as discussed in figure 18. .

Eight prostate cancer patients enrolled in an IRB-approved protocol contributed 8 reference and 19 total daily CT image sets for this study. Each CT data set was imported into the Pinnacle treatment planning software for dosimetric calculations. A single beam from the lateral direction was created for delivery of the sliding MLC window. To create the aperture for the window, a 2mm diameter circular ROI was created inside the anterior edge of the rectum on each axial slice. This ROI was then expanded anteriorely by 3 mm. The final ROI was generated by subtracting the anterior point ROI from the expanded, leaving a 3mm wide ROI tightly abutting the anterior rectal wall. The MLC segment was then created by blocking the beam to this ROI (Figure 27). To simulate the sliding of this segment in Pinnacle, 10 additional beams were generated from the original beam with an isocenter displaced anteriorly and posteriorly in 1mm increments from -5mm to 5 mm.

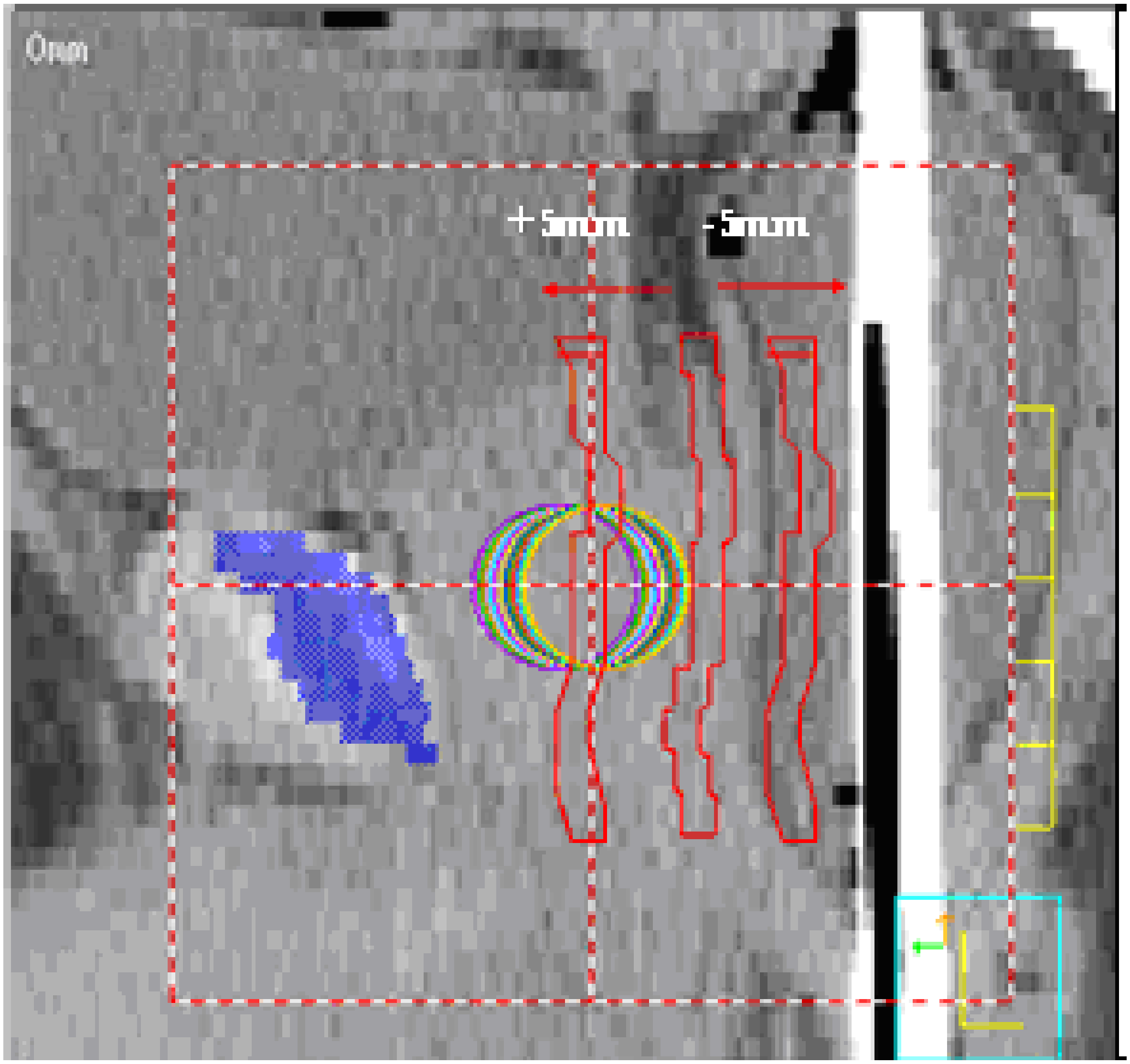

Figure 27: Beam-eye-view of the MLC sliding window segments

Each segment was set to deliver 500 MU in order to generate the required dose display precision in Pinnacle. The dose grid was set at 3 millimeter resolution. The mean rectal dose delivered to the entire rectum was then calculated in Pinnacle. The mean rectal dose of each segment was then plotted against the beam position to generate the reference dose-position relationship (Figure 28) on the patient's reference CT.

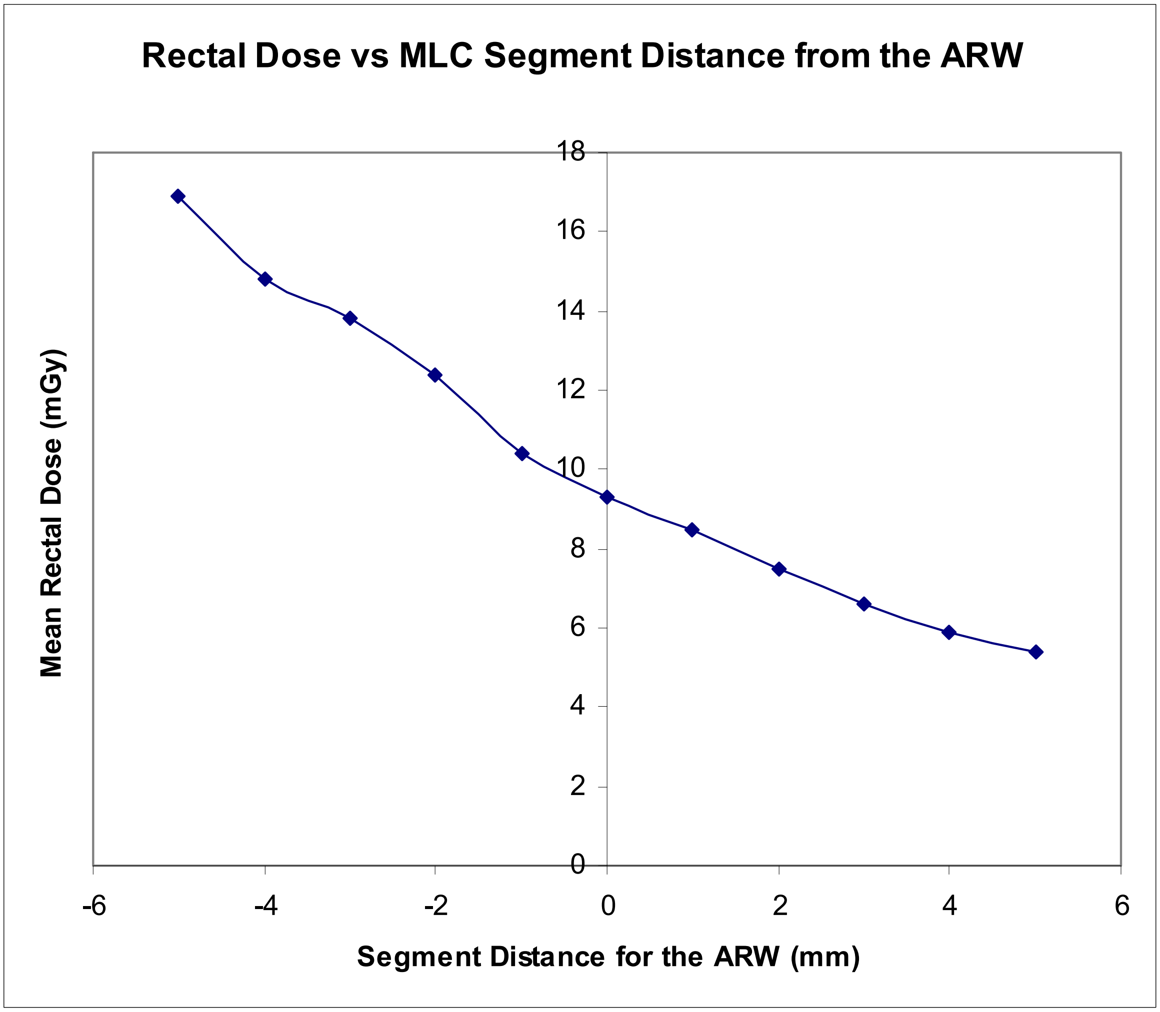

Figure 28: Mean rectal dose as a function of segment distance from the ARW

This relation was then compared to similar relations calculated on the patient's daily CT image sets for simulated device registration based on mean rectal dose and thus light emitted within the balloon. These daily graphs were then manual shifted to match the reference relationship and obtain the daily corrective shift to align the treatment at the anterior rectal wall (Figure 29). In the cases were the slopes were significantly different, the relations were matched at the origin on the reference CT when possible.

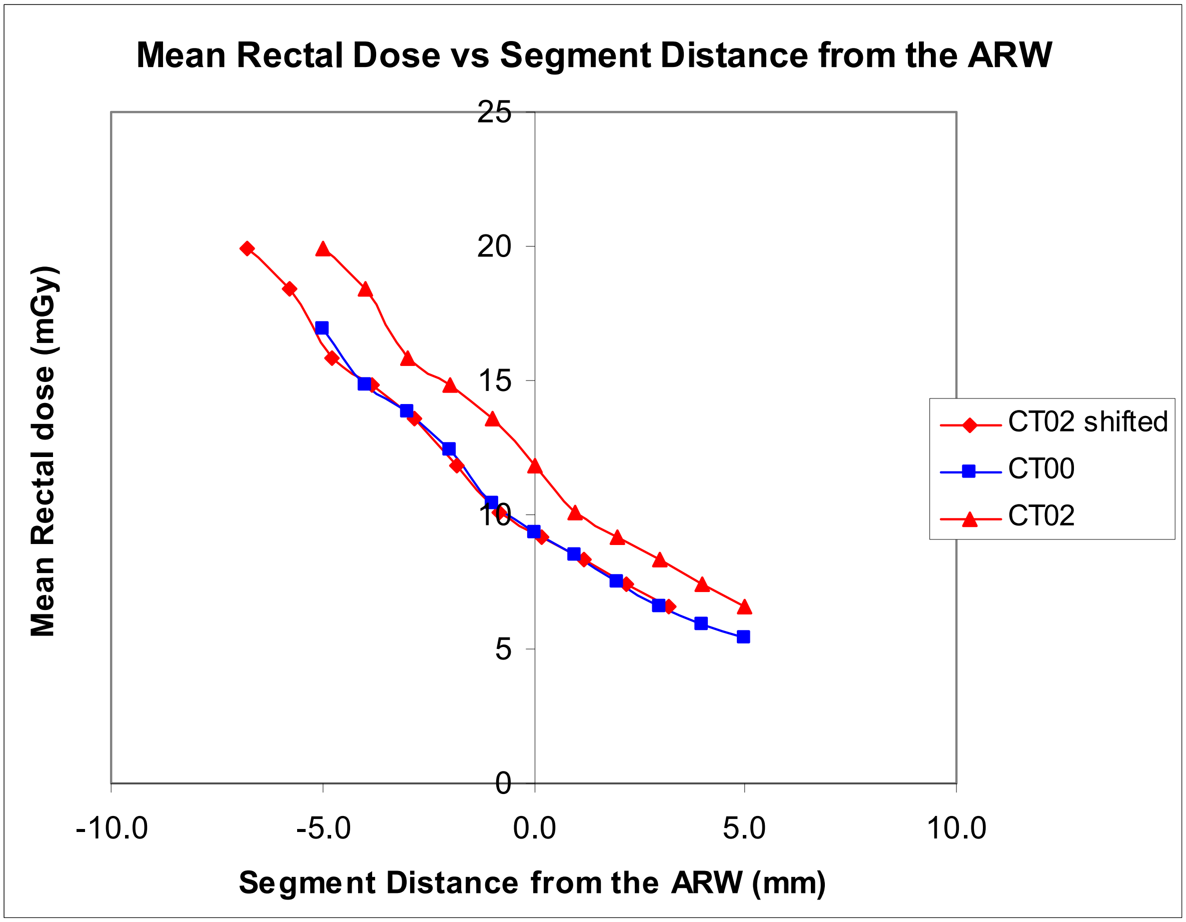

Figure 29: Manual registration of dose-position relation for alignment

The same CT image sets were then imported in our in-house CT registration software, Computer-aided Targeting (CAT) (59, 91). A one-dimensional alignment of the anterior rectal wall was manually determined to validate the dosimetry method, as shown in Figure 30. In cases where the rectal position rotated, alignment was attempted at the anterior rectal wall near the center slice of the prostate.

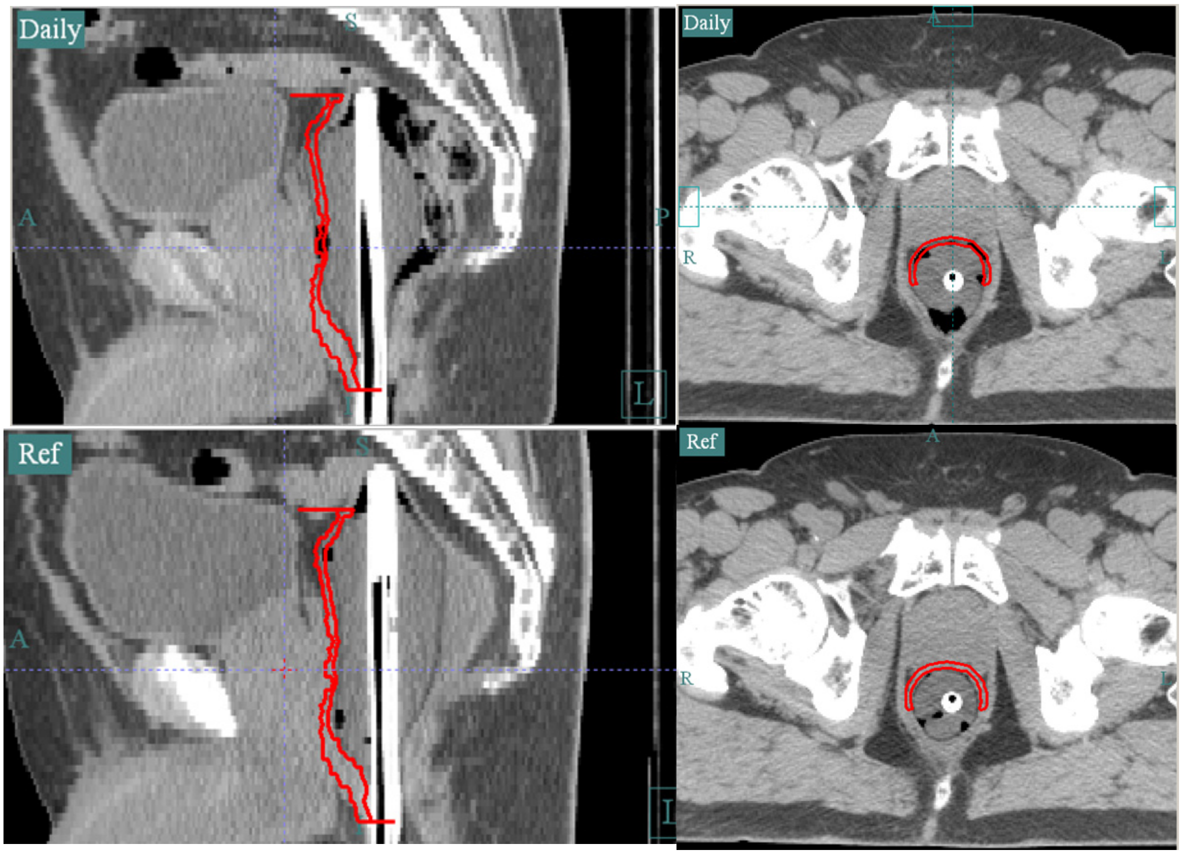

Figure 30: CT registration of ARW in CAT

3.3 Results

3.3.1 Preliminary photon measurements

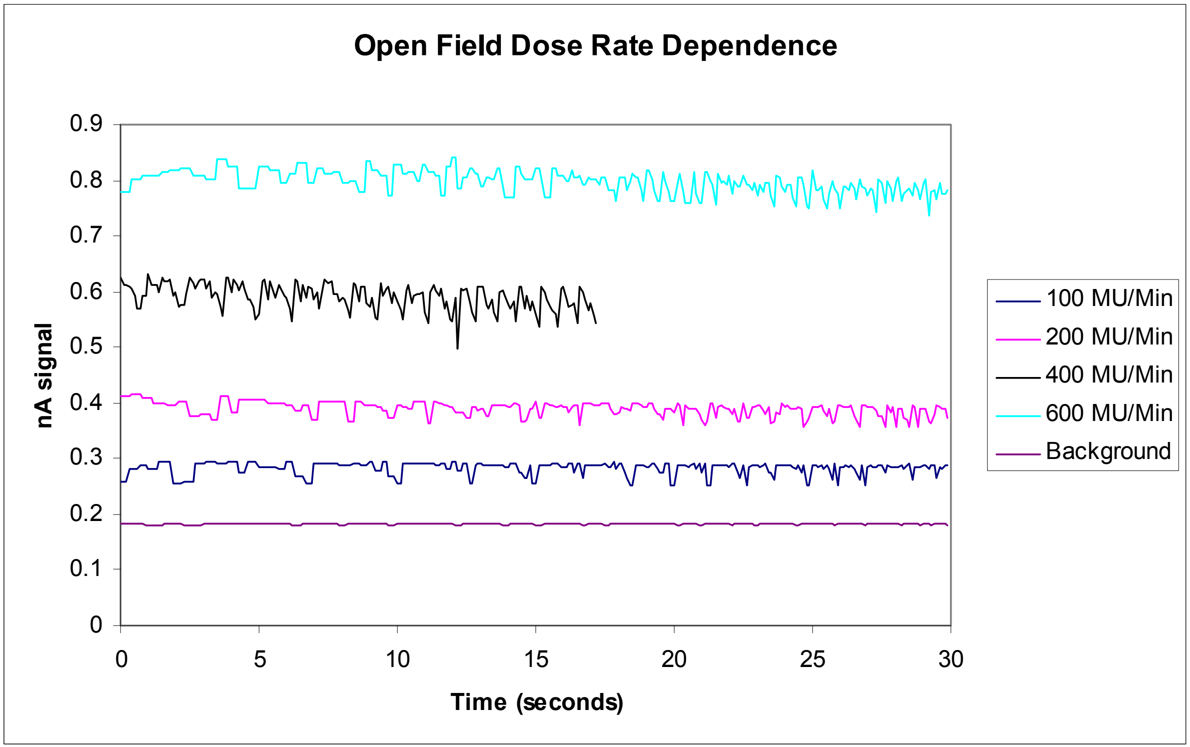

Figure 31: Photocurrent as a function of open-field dose rate

The results of the open-field dose rate dependence were illustrated in figure 31. The ADC for these measurements was set to 60 Hz and internal gain set to one. This was the reason the data appears to have low resolution (both axis). There were also issues with the LABVIEW drivers incorrectly fetching the scaled data, so the effective sampling rate was slightly less than 60 Hz. These issues were resolved in later experiments by changing the baud rate of the ADC, and fully leveraging the dynamic range of the ADC by setting the gain. The periodic signal variances shown in the figures were specific to one linac used in measurement. The magnitude of the variance illustrated in figure appeared to be dependent on the dose rate; however it did not appear to be linearly correlated. The background was very stable, approximately 183 picoamperes. Variation of the 100 and 200 MU/min rate appeared to be similar, as do the 400 and 600 MU/min rates. These measurements were then background subtracted and averaged to investigate the linearity of signal output as a function of dose rate.

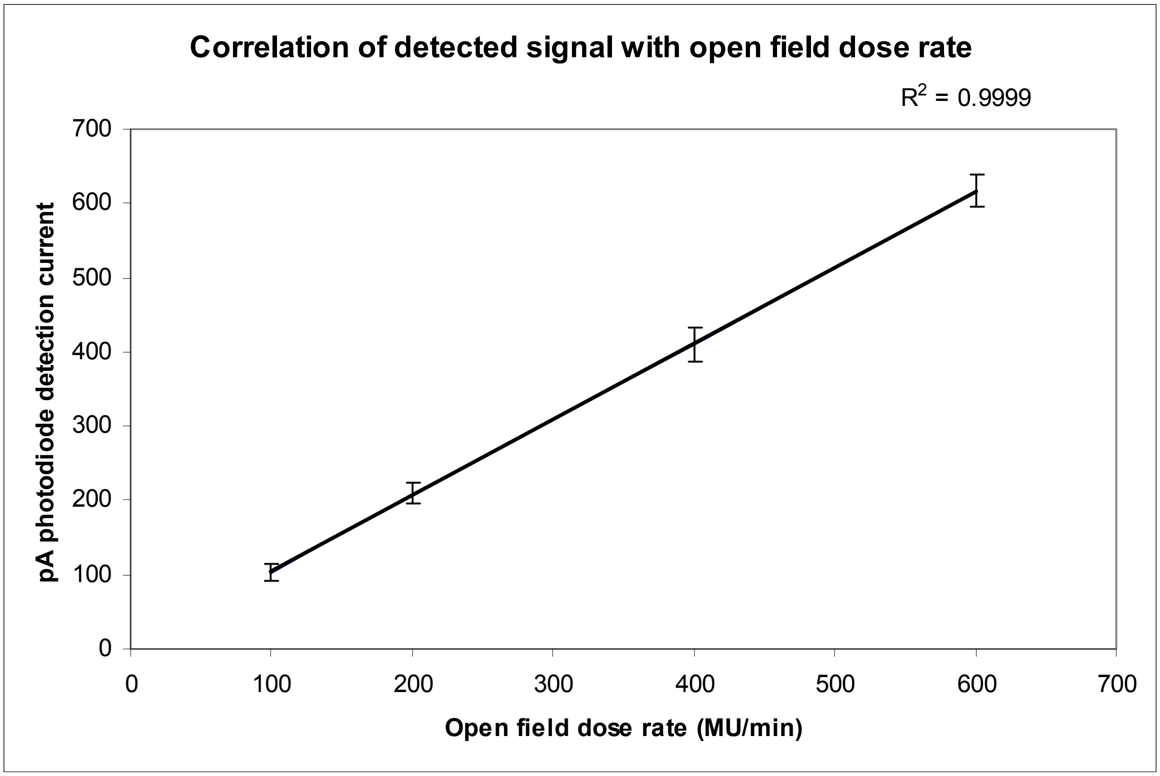

Figure 32: Correlation of mean photocurrent with the open field dose rate

Figure 32 illustrated the average background subtracted photocurrent as a function of dose rate. The photocurrent generated was slightly greater than 1 picoampere per MU/min. The photocurrent was highly correlated with dose rate ($p < 0.001$). The standard deviation, as shown by the error bars in the figure 32 and displayed in Table 1, appeared to be similar in magnitude for the 100 and 200 MU/min dose rates and the 400 and 600 MU/min dose rates.

Dose Rate [MU/min]	Average signal [pA]	Standard Deviation
100	102.70	11.78
200	209.86	13.17
400	410.32	23.54
600	616.86	20.96

Table 1: Photocurrent as a function of open-field dose rate

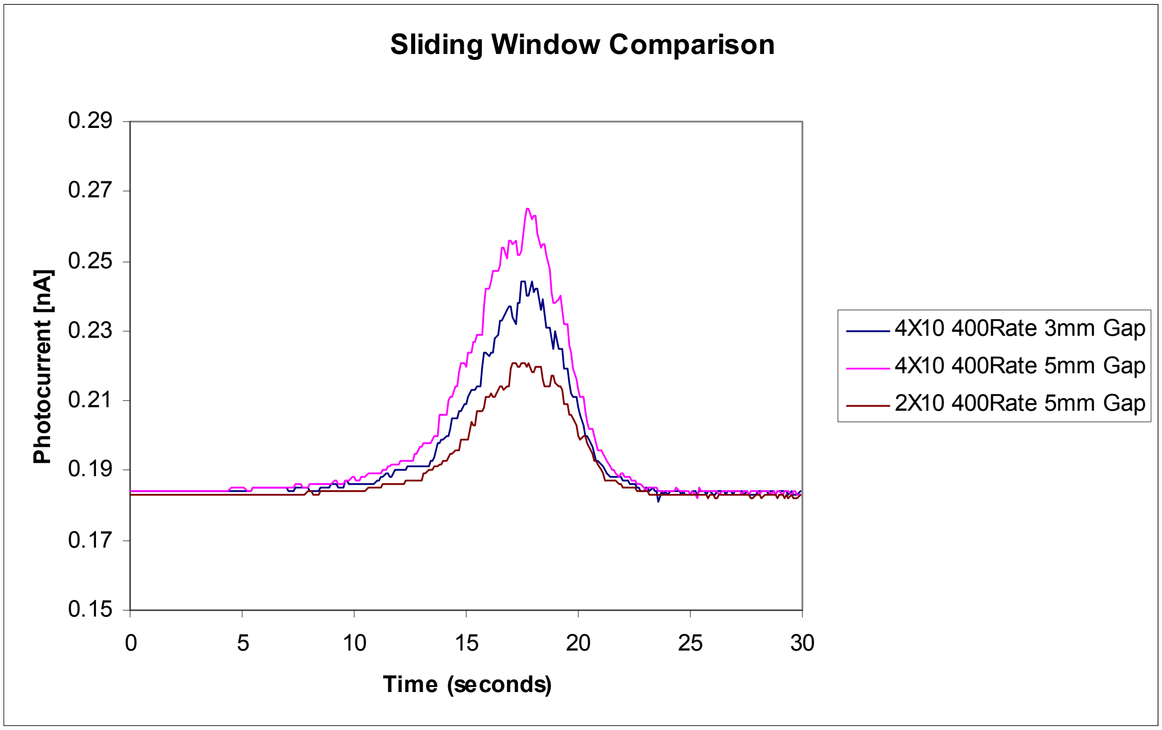

Figure 33: Photocurrent generated by reduced size sliding windows

Figure 33 showed the current generated by a 4cm by 10cm MLC window as it traveled across the beam aperature. The resulting dose was delivered anteriorely through the IMRT film phantom and the detector volume. The measured current peaks as the window reached the fiber axis. We compared the 4 cm X 10 cm X 3 mm window with a 4 cm X 10 cm X 5 mm window and 2 cm X 10 cm X 5 mm window. As we anticipated, increasing the width of the gap increased our signal and reduction of the window length decreased the dose and signal. Reduction of the window length was clearly the dominant of the two factors. If this technique was implemented for IMRT patient set-up, window size reduction could potentially decrease extraneous patient dose.

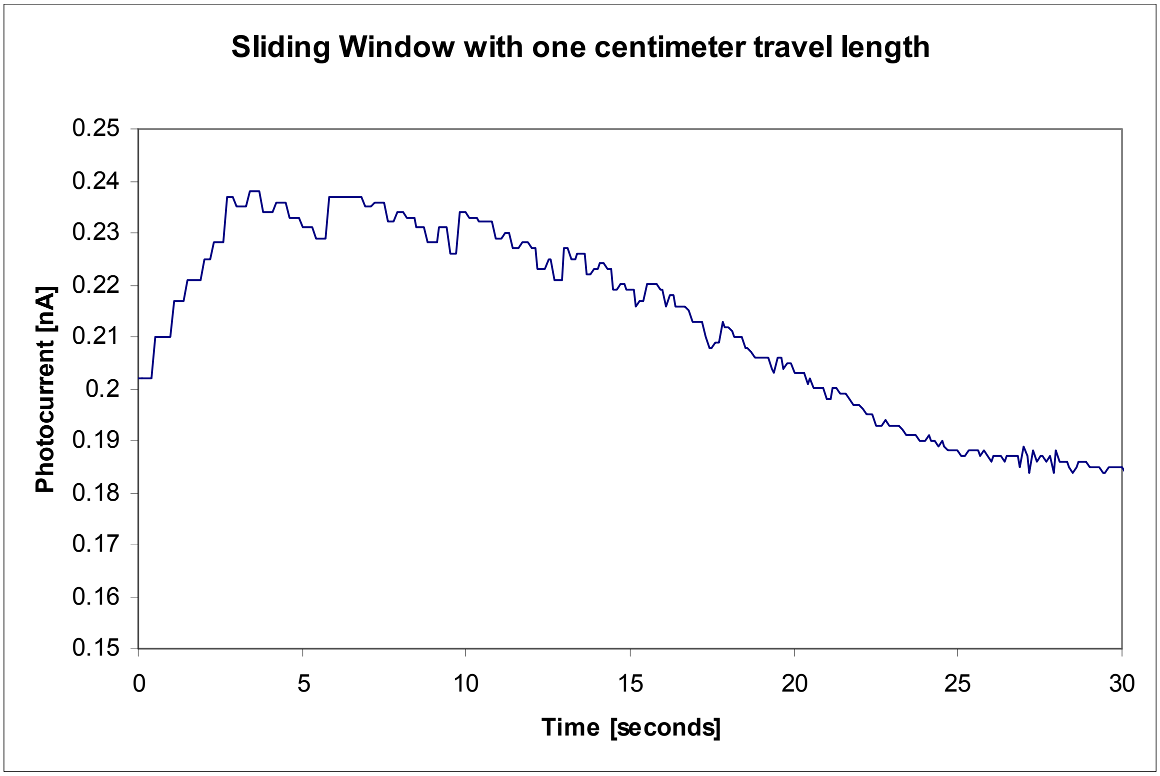

Figure 34: Photocurrent generated from 4X10 cm MLC window with 1 cm travel length

Figure 34 illustrated a 4 cm X 10 cm X 3 mm window with a one centimeter travel length starting five millimeters inside the detector and traveling to the outside of the detector wall. This particular technique could be used localize patients with minimal dose before the treatment. The short buildup region in the first 3 seconds showed the MLCs opening to their 3 mm width. The dose steadily decreased as the window moves away from the position of peak sensitivity in the center of the volume. This figure was used again to correlate the photocurrent generated as a function of sliding window delivered dose as estimated in the Pinnacle treatment planning system documented later in this chapter.

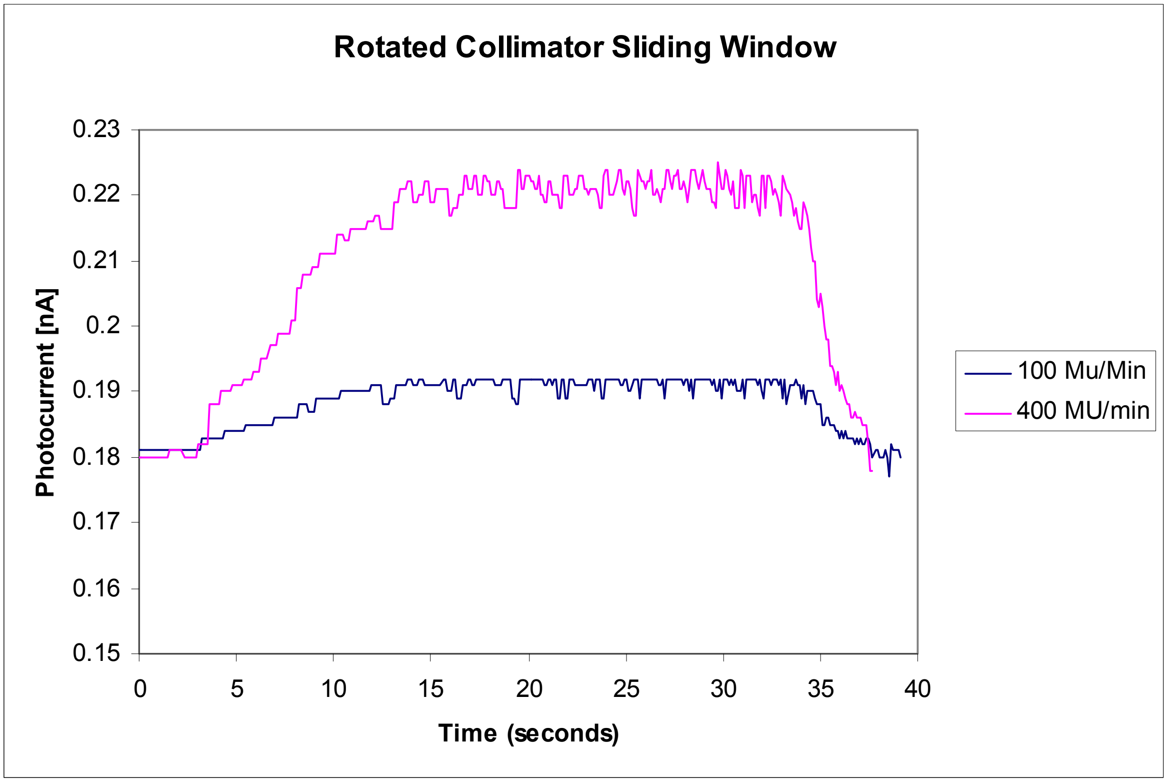

Figure 35: Photocurrent generated from a MLC window traveling up the detector volume

Figure 35 illustrated the photocurrent generated as the window travels towards the fiber face from the bottom of the detection volume. The width of the photon beam penumbra was fairly large, approximately 2 cm, which led to an initial buildup of current signal. Once the dose delivered by the window was completely inside the vial, the output current signal was constant for both dose rates until the window reaches and passes the face of the fiber. This measurement validated Equation 5. The increased capture fraction of photons emitted from any point within the volume by the fiber face was canceled by the decreased cone volume as the window reached the detector.

3.3.2 Anterior Proton Beam Simulation

Figure 36 illustrated the detection of a single proton spill when the anterior detector interface is mid-way through the proton SOBP (5 cm). The measured spill was consistent with the known properties of of the Proton Therapy Center synchrotron. A proton spill from the synchrotron was approximately 0.5 seconds in duration. Each spill was approximately 2 seconds apart. During each spill, the range modulator generated a uniform dose delivery to the entire SOPB. To obtain a uniform dose, the majority of the peaks were weighted near the distal end of the SOBP. The modulator wheel rotated at approximately 6.6 Hz. For each rotation, the wheel completed three modulation cycles, in and out of the detector at the distal end of the SOBP. Based on these properties, we expected our signal to build as the beam moved into the detector and decrease when the beam was retracted. Therefore, our signal had a frequency of 20 Hz within the spill. We observed exactly 10 peaks in the signal with each spill as shown in figure 36.

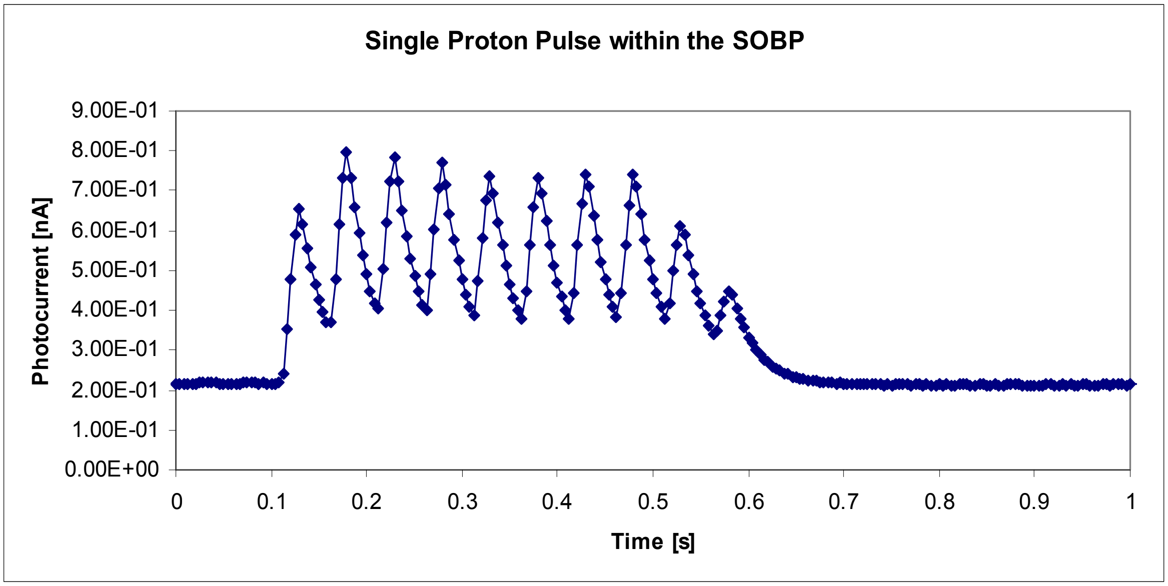

Figure 36: Proton spill with the detector anterior surface in the middle of the proton SOBP

Figure 37 illustrated a series of spills at a position mid-SOBP compared to a series of spills near the therapeutic range. Even with the SOBP well within the detector, the peak signal was not consistent. The cause of these discrepancies was the delivery of the beam in physics mode. When using physics mode, the tolerances of the gantry were relaxed to lower the cost of running the beam. This led to a slight variation in the initial beam energy or loose windowing of the modulator wheel. Either one of these potential effects could cause a variation in the observed range (signal peak) mid-spill. The figure also illustrated that this variation is much more apparent at the distal end of the SOBP (therapeutic range). Theoretically, some range modulation peaks should reach the detector and others should fall short.

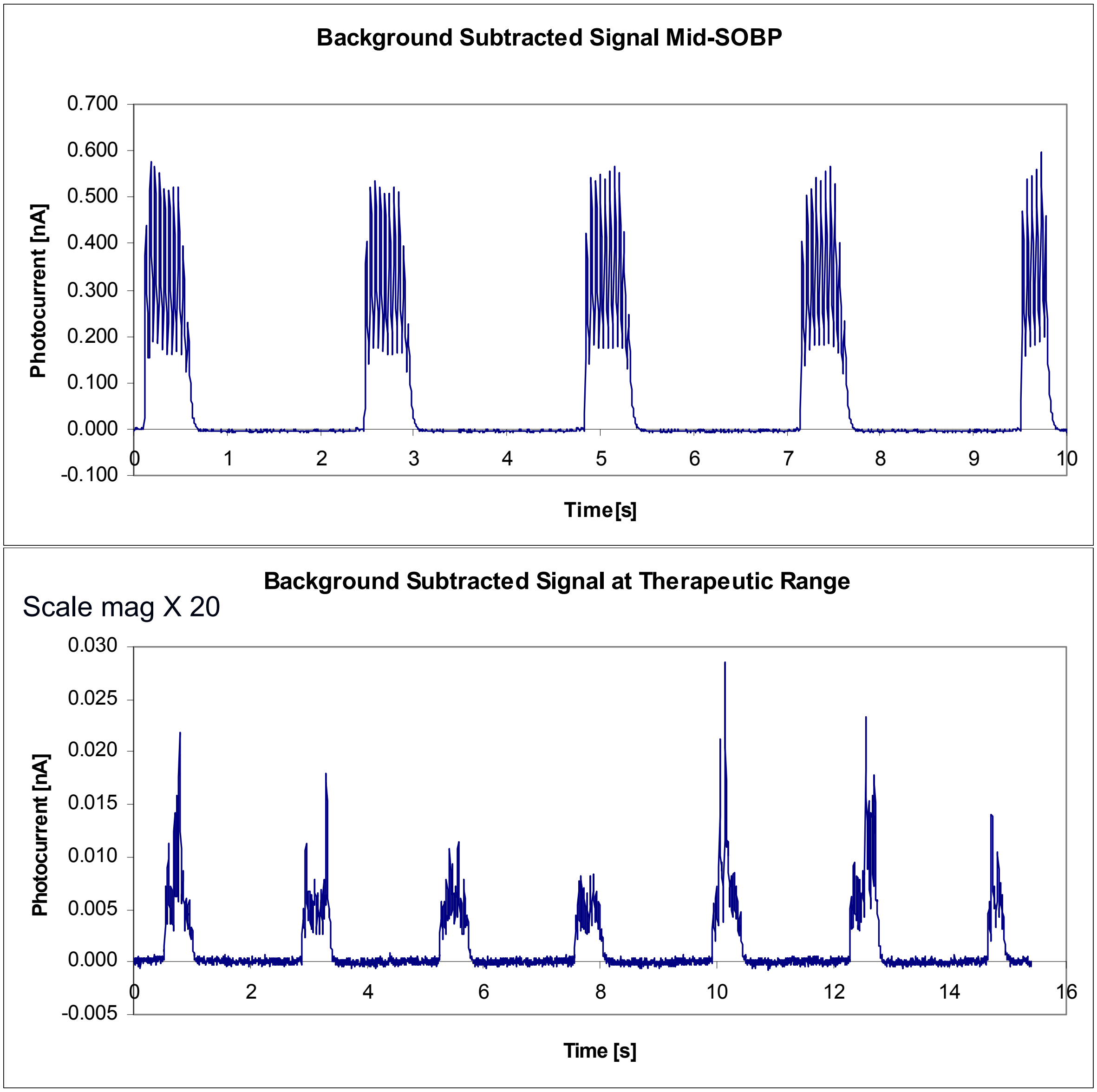

Figure 37: Comparison of proton spills mid-SOBP with spills at therapeutic range

Figure 38 showed the relationship of integrated photocurrent over the 200 MU delivery as a function of SOBP depth within the detector. The relation showed gradual signal buildup in the distal falloff region and linear output in the SOBP region as predicted in Figure 18. Since the relationship diverged from linearity at therapeutic depth, the measurement origin was reset with a bilinear fitting of the signal with the distal falloff and dose within the SOBP. This fit was rounded to the nearest millimeter. The fit predicted the SOBP reached the detector approximately 2 mm further than the measured 11.7 cm inside the phantom to the anterior detector wall. This adjustment was reasonable because the tissue-equivalent material had a slightly higher stopping power than water. The standard deviation of the spills was 19.5% at our original origin (-2 mm position) and decreased to approximately 11% in the saturation region. The linear fit of the measured data in the SOBP region yielded a gradient of 1.0183 nC/cm. Pulse variation was 17% or 0.052 nC at 2 mm depth corresponding approximately 0.51 mm considering the signal gradient in the SOBP. If in vitro detector uncertainty was the only source of uncertainty, our margin to treat with 95% confidence would be approximately 1 millimeter.

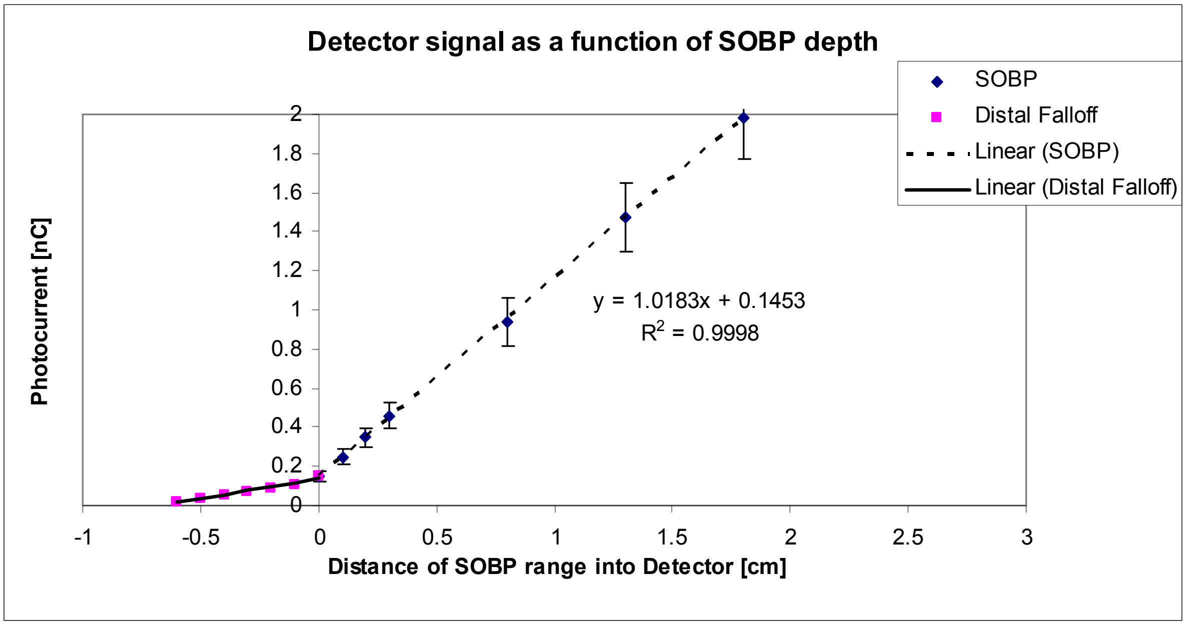

Figure 38: Photocurrent generated as a function of SOBP depth

3.3.3 *In Vivo* treatment Uncertainty

Figure 39 illustrated the agreement between the one-dimensional registration based on the rectal dose/ light emitted and the one-dimensional manual registration of the anterior rectal wall using the CAT, CT-to-CT registration software. The two values were highly correlated and the standard deviation of the difference between the two alignment techniques was 1.1 millimeters, and the average magnitude of differences was 0.76 millimeters.

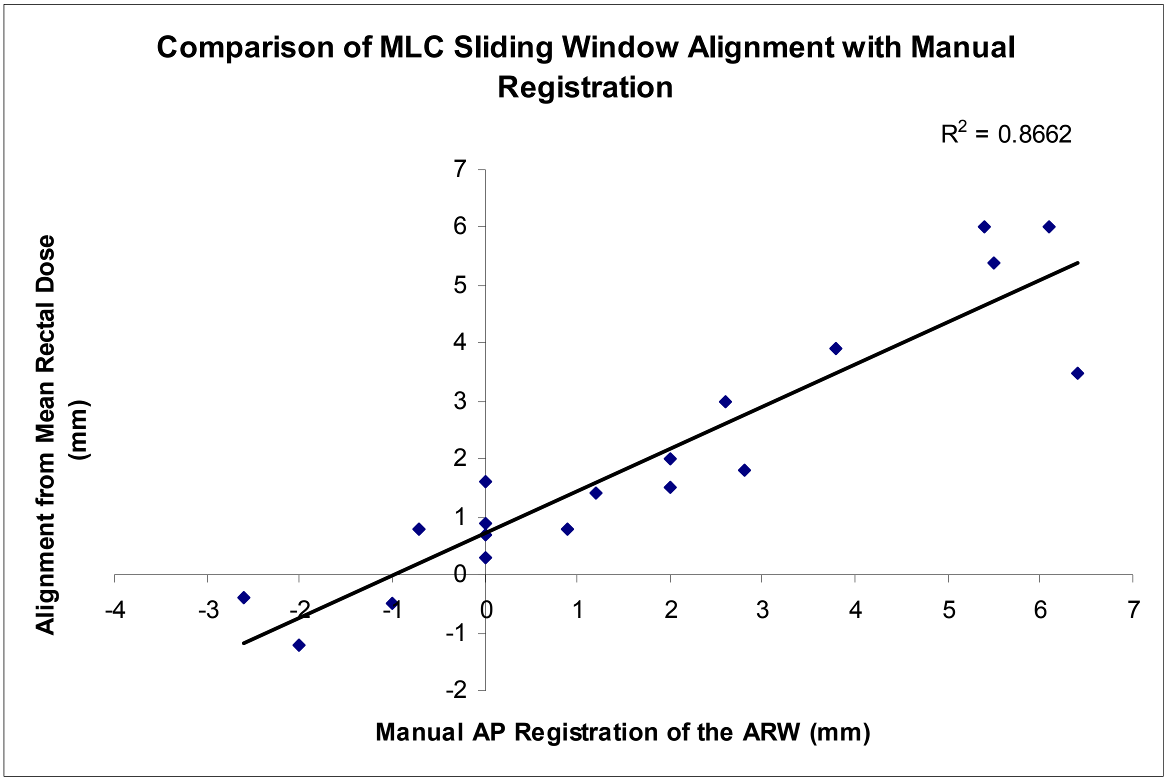

Figure 39: The corrective shifts generated from the sliding MLC technique compared with manual registration

To validate the use of mean dose as a surrogate for light output and photocurrent signal, we compared the current signal in picoamperes with the simulated delivery of the 4 cm sliding window as calculated in the Pinnacle treatment planning system (Figure 40). The original measurement was obtained from Figure 34. The series in blue was the measured current signal with delivery of the 4 cm by 10 cm by 3 mm sliding window. We sampled Figure 34 into 10 equidistant measurements for comparison with the treatment planning dose. Mean dose calculated from the treatment planning system was highly correlated with the measured photocurrent ($p<0.01$)

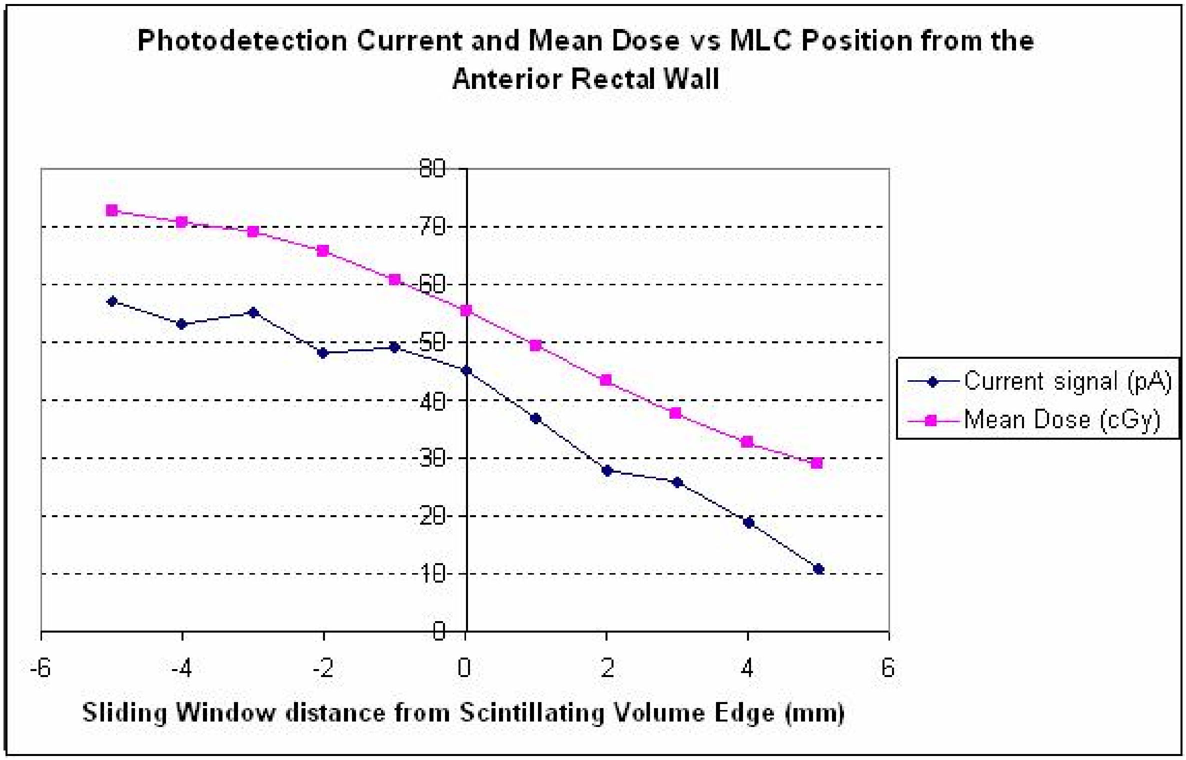

Figure 40: The measured current signal [pA] and mean dose [cGy] as a function of window position.

3.4 Discussion

3.4.1 Summary and discussion of results and aim

In summary, we built a device for detecting the fall-off of an anterior proton beam to reduce range uncertainty during treatment. This device consisted of a liquid scintillation filled rectal balloon with a single fiber machined through the stem at an angle slightly greater than 45 degrees. When the fall-off reached the anterior balloon surface, scintillation light was emitted isotropically in proportion to the dose and corresponding energy deposited within the fiber's collection cone. This light was collected by the fiber and guided to a silicon photodiode. The diode generated current in proportion to the incident light. This current was measured by an electrometer and converted to a digital signal for computer analysis.

Our aim for this chapter was to design an *in vivo* proton beam detection device located within a rectal balloon that could detect the distal fall-off of a proton beam within 2 mm (95% confidence interval). To evaluate our design, we measured the photocurrent produced by an anterior proton beam in our anthropomorphic phantom and detector prototype as a function of SOBP depth from the anterior interface of the detector. By investigating the signal gradient and variation of the individual proton spills, we approximated the uncertainty of positioning the patient with each proton spill in real-time. The 95 % confidence interval at 2 millimeters from our corrected interface was approximately 1 mm. We wanted to extrapolate this technique and corresponding uncertainty for use in a patient. Since the total light output was a function of the energy deposited in the scintillator and the rectal volume was nearly constant in patients with endorectal immobilization, we used mean dose as a surrogate for light output in the treatment planning system. The relation of beam position with rectal dose was a function of the distance of the beam from the prostate-rectal interface and the shape of the balloon. Therefore we simulated set-up with the device by registering patient's prostate-rectal interface with an MLC sliding window induced rectal dose. We then compared alignment with the mean dose gradient to manual one-dimensional alignment with CT registration software to isolate output variation induced from shape deformation of the balloon. The standard deviation of agreement was 1.1 millimeters. Assuming that the *in vitro* and *in vivo* uncertainty sources were independent and random, the composite 95 % confidence interval was approximately 2.4 millimeters in each direction. Thus, we narrowly missed our aim of 2 millimeter precision. However, considering the study limitations and the potential for improvement as discussed in the proceeding sections, our initial 2 millimeter guess was an excellent. If we relax our 95% confidence criteria to 90%, the interval is exactly 2.0 millimeters.

3.4.2 Design limitations

There were several limitations in design, implementation, and testing of our device precision. The first limitation of our device was the use of liquid scintillation as our radiation detector. The solution was slightly toxic and therefore required special handling, storage, and prophylactic safety measures for use in patients. The solution was also noxious and difficult to clean when spilt.

Additionally, exposure of the liquid to air resulted in signal quenching, so airtight storage was necessary to ensure signal integrity.

The second limitation of the detector was the energy-dependent quenching of the solution in the distal fall-off. Only a small fraction of the energy deposited within the solution was converted into light. For the ideal scintillator, the fluorescence yield was proportional to the energy loss as in equation 6.

$$\frac{dL}{dX} = S\frac{dE}{dx}$$

Equation 6: Ideal scintillator output

In equation 5, the light output of the scintillator per unit pathlength was proportional to the linear stopping power multiplied by the efficiency of the scintillator. This relation held for electron energies in excess of 125 keV, but this threshold was significantly higher for larger charged particles such as protons (80). To account for LET-dependent quenching from damage molecules in the solution, an additional term was added to the denominator in Birk's formula (92) (Equation 7).

$$\frac{dL}{dx} = \frac{S\frac{dE}{dx}}{1 + kB\frac{dE}{dx}}$$

Equation 7: Birk's formula for quenched scintillator output

For low LET radiation, this formula reduces to equation 6 and the light output is directly proportional to the energy deposited in the solution. For high

LET radiation, scintillation efficiency approached the empirically determined value, S/kB, where B was the probability of damaging a fluor in the solution and k was the probability that the damaged molecules will quench the excitons in the solution. These terms were unable to completely account for quenching, which continued to increase with increasing LET of low energy charged particles.. This additional quenching may have been due to interaction between mutually excited electrons as the ionization density was increased(93). To account for quenching that continued to scale with decreasing energy, an additional quadratic term was added to the denominator in Equation 8.

$$\frac{dL}{dx} = \frac{S\frac{dE}{dx}}{1 + kB\frac{dE}{dx} + C\left(\frac{dE}{dx}\right)^2}$$

Equation 8: Birk-Chou model for LET-dependent quenching

The three terms, S, kB, and C were experimentally fit and provide good agreement with measured values While several authors have recently discussed liquid scintillation for external beam dosimetry (94, 95), few have modeled proton quenching in scintillators ((96), Beddar and Siebers 1995) and one author experimentally determined quenching in BC-531 (97). Beddar et al. used a plastic tank and CCD camera system for quality assurance dosimetry of a proton pencil beam. Scintillation measured depth dose deviated from the measurements made with a parallel plate ionization chamber from three factors, the focal depth of the lens system, optical blurring, and scintillation quenching. The absolute efficiency of the scintillator at the Bragg peak of a 120 MeV beam was approximately 70%. More troubling for relative dosimetry purposes, was the observed degradation (widening) of the falloff, however, this was primarily due to optical blurring and would not be present if the light was collected closer to the source.

We anticipated a very small deviation (sub-millimeter under-estimation) in the position of the distal fall-off when the quenched depth dose was integrated with our detector. This value would be approximately the distance to agreement (relative) between the quenched depth dose and measured depth dose. Fortunately, the strongest factor in quenching was the initial proton energy and depth. Therefore, most of the deviation would be systematic and could be mathematically modeled with Monte Carlo (96). Then the predicted range with our technique could be corrected based on the initial energy of the proton beam and the measured depth.

Another potential limitation of our design was due to the dependence of light collection efficiency on the coupling efficiency at each optical interface (98). Although we do not couple to our scintillator as in scintillating fiber dosimetry, we can still lose a large amount of light at the coupling of our fiber to the face of the photodiode. Loss of some of the light at the coupling was not detrimental to our goals, since we observed signal well above background while still in the fall-off portion of the beam. However, we maintained the same coupling at the photodetector for all of our measurements. The only way to maintain identical coupling for in vivo application of our device was to use the same exact system for all measurements. Reuse of the balloon between patients may not be feasible. Therefore, we would re-couple at the diode if the balloon and complete fiber length were fabricated together or we could apply a fiber adapter at the base of the balloon and reuse the length of fiber leaving the treatment room. The variation in the re-coupling with a fiber adapter would be similar to the measurements of Ayotte et al. (98) who investigated variance in coupling to scintillating fibers. They reported 10% variance with proper fiber preparation and consistent procedures. This variance would significantly contribute to the spatial resolution of our detector and potentially increase the distal margin needed to ensure treatment confidence.

3.4.3 Study limitations

The first study limitation was the operation of the synchrotron gantry in physics mode. When in physics mode, the tolerances for proton energy and range modulator windowing were looser. Therefore much of the observed variation in the proton spills may not reflect treatment in clinical mode in an actual patient. To better estimate the precision of our technique, we should repeat the experiment by generating a treatment plan in Eclipse and delivering the plan in clinical mode. We could repeatedly deliver the plan with different amounts of degrading material in the beam to generate the sensitivity of our detector as a function of SOBP depth. Since the measured precision with this technique should be considerably less, we could still establish feasibility with our previous measurements.

The second study limitation was the use of photon mean dose in Pinnacle to estimate the *in vivo* uncertainty of our device. Mean dose was an excellent surrogate for total light emitted inside our balloon and light collected with our initial prototype design. Our latest prototype was only sensitive to the depth dose between the fiber and anterior rectal wall. The light collection of our prototype along with the sharper dose fall-off of the proton beam in the balloon should lead to a much smaller *in vivo* detection precision. Since the precision measured was close to our stated aims, we deferred these measurements to a later date.

The final limitation of our study was the ability of the registered plan to cover the clinical target volume. Assuming we registered the plan to a point on the anterior rectal wall, deformation of the target organs, particularly rotation (44), may move the target slightly out of the treatment field. Use of two fibers, one at the base of the prostate and one at the apex, could theoretically detect rotation during treatment. The precision of each fiber should be identical to our measurements. Proper range correction to account for a rotation in the target organs could be challenging.

3.4.4 Alternative range verification techniques

Lu et al (99, 100) has investigated the use of point dosimetry (MOSFET-based) at the anterior rectal wall at MGH for in vivo range verification. This method exploited the range modulation in the proton SOBP and approximated the residual range of the proton beam based upon when the Bragg peak reaches the point detector within the patient. Each point within the Bragg peak had a unique periodic dose rate was used as a “ruler” for in vivo range verification. The precision of this technique was dependent upon many factors such as variation of the spectral fluence at depth caused by heterogeneities in the patient. It was also highly dependent upon the temporal resolution of the detector, since their technique was dependent on reproducing the dose rate at a point with fidelity.

At this point in time, the MGH group does not have the capability to synchronize their measurements with the range modulator wheel and gantry *in vivo.* They have proposed a second method for range verification using only the dose measured at a point at the anterior rectal wall. Liquid scinitllator was selected for this thesis due to its sensitivity in the SOBP region of the beam. The method that Lu et al proposed artificially created a gradient in the SOBP by treating with two beams, one with increasing dose in the SOBP and the second with decreasing dose in the SOBP. The sum of these two beams generated a uniform dose in the SOBP. They then have an algorithm that reconstructed the range based on the ratio of the doses delivered to the point by both beams with approximately millimeter precision. This method could provide reliable interfractional correction, however real-time correction would be slightly more challenging.

Another potential range verification method was PET verification (101-104). When the patient's tissues are irradiated with protons, positrons were emitted from activated isotopes e.g., ${}_{11}$C, ${}_{10}$C, ${}_{15}$O within the patient. The activity can then be predicted based on the range of the protons, total dose, dose rate, and dose distribution within the patient. The positron decay can be measured either in-room or shortly after therapy by moving the patient into a nearby imaging suite. The primary limitations of this method for range verification were the relatively short life-time of the isotope, biological wash-out, and the inherently low resolution of the imaging modality. If the method were used for real-time tracking, i.e. 4DPET, the disadvantages of the modality would be compounded with the relatively low counting statistics from obtaining images over a very short duration. While PET verification had the potential to improve proton therapy for all disease sites, its performance for verification at the anterior rectal wall will not out-perform direct measurement techniques.

3.5 Specific Aim 1 conclusions

A scintillation filled endorectal balloon was designed for real-time determination of an anterior proton beam’s range. The goal was 2 millimeter precision and that goal was nearly met with an estimated 95% confidence interval of 2.4 millimeters. Given the precision of the initial measurements, use of this technique for real-time adaptive proton therapy with our technique was certainly feasible. The estimated *in vitro* precision of our technique also exceeded the measured precision of other range verification techniques and was simpler to clinically implement. Further development of this technique was needed to translate this technology into the clinic.

Chapter 4: Development of a dual wedge range shifter

4.1 Introduction

Specific Aim 2: Develop a computerized external proton beam range shifter to modulate proton beam energy/range.

*Working hypothesis: A*n external proton beam range shifter can modulate proton beam energy/range and localize the distal fall-off of a single anterior proton beam to the anterior rectal wall within 2 mm (95% confidence interval).

To adapt the incoming beam energy to the daily variation of the rectal wall position, a range shifter was placed in the beam path between the end of the proton beam nozzle and the anterior skin surface of the patient, as diagramed in Fig. 12. The range shifter was a pair of triangularly shaped Lucite attenuators, one which was fixed and another which was dynamically adjusted. The thickness of the range shifter was controlled precisely by a stepping motor, which controlled the horizontal positions of two triangular objects. A thicker range shifter in the beam path will pulled the distal proton beam edge anteriorely from the prostate and rectum interface, sparing the rectum from excessive (overshooting) radiation. A thinner range shifter, on the other hand, increased the proton range to ensure that the posterior coverage of the prostate target to the adequate prescribed dose level. The goal for this chapter was to develop this wedge shifter based on observation of anatomic deformation of prostate cancer patients and determine the precision of the range system to degrade the proton's range from a calculated value.

4.2 Methods and materials

4.2.1 Degradation of the beams energy and range

Most proton synchrotrons or cyclotrons employed some method of reducing the proton's energy and range by placing attenuating material in the beam's path. Inside this material, proton's lost energy from multiple Columbic interactions with electrons resulting in a reduction of the proton's energy and residual range (105). Some of the protons interacted with the nuclei in the attenuating material and deposited most of their energy, resulting in a loss of proton fluence and dose delivered to the target. Since the energy loss of the proton per unit pathlength was proportional to the inverse square of its energy, placing attenuating material upstream from the target substantially reduced the proton's range while retaining most of the energy for deposition within the target (106).

In beam lines that deliver high energy protons, attenuating plates were used to coarsely step the proton energy to the desired range, as in the Proton Therapy Center – Houston (107) and the Paul Scherrer Institute in Switzerland (108). In beam lines for lower energy protons that treat small superficial legions such as ocular tumors, a wedged attenuator was placed in the beam's path to finely degrade the proton's range to conform to the distal edge of the tumor. This technology was used at several proton facilities including the Hahn-Meitner-Institut (HMI) in Berlin (109, 110) and at Massachusetts General Hospital (MGH) (111, 112) The latter type of range degrader was built in order to localize the distal edge of the proton spread out Bragg peak (SOBP) with a high degree of precision.

4.2.2 Preliminary determination of depth variation

Construction of the external collimation system required some knowledge of the magnitude of daily or inter-fractional and intra-fractional beam range corrections. The wedges had to be large and steep enough to correct for the majority of anatomic variations and calculation based variations encountered during a patient's fractionated radiotherapy. To estimate the range of variations in actual patient treatment, we measured the distance from the abdomen to anterior rectal wall in the mid-sagittal plane near the superior prostate and proximal seminal vesicles in patients without rectal balloon immobilization (Figure 41). Previous studies indicate that both interfractional and intrafractional variation of the target organs was greatest at the level of the seminal vesicles (44, 61).

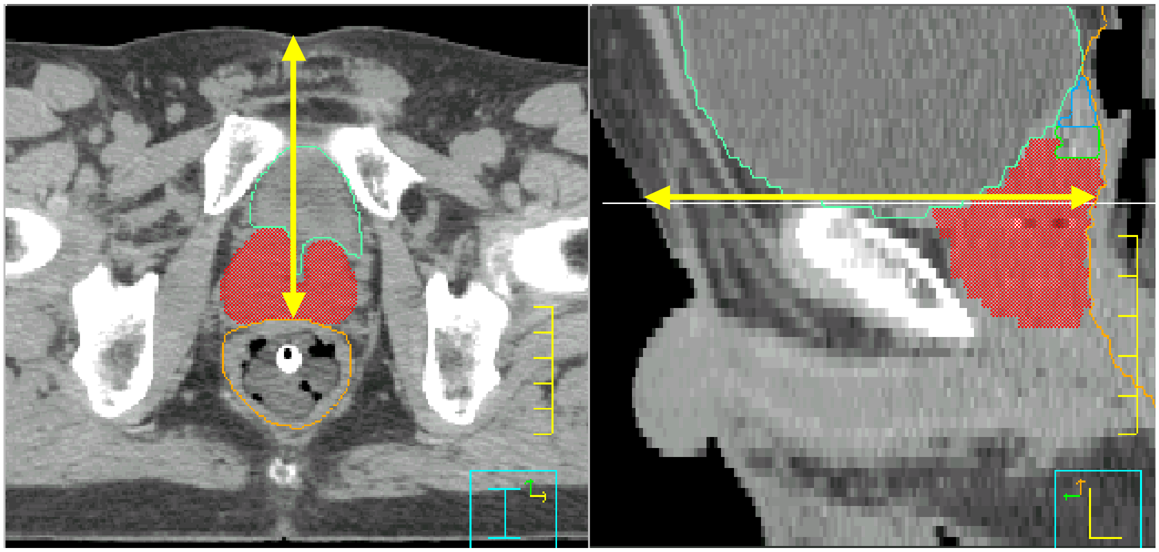

Figure 41: Measured depth from the abdomen to the anterior rectal wall

Taking advantage of a previously completed repeat CT imaging research protocol, the mean depth was calculated for each patient and subtracted from each weekly CT image set for 30 patients and a total of 154 depth variations. One standard deviation of variation was 4.5 millimeters (Figure 42). The total range of beam attenuation for our patient set-up device had to be capable of at least 9 millimeters (2 standard deviations) range attenuation both anteriorely and posteriorely to correct for anatomic variation in 95% of cases. Some additional margin was added to the nine millimeters to account for potential variation in the calculated range.

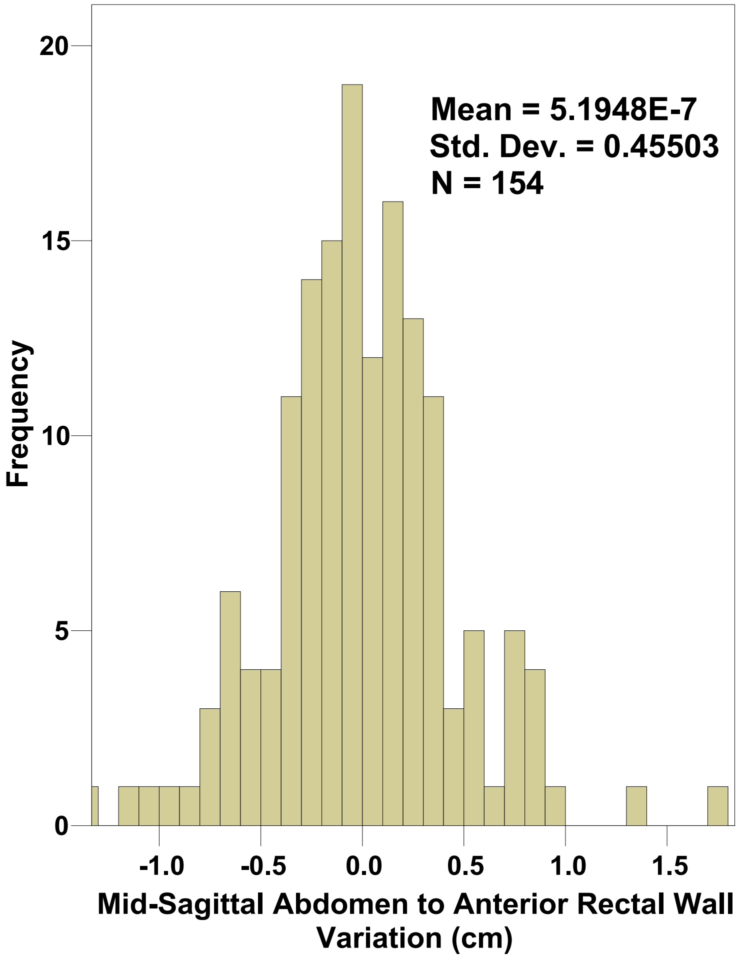

Figure 42: Measured depth variations to the anterior rectal wall

The absolute depth to the anterior rectal wall was also important for wedge design. The mean depth to the anterior rectal wall from the abdomen was 13.8 centimeters with a standard deviation of 1.5 centimeters. The maximum therapeutic energy of the synchrotron at the PTC was 250 MeV. After scattering, shifting, and monitoring in the nozzle, the maximum range of this energy was approximately 28.5 centimeters. Considering the depth to the target, the wedges could be no more than 11-12 centimeters in height.

4.2.2 Wedge system design

The relationship between the wedge dimensions and the total range of attenuation was illustrated in Figure 43. In the wedges' reference position, the total physical thickness of the wedge was the product of the wedge length and the tangent of the wedge angle, or the maximum height of the wedge. The distance that the dynamic wedge can travel was limited by the need to maintain a uniform thickness across the beam. Thus, the maximum and minimum depths were limited by the length of the wedges and the width of the treatment beam. For the case for prostate treatment, we assumed that the width of the beam would be approximately 10 centimeters. The total attenuation range was the difference in the length of the wedges and the beam multiplied by the tangent of the wedge angle.

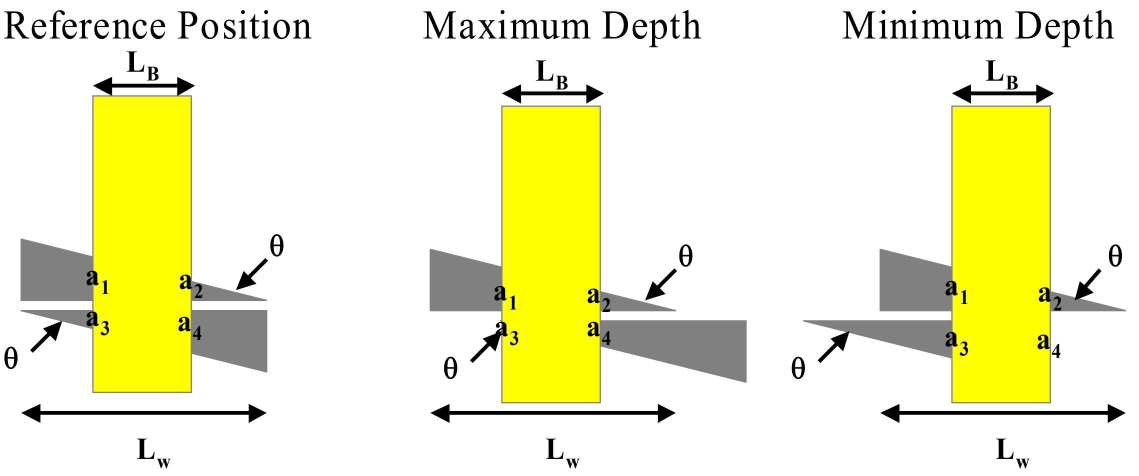

$a_1 + a_3 = a_2 + a_4 = L_w \tan\theta$

$a_1 = a_2 + a_4 = 0.5(L_w + L_B) \tan\theta$

$a_1 + a_2 = a_3 + a_4 = (1.5L_w - 0.5L_B) \tan\theta$

$$\text{Total Attenuation Range} = (1.5L_w - 0.5L_B)\tan\theta - 0.5(L_w + L_B)\tan\theta$$
$$= (L_w - L_B)\tan\theta$$

Figure 43: Relation of attenuation range to wedge width and angle

We selected a wedge angle of 26.5 degrees. The tangent of this angle was one-half. The physical thickness of the wedges would change by exactly one-half the distance the dynamic wedge was moved into or out of the field. For our prototype design, we created 20 centimeter square wedges that were 10 centimeters in height. These dimensions allowed for 2.5 centimeter correction in either direction. In hindsight, we should have created these wedges slightly smaller. Additional attenuation added distal edge degradation, additional lateral scatter, and generated additional neutrons.

After determining the dimensions of the dual wedge range shifter, we selected an appropriate commercial stepping motor, controller, and mountable slide. The Velmex Bislide (Velmex, Inc., Bloomfield, NY) commercial system fit our specifications (Figure 44). The total travel length of the motor was 10 inches.

The motor's precision was approximately 1/1000", ensuring that the precision of our range shifter would meet our criteria as long as the wedges were well constructed. The screw index was one tenth of an inch per revolution. The stepper motor also included commercial software; however, Labview was used to interface the range shifter with the beam detector in our experimental setting for future interfacing with our detector from aim 1.

Figure 44: Velmex Bislide stepper motor

We built a custom attachment from the motor carriage of the Velmex Bislide to the top wedge (Figure 46). The bottom wedge was inverted and attached to the bottom side of our measurement cart to achieve uniform range modulation across the field (Figure 45). Our measurement cart had a second rack below the wedges to place phantoms for measurement.

Figure 45: Mobile cart for mounting wedge system

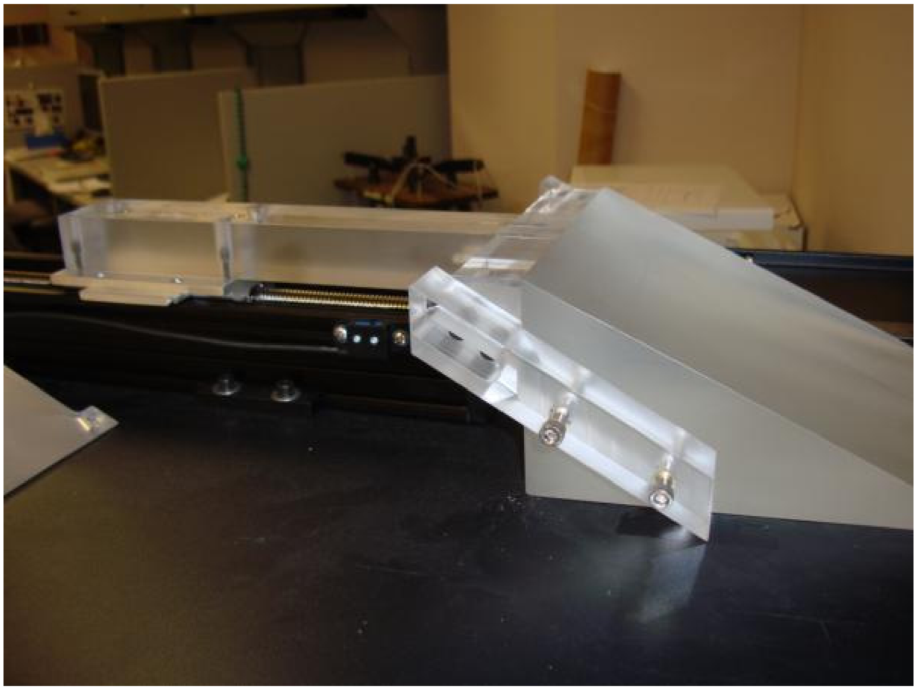

Figure 46: Wedge mounted to the carriage of the stepper motor

4.2.3 Experimental methods

The first experiment determined the water equivalent thickness of our dual wedge range shifter. The proton beam was set to 23.5 cm depth. A TG-51 single axis water phantom and Markus parallel plate ionization chamber were positioned beneath our wedges on our cart rack (Figure 47). The proton depth dose through the distal falloff was measured with the wedges in place (10 cm physical thickness) and with the wedges replaced with calibrated solid water blocks of 6 cm thickness. The measured range of the depth dose with the 6 centimeters of calibrated Lucite build-up material was subtracted by 6 cm to determine the range of the beam without any buildup material in place. The difference between this value and the measured range of the beam with the wedges in place yielded the total water equivalent thickness of the wedges. By dividing this value by ten centimeters, the total thickness of the wedges, the relative water equivalent thickness of the Lucite in our wedges was calculated. This value was necessary for calculating the distance to move our motor to generate a desired adjustment in depth.

We then calculated the distance necessary to move the motor to shift the proton beam by a calculated -1cm, -5 mm, 5 mm, and 1 cm in depth (greater than 2 SD from Figure 42). These values were twice the desired range adjustment due to the angle of the wedge divided by the relative water equivalent thickness of our wedges. After adjusting the proton beam by our calculated amounts from our reference position, the depth dose was measured in our scanning water phantom. The depth of R50 was then estimated by linear integration between our measurement points and these depths were compared to those predicted by our calculation. The deviation between the range that we calculated and the measured range would generate the error in the range correction. The standard deviation of these errors was an independent source of uncertainty for determination of the composite distal margin in aim 3.

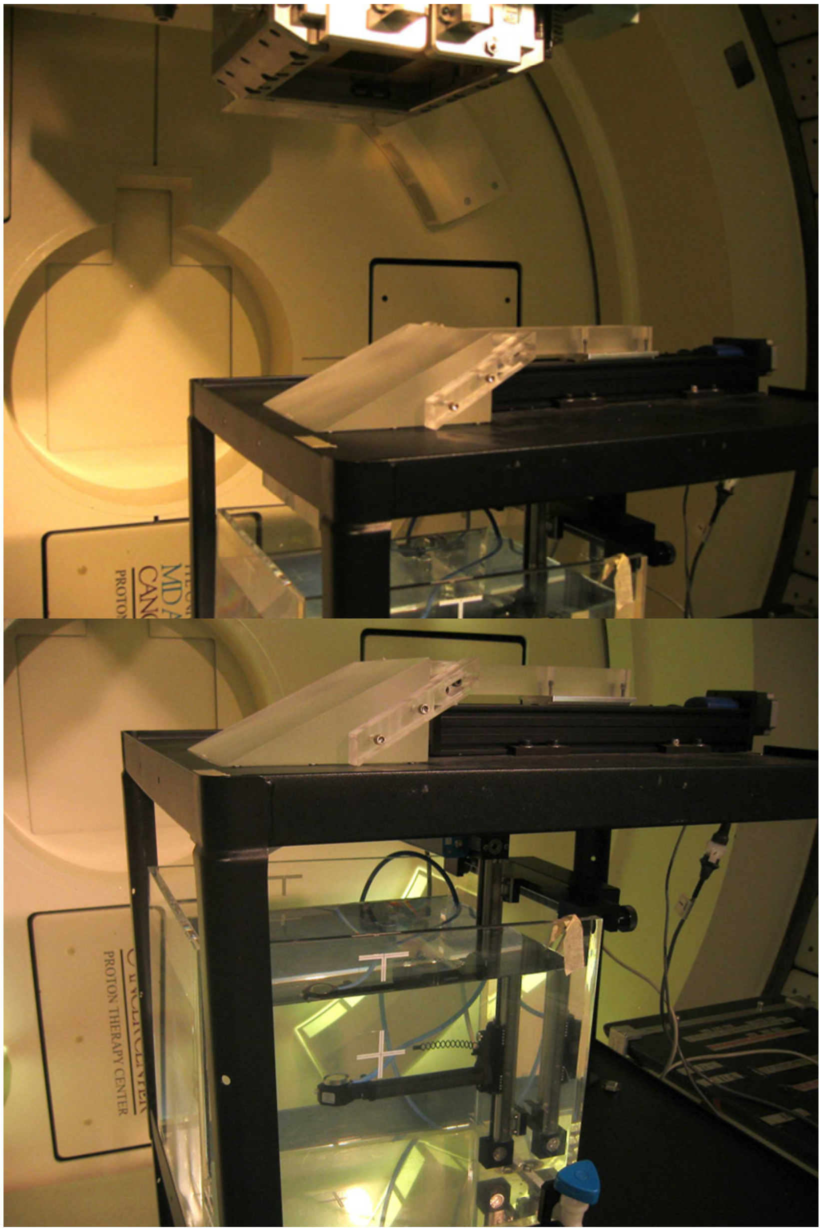

Figure 47: Experimental set-up for wedge precision

4.3 Results

4.3.1 Calculation of the RWET of the wedge system

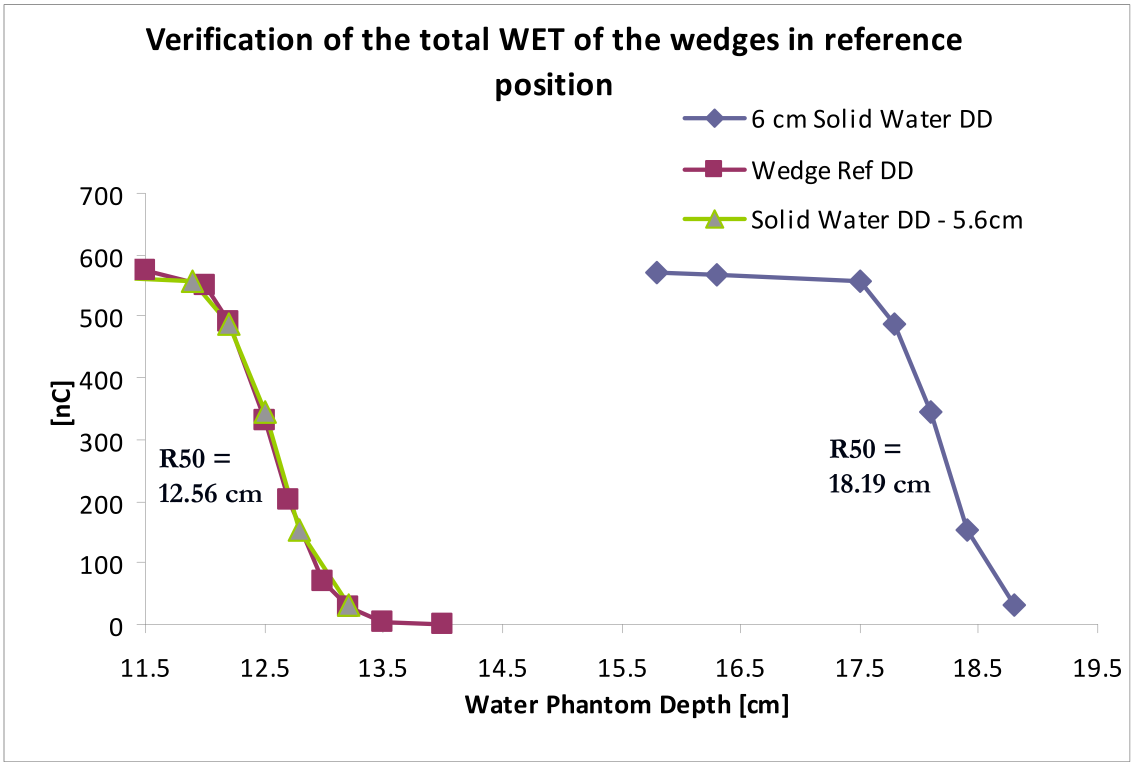

Figure 48: Calculation of RWET of wedges from measurements

Figure 48 illustrated the two depth dose curves measured to determine the relative water equivalent thickness of the wedges. The blue series was the depth dose with the 6 centimeters of water equivalent material in the beam. The red series was the depth dose with the wedge in the reference position (10 centimeters physical depth). The green series was the depth dose with the 6 centimeters of build-up material that has been shifted by 5.6 centimeters for visual reference. As shown in the figure, the distance to agreement between the two relations was 5.6 cm resulting in a measured total WET of 11.6 centimeters and a RWET of 1.16 when compared to water.

4.3.2 Wedge precision determination

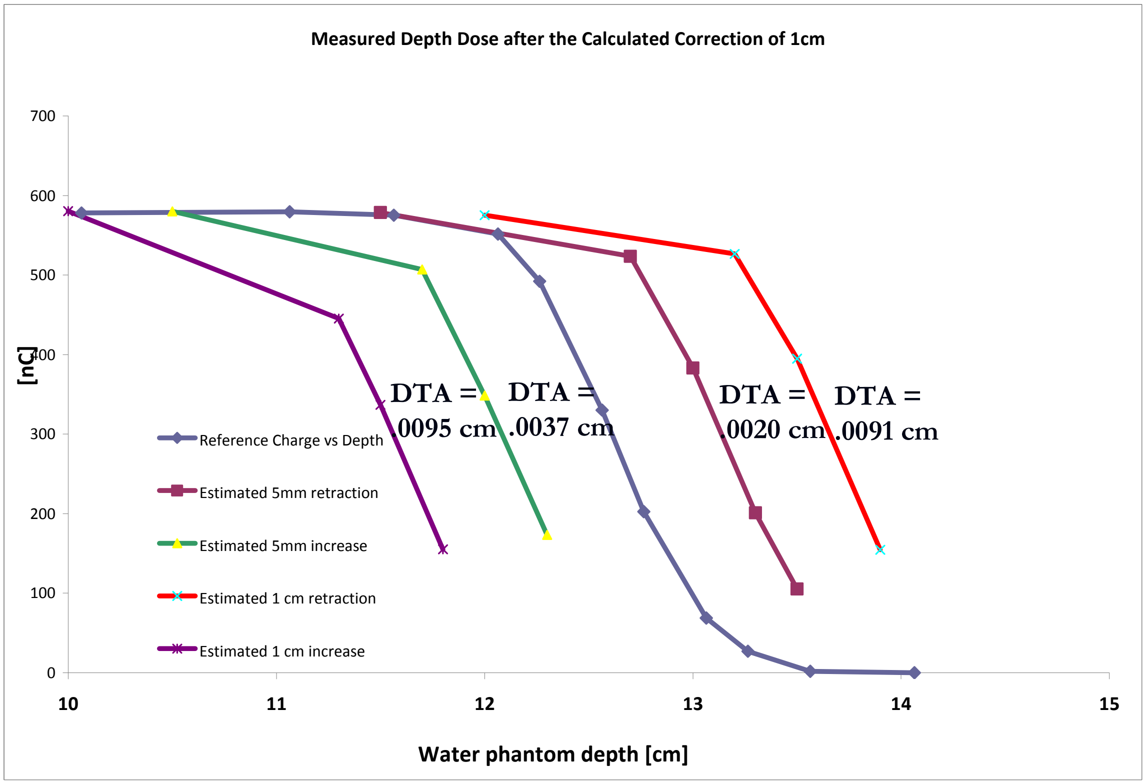

Figure 49: Measured depth dose curves after calculated shifts

Figure 49 illustrated the measured depth dose curves after a calculated shift of -10, -5, 5, and 10 millimeters. For each curve, the 50% range was estimated by linear interpolation between the data points. These values were then compared with the estimated 50% range on the reference depth dose curve. The absolute distance to agreement between the measured 50% range and the calculated shifts were shown next to each curve. Additionally, the calculated range shifts were highly correlated with the measured shifts (Figure 50). The standard deviation of the distance to agreement was 0.04 mm.

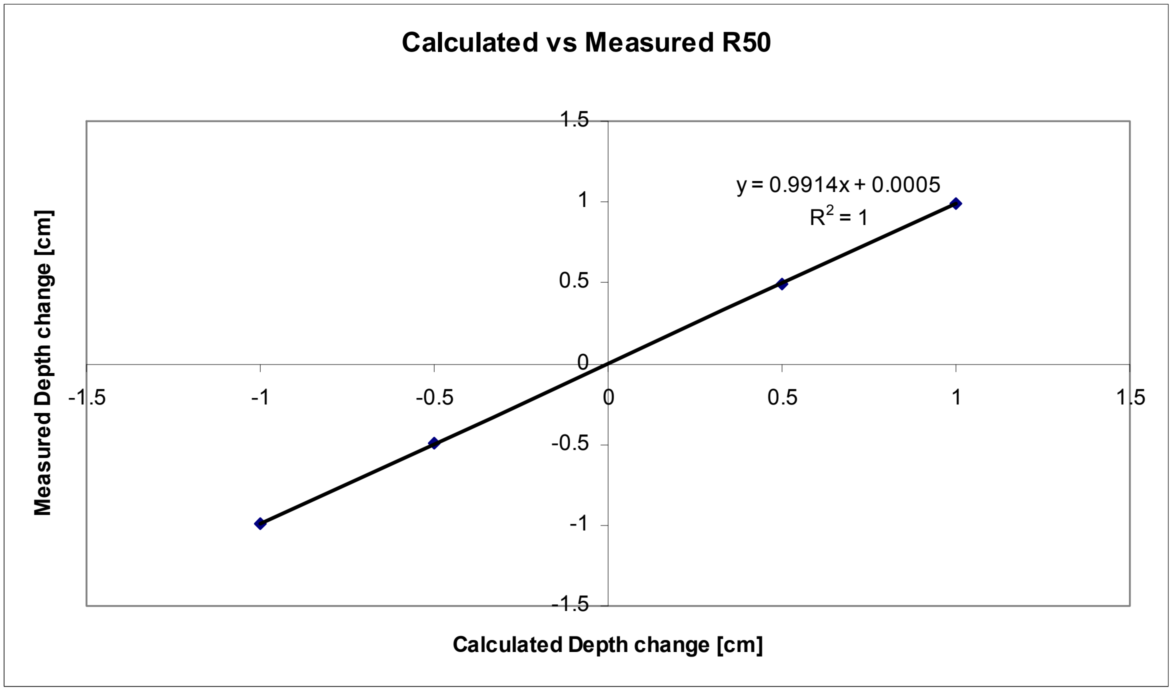

Figure 50: Correlation of calculated and measured depth dose

4.4 Discussion

4.4.1 Summary

Custom inverted Lucite wedges were designed to degrade the range of the proton beam to precisely match the distal edge of the target organs. The dimensions of these wedges balanced attenuation range with size, compatibility with proton gantry, proton range limit, wedge cart, and treatment couch.The total WET of the wedges was first determined. Then the distance was calculated to adjust the proton's range. This pre-determined shift was a surrogate for the detector signal and subsequent depth measurement from our detection device discussed in the previous chapter. One standard deviation of agreement was

0.04 millimeters. This figure is negligible compared to the in vivo and in vitro uncertainties of the detector.

4.4.2 Study limitations

One issue that was not addressed during the testing of our aim was the time effect between when the wedges receive a signal and the time that the range correction actually occurs. With the speed of the controller and motor along with the screw index, the maximum estimated wedge speed was 1 inch per second. Compared with the patient's anatomic variation from bladder and rectal filling, this speed was more than adequate. However, breathing induced range variation was not considered. This issue was a limitation of the entire localization technique since the distal falloff was only measured and corrected once per spill, or approximately every two seconds. Further investigation of the effects of patient breathing on variation of the anatomy in the lower abdomen was needed before translating this technique into the clinic.

There were two potential solutions to correct for breathing induced proton range variation. The first was to use an immobilization device that fits completely around the patient's anatomy. Another potential solution was the use of stereotactic monitoring and localization with a camera system in conjunction with our endorectal detector to estimate range variations between pulses. The ability of the wedges to adjust their position relative to a real-time breathing trace from the Varian RPM system (Varian Medical Systems, Palo Alto, CA) was tested. The lag between the position input and the time when the motor matched the position was slightly greater than 100 milliseconds. However, without corresponding data on the magnitude of breathing-induced depth changes and the correlation of those changes with the patient's skin surface, this potential method was speculation.

Another potential improvement of the system would be to add another dimension of proton beam correction. Additional fibers within the balloon could detect variation of the depth along the axis of the balloon. Based on difference in these measured values, a third wedge could be added to rotate the distal edge of the beam. The impact and feasibility of this technique could be simulated in the treatment planning system by measuring the rotation of the rectum and target organs in CT patient data and drawing custom regions of interest as a surrogate for the third wedge.

4.5 Specific Aim 2 conclusions

A dual wedge Lucite range degrader was designed with the initial goal of 2 millimeter precision, and we demonstrated that our design meets and exceeds our initial expectations. Considering the precision of both the detector and the wedges, the range shifting portion of the device should not significantly contribute to the treatment uncertainty and the residual distal margin needed to ensure treatment coverage with our localization technique.

Chapter 5: Dosimetric comparison of IMRT, bilateral proton, and single anterior proton beam treatment of the prostate

5.1 Introduction

Specific Aim 3: Determine dosimetric benefit of utilizing the *in vivo* proton beam detection device and external proton beam range shifter,

Working hypothesis: Using the measured precision of the *in vivo* proton beam detection device and external proton beam range shifter, the reduced margin planning treatment strategies reduce mean rectal dose by 20% over conventional bilateral proton and IMRT photon therapies.

The conversion of proton stopping power ratio from CT Hounsfield units to calculate proton range carries large uncertainties, necessitating large distal margins to ensure target coverage and diminishing the major benefit of proton therapy. In the case of proton radiotherapy for prostate cancer, the major dose-limiting organ is the rectum, which is adjacent to the prostate target. In current practice, institutions adopt bilateral treatment proton beams to avoid pointing the sharp falloff of the Bragg peak directly in front of the rectum. Unfortunately, this beam arrangement introduces higher rectal dose due to the large lateral penumbra of the proton beam. Several published studies compare bilateral proton treatment with photon IMRT of the prostate and reported significant sparing of the rectum and bladder volume at low doses (113-116). While low dose sparing of normal tissues is still beneficial to prostate cancer patients, these improvements may have minimal effect on acute rectal and bladder toxicity and may not allow target dose escalation or hypofractionation of treatment.

Methods to detect the anterior beam at depth were developed at this institution (this thesis) and elsewhere (99, 100) to eliminate the large distal proton planning margin, enabling abrupt dose falloff at the anterior rectal wall rather than the relatively shallow falloff of the lateral beam penumbra with conventional bi-lateral treatments.

The purpose of this chapter is to evaluate the ability of an anterior proton beam to adequately spare the rectum considering the measured precision of our *in vivo* patient set-up technique discussed thus far in the thesis. this treatment technique will be compared with the conventional treatment planning techniques: eight-field IMRT and bilateral proton treatment of the prostate. Based on the estimated rectal dose for patients receiving our technique for their proton radiotherapy, the thesis hypothesis will be evaluated.

5.2 Materials and methods

5.2.1 Patient protocol

The first twenty-seven prostate cancer patients treated with proton therapy at this institution enrolled in an IRB-approved prospective treatment planning study to compare standard IMRT and bi-lateral proton treatments with a single anterior proton beam treatment. An additional treatment plan was generated to simulate patient treatment with an anterior proton beam with a reduced distal margin. All twenty-seven patients had localized cancer of the prostate (T1-T3, N0, M0) prescribed to 75.6 CGE in 42 treatment fractions. Patients were immobilized with the Dual Leg Positioner (Cisco Systems, San Jose, CA) and marked with external skin fiducials for treatment alignment with the in-room lasers. All patients were instructed to maintain a full bladder and empty bowel. Endorectal balloons (MEDRAD, Inc., Pittsburgh, PA) were inserted into each patient's rectum to provide additional prostate immobilization, expand the rectal volume, and push the upper bowel out of the treatment field. A single CT data set was created for each patient, contoured by a single physician (AKL), and exported into treatment planning systems for plan generation. The rectum was contoured from the anus to the recto-sigmoid flexure. The rectal wall was generated by contracting the rectal contour by 3 mm and generating an ROI between the rectal contour and contracted contour. The bladder wall was generated identically to the rectal wall.

5.2.2 Treatment planning

For the patients' proton radiotherapy treatment, reference CT data sets were imported into Varian's Eclipse treatment planning system. Each daily fraction was delivered with equally weighted parallel-opposing passively scattered proton beams as illustrated in the middle of Figure 51. Bilateral proton beam treatment margins were generated with our standard institutional margin recipes. The lateral aperture margins for both the bilateral treatment plans and anterior proton beam treatment plans included allowances for set-up uncertainty (2mm), patient motion (3mm), and proton lateral beam penumbra (12 mm) for a total of 17 mm. The distal and proximal margins accounted for uncertainties in converted CT Hounsfield units to proton stopping power. For the bilateral plans, generation of these margins included 3.5% of the proton depth plus a 3 mm machine-dependent beam energy uncertainty for a total of 10-13 mm distally and 8-10 mm proximally. The distal margin for the anterior proton beam treatment was 2 mm to account for the estimated precision of the *in vivo* proton beam detection method we discussed in the previous two chapters. By measuring the beam at depth, we avoid the 3.5% of the depth distal margin because we have not calculated the beam pathlength from CT Hounsfield units. Since we detect the beam during each proton spill, we also avoid set-up and interfractional motion uncertainties. The proximal margins of the anterior proton beam plans were also set to 2 millimeters. The compensator smearing corrected for movement of tissue heterogeneities in the beam path by assuming the water equivalent depth to the distal edge of the target at any point is the maximum of its neighbors within the smearing radius. Determination of the smearing radius included the square root of the square of 3% of the target depth added with the square of set-up and motion uncertainties for a total of 8-10 mm. The smearing margin for the anterior beam plans was maintained at 7 mm.

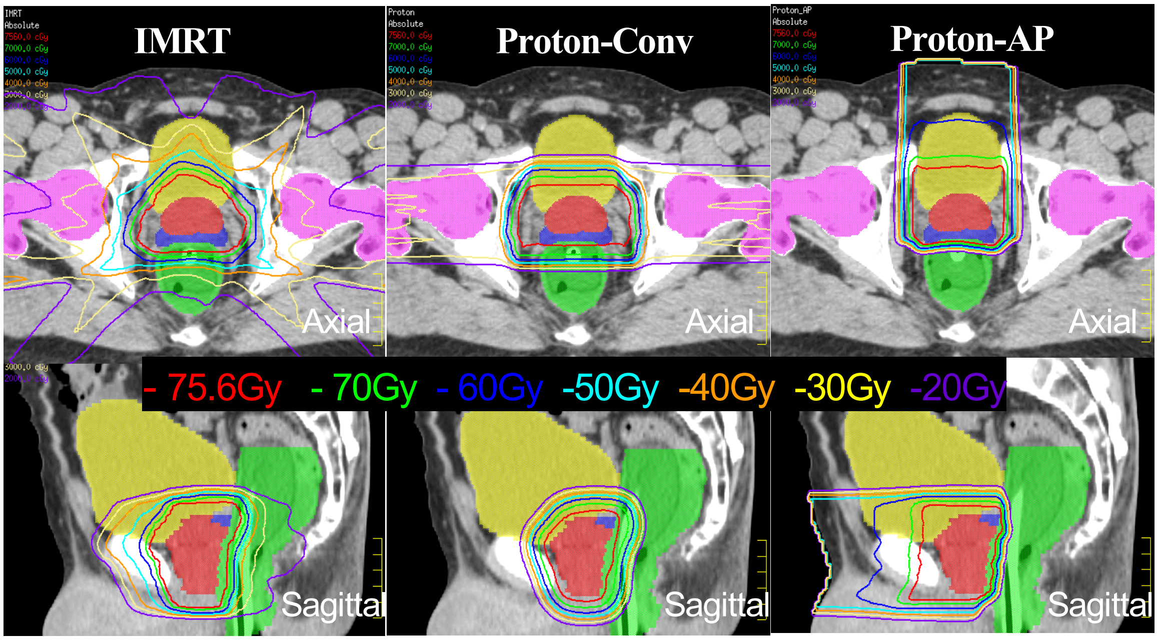

Figure 51: A dosimetric comparison between IMRT, bilateral proton therapy, and anterior beam proton therapy

CT data was imported into Phillip's Pinnacle treatment planning software for IMRT treatment planning generation. The IMRT PTV included an 8 mm isotropic expansion of the prostate except along the posterior border which was 5 mm (Figure 51: Left). The prescription dose was 75.6 CGE (shown in red). The IMRT treatment plans were optimized to spare normal tissue dose in the rectum and bladder at dose levels of 70, 60, and 40 Gy. Additional constraints were set to prevent hotspots in the femoral head and general normal tissue. The dose to the CTV was normalized to 100% coverage on the IMRT and bilateral treatment plans. In some case, complete coverage of the CTV was challenging with a 2 mm margin anterior plan due to the approximation of the compensator before accounting for scatter. In these cases, the compensator was manually modified and the treatment prescription set to a comparable level as the bilateral proton plans.

Additionally, we generated anterior proton plans with varying distal margins on a single patient to evaluate the effectiveness of treatment is our in vivo beam detection is more precise (down to 0 mm margin) or less precise (as much as 5 mm margin) than we originally anticipated. With the known relationship of distal margin to mean dose to the rectum, the treatment planning results (2 mm margin) can be extrapolated to the anterior treatment with a margin reflecting the measured precision of our device (2.4 mm).

5.2.3 Data analysis

Each patient's dose volume histograms for the prostate, proximal seminal vesicles, rectum, bladder, rectal wall, and bladder wall were collated in MATLAB and exported to Excel for data analysis. A single dose population histogram was generated for each organ in each treatment arm to illustrate the average relative volume exposed to a dose level. The terms Grey and cobalt-grey-equivalent were used interchangeably in this study. The relative biological value used for clinical proton treatment at our institution was 1.1. The dose levels were generated in 10 cGy bins for display in the dose population histograms. For each patient and organ, the maximum dose, mean dose, and median dose was recorded. For the prostate and proximal seminal vesicles, the minimum dose to 0.1 cc was recorded as well. The average, standard deviation, minimum, and maximum of each of those dose metrics was summarized in tabular form. To statistically compare our treatment arms for each organ, p-values were generated with the student t-test for each dose bin between each treatment arm for each critical organ. These results were displayed graphically relating the probability of any treatment arm pairing to be statistically the same at each dose bin. These graphs were called P-plots.

5.3 Results

5.3.1 Target organ coverage

Table 2 summarizes the dosimetric statistics for the prostate and the proximal seminal vesicles across our entire 27 patient group. Volume, mean dose, median dose, maximum dose, and minimum dose are displayed for each treatment arm and organ of interest. For each metric the statistical mean, standard deviation, minimum, and maximum describing the 27 patients were generated. Prostate coverage was comparable between the three treatment arms. Scatter from the pubic symphysis resulted in small hot spots in the middle of the prostate for some patients. A single statistical outlier had a maximum hotspot of 87.3 CGE which was reflected in the mean hot spot over the 27 patients (81.1 CGE for Anterior proton versus 80.3 CGE for IMRT and 79.3 CGE for bilateral proton treatments). The anterior proton plan appears more heterogeneous, however many clinicians feel that the relative hot and cold spots on proton plans in general average over a fractionated treatment due to the sensitivity of the dose distribution to registration errors of heterogeneities in the beam path. The invariance of the dose distribution assumed in photon treatment does not apply for proton treatments.

			Average	1SD	Max	Min
Prostate		Total Volume (cc)	66	18	108	38
	IMRT	Max Dose (0.1cc)	80.3	1.0	82.8	78.9
		Mean Dose	78.5	0.5	80.0	77.6
		Min Dose (0.1cc)	76.7	0.4	77.6	76.0
		Median Dose	78.5	0.5	80.0	77.6
	Bilateral	Max Dose (0.1cc)	79.3	0.5	80.6	78.1
		Mean Dose	77.9	0.3	78.7	77.2
		Min Dose (0.1cc)	76.5	0.3	77.2	76.1
		Median Dose	77.8	0.3	78.7	77.1
	AP	Max Dose (0.1cc)	80.9	1.1	83.3	79.4
		Mean Dose	77.9	0.4	78.7	76.6
		Min Dose (0.1cc)	75.4	0.5	76.4	74.1
		Median Dose	77.8	0.5	78.7	76.6
Proximal SV		Total Volume (cc)	8	3	15	2
	IMRT	Max Dose (0.1cc)	79.8	0.8	81.7	78.6
		Mean Dose	78.5	0.5	79.9	77.5
		Min Dose (0.1cc)	77.1	0.5	77.9	76.1
		Median Dose	78.4	0.5	79.9	77.5
	Bilateral	Max Dose (0.1cc)	78.5	0.5	79.7	77.6
		Mean Dose	77.6	0.5	78.7	77.0
		Min Dose (0.1cc)	76.8	0.5	78.0	76.1
		Median Dose	77.6	0.5	78.7	76.7
	AP	Max Dose (0.1cc)	79.7	0.9	81.5	77.9
		Mean Dose	77.9	0.6	79.5	76.8
		Min Dose (0.1cc)	76.0	1.4	78.2	70.6
		Median Dose	77.8	0.6	79.4	76.8

Table 2: Dose statistics of the prostate and proximal seminal vesicles

The dose population histograms of the prostate are shown in figure 52. The IMRT treatment plans appear to be slightly hotter than the bilateral proton treatment plans; however, these two treatment techniques were both normalized to receive full treatment coverage to the CTV. The dose population histogram for the AP proton beam appears troubling at first glance. The Eclipse treatment planning system had difficulty covering the CTV with a 2 millimeter distal margin treatment planning technique. This is because calculation of the range and subsequent range compensator generation is made without considering lateral scatter of the proton beam. After the full dose calculation is performed, the effective treatment margin at any one point along the distal edge of the treatment beam is slightly different from the margin set by the user. This is an inherent weakness of the treatment planning system rather than an indictment of the treatment planning strategy. Some compensation for this miscalculation was made by manual editing the range compensator and increasing the prescription isodose line.

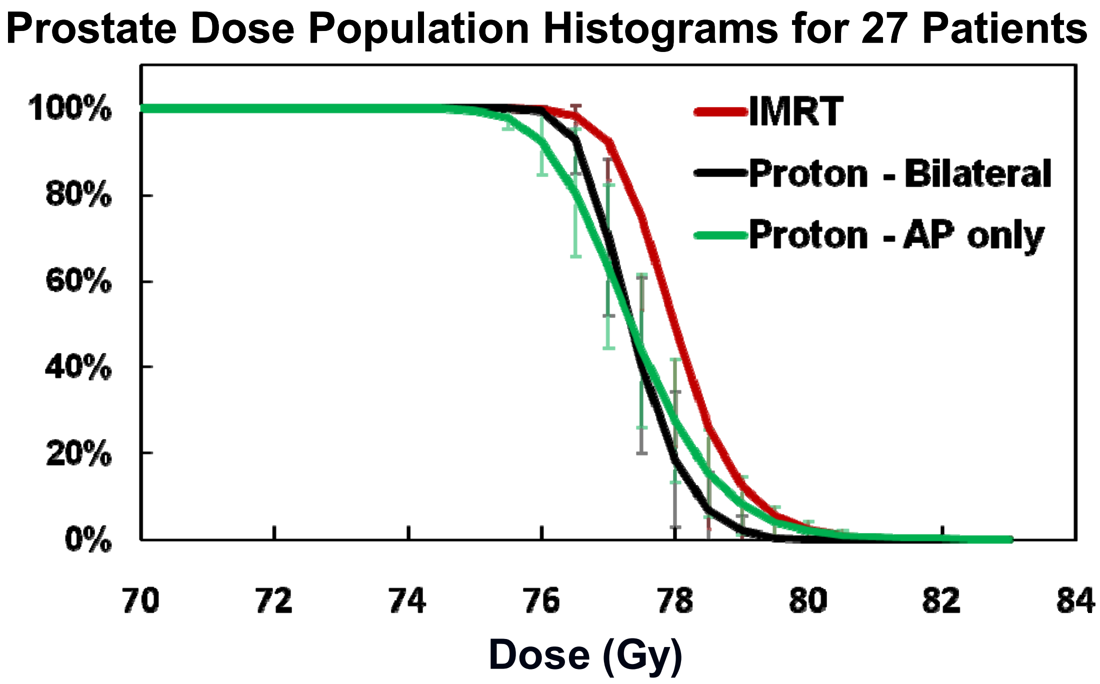

Figure 52: Dose population histogram of the prostate

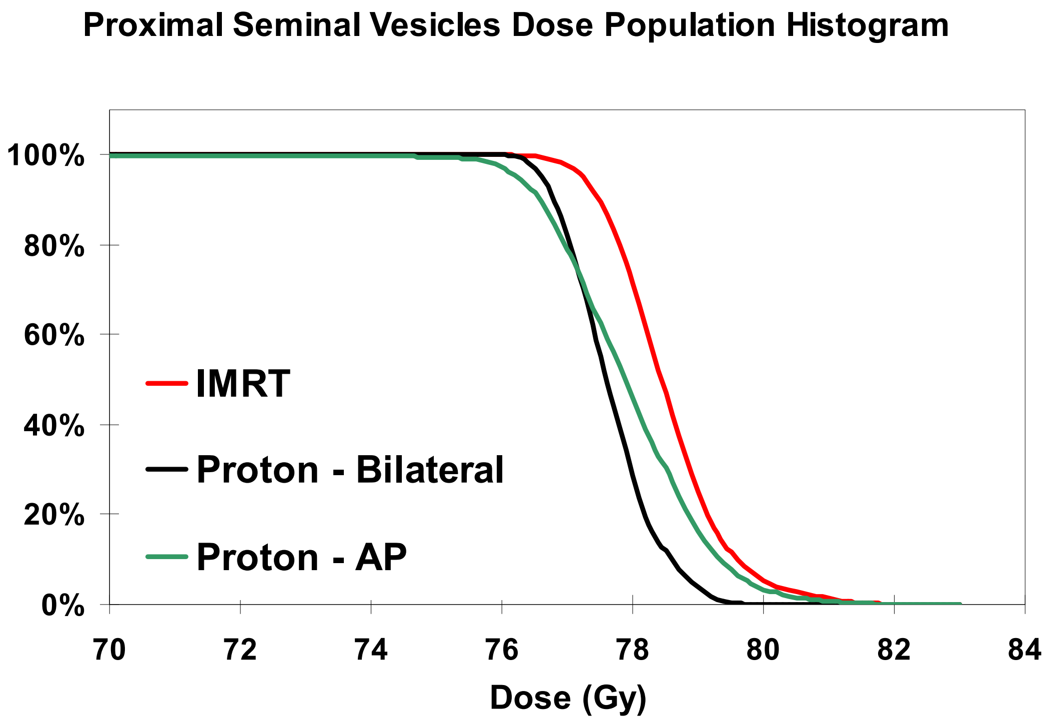

Proximal Seminal Vesicles Dose Population Histogram

Figure 53: Dose population histogram of the proximal seminal vesicles

Figure 53 illustrates the dose population histograms of the proximal seminal vesicles for our three treatment arms. The results are similar to those for the prostate. The mean patient minimum dose to the seminal vesicles was 76 CGE which is slightly better than the 75.4 CGE for the prostate. The dose to the proximal seminal vesicles with our anterior proton treatment plan was slightly more heterogeneous than the other two arms.

5.3.2 Rectum and rectal wall dose

			Average	1SD	Max	Min
Rectum		Total Volume (cc)	156	17	196	130
	IMRT	Max Dose (0.1cc)	80.1	0.9	82.0	78.3
		Mean Dose	31.5	4.2	38.8	22.3
		Median Dose	26.5	4.5	37.7	15.6
	Bilateral	Max Dose (0.1cc)	78.5	0.7	80.3	77.1
		Mean Dose	23.3	3.8	29.9	16.9
		Median Dose	7.9	5.1	19.4	0.6
	AP	Max Dose (0.1cc)	79.3	1.1	83.0	77.5
		Mean Dose	10.5	2.3	15.7	6.9
		Median Dose	0.0	0.0	0.1	0.0
Rectal Wall		Total Volume (cc)	31	4	38	26
	IMRT	Max Dose (0.1cc)	80.0	0.9	81.9	78.2
		Mean Dose	33.3	3.6	38.3	26.4
		Median Dose	23.4	3.6	31.7	15.1
	Bilateral	Max Dose (0.1cc)	78.5	0.7	80.2	77.1
		Mean Dose	24.6	2.9	29.7	19.8
		Median Dose	3.8	2.7	10.7	0.4
	AP	Max Dose (0.1cc)	79.1	1.2	84.1	77.3
		Mean Dose	16.2	2.3	21.7	12.3
		Median Dose	0.0	0.0	0.0	0.0

Table 3: Dose statistics of the rectum and rectal wall

Differences in dose to the rectum and the rectal wall were substantial between our treatment groups (Table 3). Mean dose to the rectum and rectal wall was greatest in the IMRT group (31.5 and 33.3 CGE) followed by the bilateral proton group (23.3 and 24.6 CGE) and anterior proton group (16.2 CGE). Maximum dose was similar between treatment groups. Over half the rectum was spared in our anterior treatment group (0 CGE) and nearly half in the bilateral group (median dose of 3.75 CGE).

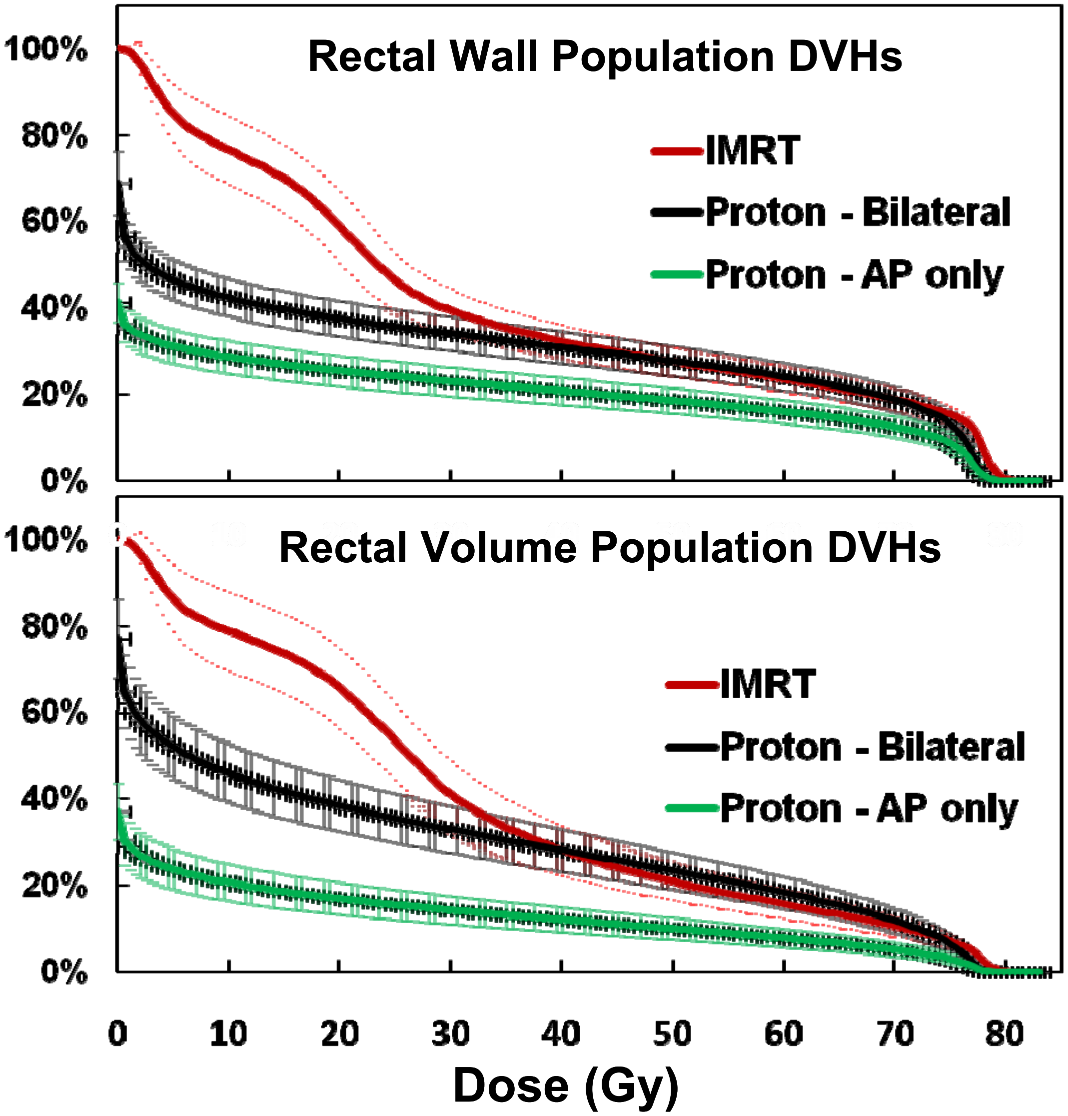

Figure 54: Dose population histograms of the rectal wall and rectum

Figure 54 illustrates the dose population histograms for the rectum (bottom) and rectal wall (top) for our three treatment techniques. The rectal sparing is nearly equivalent between bilateral and IMRT treatments except for low dose regions (sub-30 CGE) where protons substantially outperform IMRT for both the rectum and the rectal wall. The anterior treatment achieves nearly approximately 10-15% sparing of the rectal wall by volume of conventional bilateral proton treatment at all dose levels. The dose delivered to the entire rectum with the anterior proton beam treatment is much less than the bilateral and IMRT treatment techniques at all dose level less than 70 CGE. The dose to the rectum is comparable between the IMRT and bilateral proton arms for doses greater than 40 CGE. The dose to the rectum with the anterior beam planning is nearly half the dose from the other two treatment arms.

The p-plots provide a visual representation of the statistical significance between the treatment arms (Figure 55). The dose population histograms display error bars illustrating the standard deviation of the data sets at each dose bin. The standard deviation of the mean (SDM), which is used for determining the statistical significance, is the standard deviation divided by the square root of the number of patients. Therefore the SDM is greater than a factor of 5 times smaller than the standard deviation. In Figure 54, the SDM is extremely small. Therefore, small dosimetric changes between the treatment groups can change the statistical significance abruptly. The abrupt changes of the statistical significance are represented by the steep gradients of the p-plots. Figure 55 summarizes the statistical differences between our treatment arms for rectal sparing. The rectal dose for anterior treatment plan is significantly less then IMRT (red) for all dose level less then 80 CGE ($p< 0.01$) and less than bilateral proton for all dose levels less than 77.5 CGE ($p < 0.01$). The bilateral proton plan treats significantly less rectum then the IMRT plan for dose levels less than 35.5 CGE and significantly more rectum from 46.7 CGE to 71.4 CGE ($p<0.01$). The bilateral proton and IMRT plans are nearly equivalent at doses near prescription levels.

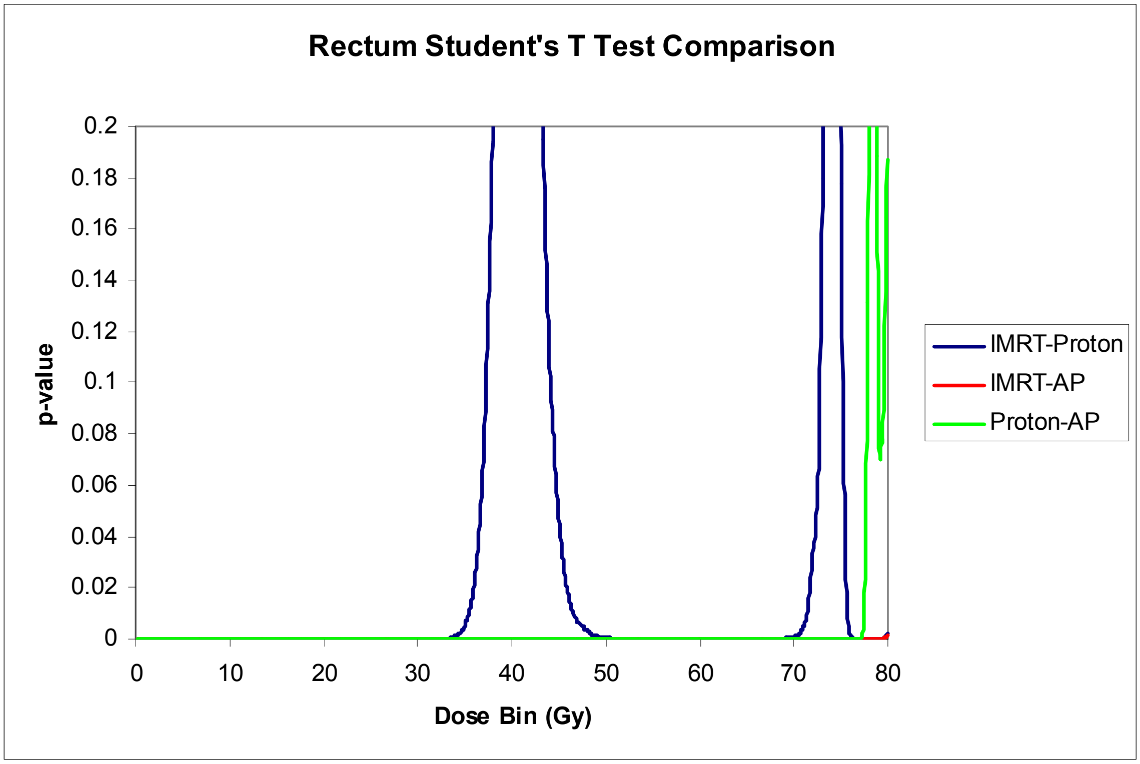

Figure 55: P-plot of the rectum

The statistical differences in the volume of rectal wall treated by our treatment arms are summarized in figure 56. As in the case of the rectal volume, the anterior treatment plan treated less rectal wall than the IMRT plan for all dose levels and less than the bilateral proton plan for all dose levels less then 77.4 CGE ($p < 0.01$). The bilateral proton plan treated less rectal wall than the IMRT for dose levels less than 41.4 CGE and greater than 73.3 CGE ($p < 0.01$).

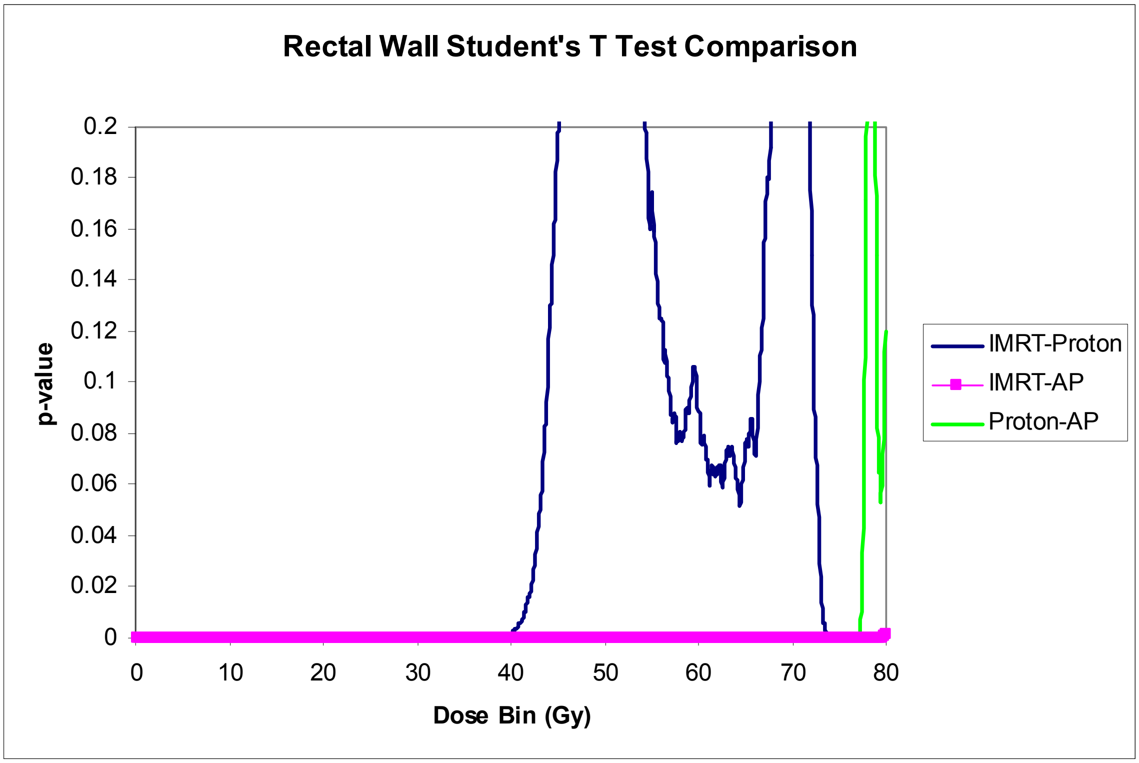

Figure 56: P-plot of the rectal wall for all three treatment techniques

5.3.3 Bladder and bladder wall dose

			Average	1SD	Max	Min
Bladder		Total Volume (cc)	335	141	620	133
	IMRT	Max Dose (0.1cc)	80.0	0.9	82.0	78.1
		Mean Dose	19.0	6.4	33.1	8.8
		Median Dose	8.0	6.7	24.6	1.9
	Bilateral	Max Dose (0.1cc)	78.7	0.6	79.9	77.6
		Mean Dose	14.7	5.7	31.2	7.5
		Median Dose	1.2	4.2	21.8	0.0
	AP	Max Dose (0.1cc)	80.1	1.2	82.9	77.2
		Mean Dose	22.1	9.4	43.4	8.8
		Median Dose	8.9	16.8	58.9	0.0
Bladder Wall		Total Volume (cc)	57	18	94	28
	IMRT	Max Dose (0.1cc)	79.8	0.9	81.9	78.1
		Mean Dose	19.8	6.0	33.4	10.2
		Median Dose	7.4	6.5	25.0	1.7
	Bilateral	Max Dose (0.1cc)	78.7	0.6	79.9	77.6
		Mean Dose	16.6	5.4	30.5	8.8
		Median Dose	0.8	3.0	15.6	0.0
	AP	Max Dose (0.1cc)	80.1	1.2	82.8	77.7
		Mean Dose	22.7	8.7	40.1	9.6
		Median Dose	7.8	15.1	50.6	0.0

Table 4: Dose Statistics of the Bladder

Dose to the bladder wall were nearly opposite of the rectal wall dose results (Table 4). The mean dose to the bladder and bladder wall was greatest in the anterior proton group (22.1 and 22.7 CGE) followed by IMRT group (19.0 and 19.8 CGE) and bilateral proton group (14.7 and 16.6 CGE). The maximum dose to the bladder and bladder wall were comparable between the IMRT and anterior proton beam plans and slightly reduced in the bilateral proton beam plans. The median dose to the bladder was greater in the anterior treatments than the other two treatment arms.

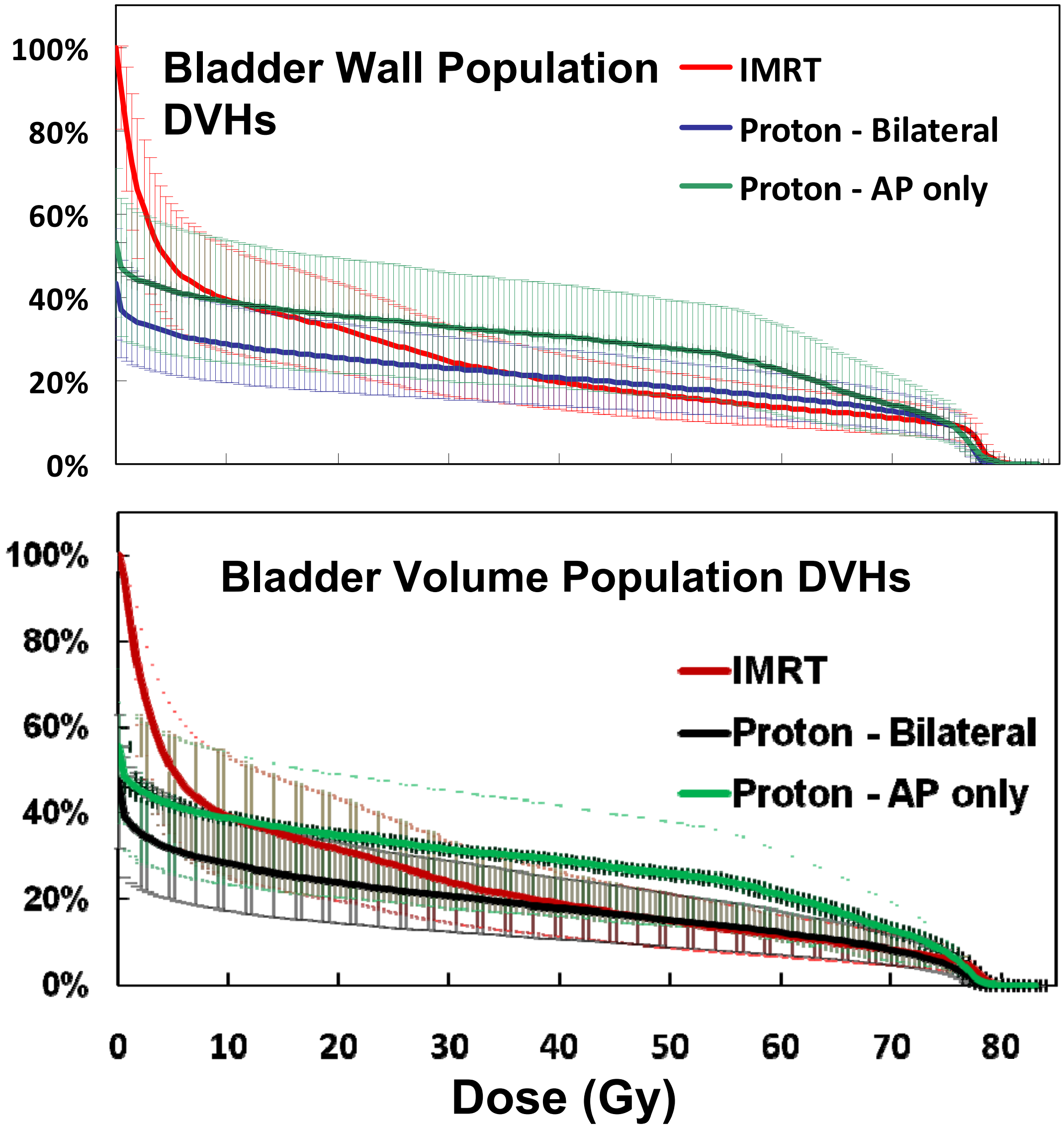

Figure 57: Dose population histograms of the bladder and the bladder wall.

Figure 57 shows the dosimetric comparison of the three treatment techniques for bladder and bladder sparing. The ability of the bilateral proton and IMRT plans to spare the bladder is comparable at dose levels greater than 30 CGE. The bilateral plan is slightly better for the low dose regions of the bladder and bladder wall. The anterior proton plan delivers approximately 10% more dose to the bladder wall than IMRT for dose levels greater than 30 Gy and at all dose levels when compared to bilateral proton treatment.

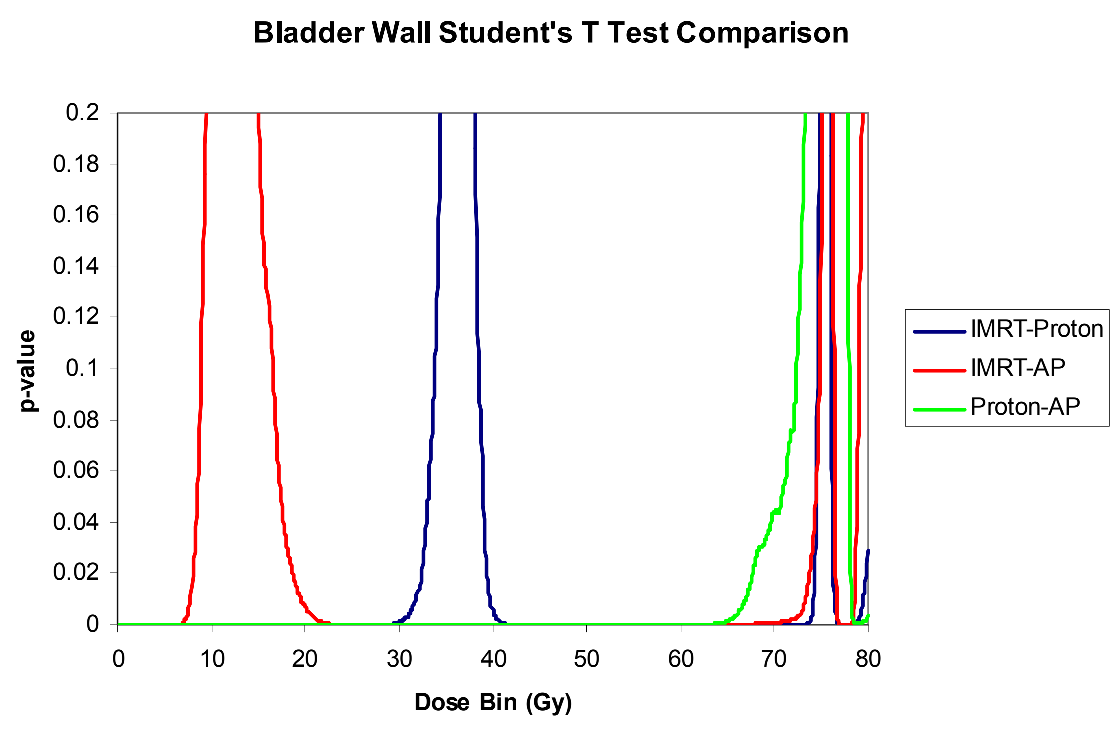

Figure 58: P-plot of the bladder wall dose

The statistical differences in the volume of bladder wall treated with our three treatment technique are summarized in figure 58. The IMRT plan delivered more dose to the bladder wall than the anterior proton technique for doses less than 7.8 CGE and less dose from 19.6 to 73.2 CGE ($p<0.01$). The IMRT plan delivered more dose to the bladder wall than the bilateral proton technique for doses less than 31.9 CGE and less dose from 39.8 to 74.1 CGE ($p<0.01$). The anterior proton technique treated more bladder wall than the bilateral technique for all dose levels less than 77.5 CGE ($p<0.01$).

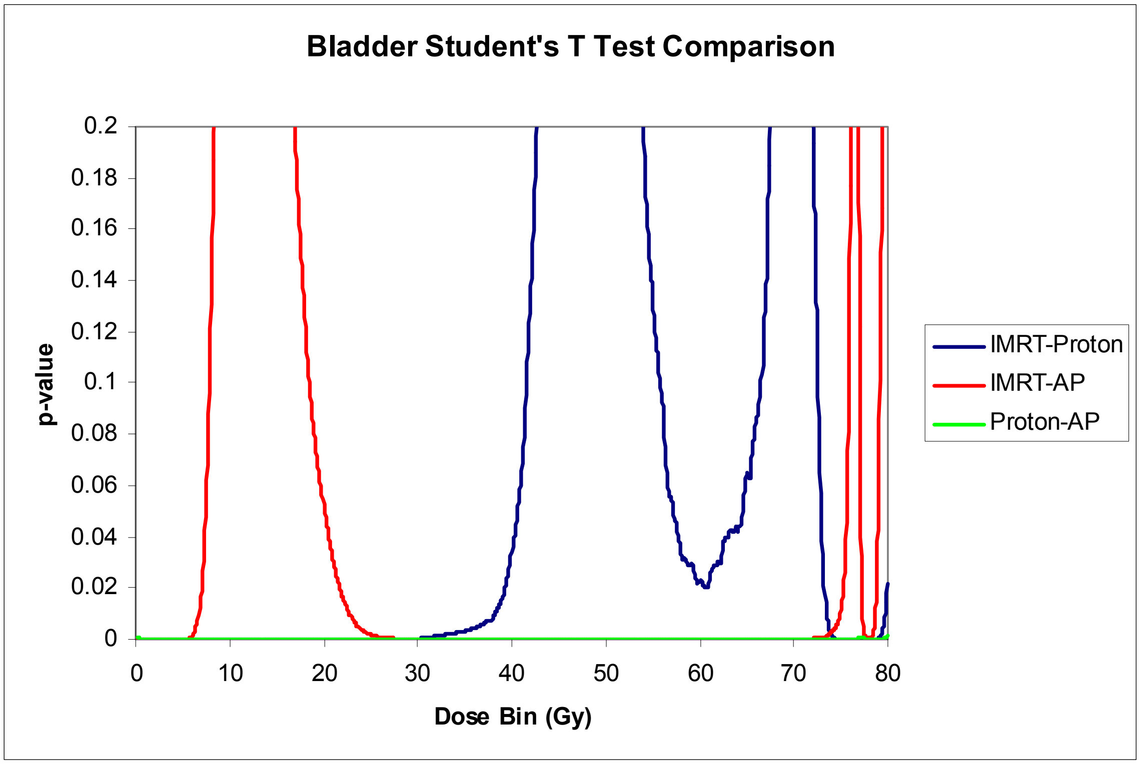

Figure 59: P-plot of the bladder

The statistical differences in the volume of bladder treated with our three treatment technique are summarized in figure 59. The IMRT plan delivered more dose to the bladder wall than the anterior proton technique for doses less than 6.7 CGE and less dose from 22.8 to 74.9 CGE (p<0.01). The IMRT plan delivered more dose to the bladder wall than the bilateral proton technique for doses less than 38.4 CGE and more volume at levels greater ant 73.5 CGE (p<0.01). The anterior proton technique treated more bladder wall than the bilateral technique for all dose levels (p<0.01).

4.3.4 Femoral head dose

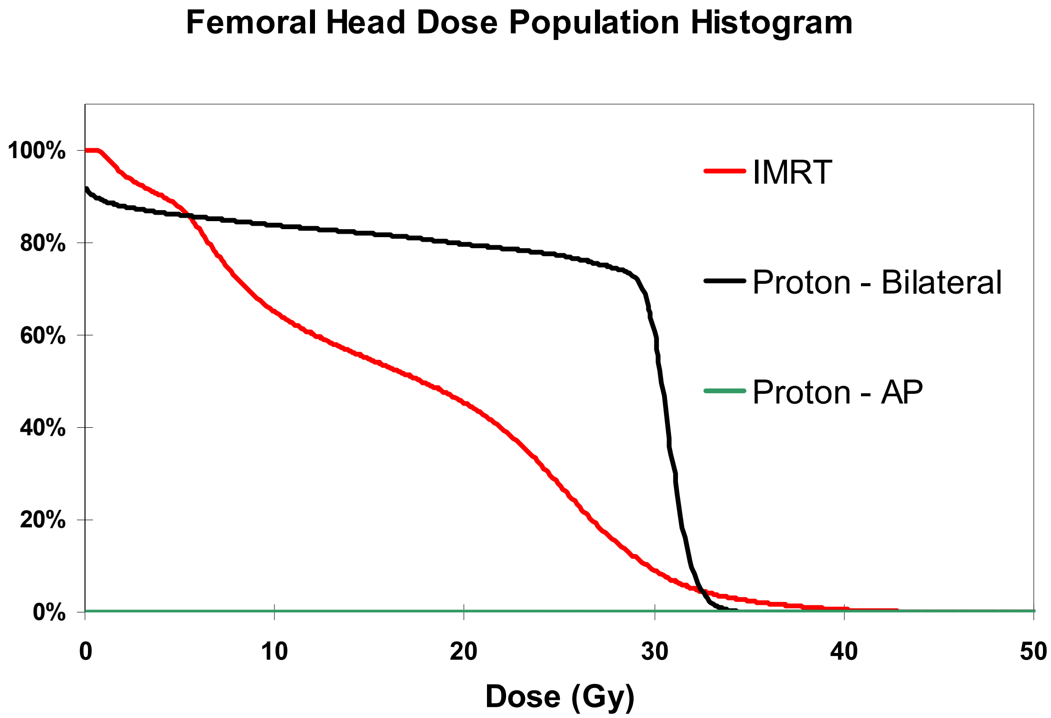

Figure 60: Dose population histogram of the femoral heads

Figure 60 illustrates that femoral head dose is considerably more for bilateral proton treatment than for standard 8-field IMRT. The mean dose to the femoral heads with the bilateral treatment techniques was 25.1 CGE and 17 CGE for the IMRT. However, the patient average maximum dose to 0.1 cc of the femoral heads was 34.5 CGE for the bilateral proton technique and 41.4 CGE for the IMRT treatments. Generally the femoral heads are constrained to a maximum dose of approximately 45 CGE, so IMRT treatment may be more likely to illicit morbidity than the bilateral treatment. Anterior beam treatment delivers nearly zero dose to the femoral heads.

5.3.5 Rectal dose and distal margin

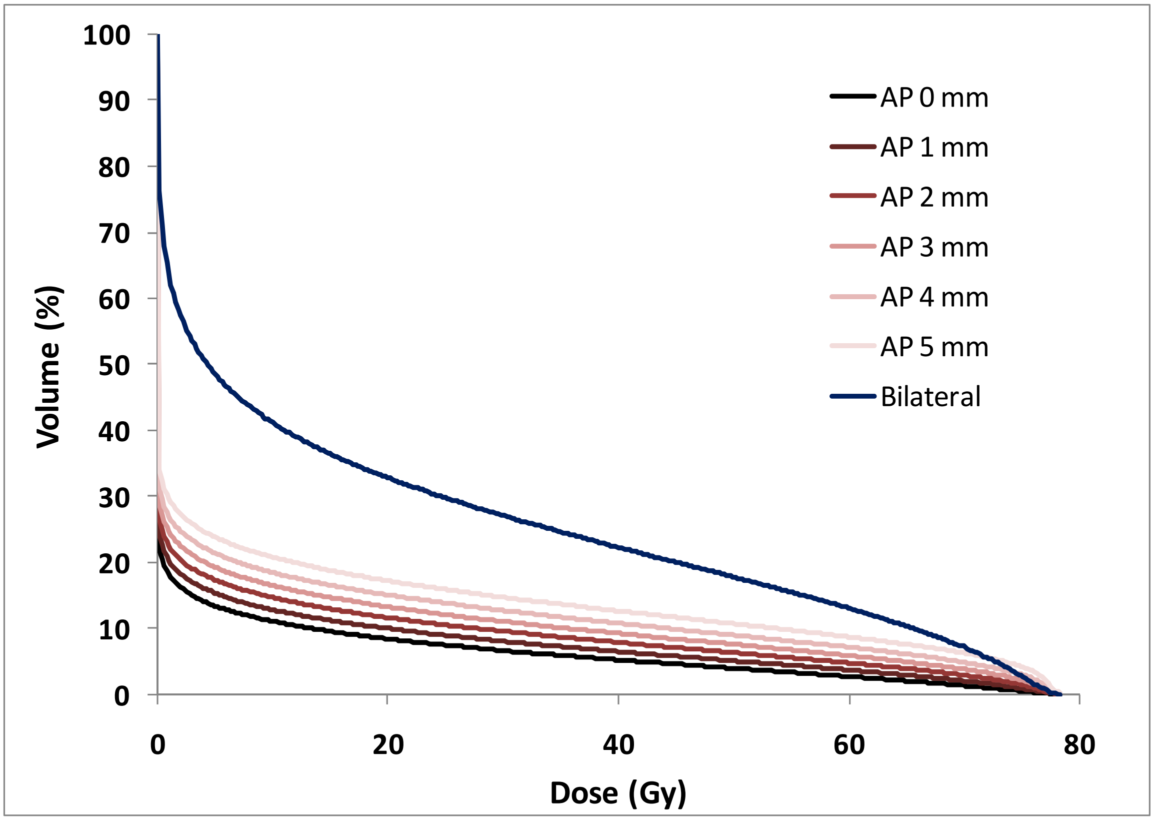

Figure 61: Rectal dose volume histogram as a function of distal margin

Figure 61 illustrates the dose volume histograms (DVH) of the prostate and rectal volume for a single patient calculated from a two field conventional bi-lateral proton beam plan and a single anterior proton beam plan with distal margins of 0 to 5 mm. The mean rectal dose is also displayed for each treatment planning strategy. The mean rectal dose scales linearly with increasing distal margin, approximately 100 cGy per millimeter. Although our predicted distal margin is 2.4 millimeters and our dosimetric study tested a 2 millimeter margins, we can realistically predict that the mean rectal dose over the 27 patients should be no more than 100 cGy higher with a 2.4 mm distal margin. Also, this figure suggests that the rectal sparing capability of the anterior beam treatment is preserved even with a 5 mm margin. Table 5 presents the data from Figure 61 in tabular form. The mean dose, V40, V60, and V70 are displayed for the bilateral proton and anterior proton plans. For comparison, the values for the anterior plans were normalized to those of the bilateral plans. The table indicates that the values of V60 and V70 are more sensitive to the size of the anterior treatment margin with comparing anterior treatment with bilateral treatment.

	Mean Dose		V40		V60		V70	
	[cGy]	% Bilateral	% Vol	% Bilateral	% Vol	% Bilateral	% Vol	% Bilateral
AP 0mm	481.5	0.25	5.26	0.24	2.75	0.21	1.39	0.19
AP1mm	581.1	0.30	6.54	0.29	3.76	0.29	2.11	0.29
AP2mm	690.1	0.36	7.97	0.36	4.83	0.37	3.01	0.41
AP3mm	798.5	0.42	9.36	0.42	5.98	0.46	3.93	0.54
AP4mm	921.1	0.48	10.91	0.49	7.30	0.56	4.99	0.68
AP5mm	1058.4	0.55	12.64	0.57	8.74	0.67	6.28	0.86
Bilateral	1912.4	1.00	22.33	1.00	13.10	1.00	7.29	1.00

Table 5: Table of rectal dose as a function of anterior proton beam margin size

5.4 Discussion

5.4.1 Summary

In this chapter, we set out to compare the dosimetric impact of IMRT and passively scattered bilateral proton beam treatment and investigate the utility of anterior beam proton treatment utilizing the proton's rapid distal fall-off for optimal rectal sparing. The previous two chapter outlined methods to detect the anterior beam at depth. These methods eliminated the distal proton planning margin, enabling abrupt dose falloff at the anterior rectal wall rather than the shallow falloff of the lateral beam penumbra with bi-lateral treatments.

The first 27 prostate cancer patients treated with protons at this institution enrolled in a prospective treatment planning study to compare the three treatment techniques. Based on the measured precision in the previous two chapters, we estimated that we needed a 2.4 millimeter treatment planning margin to ensure treatment coverage. We relaxed our 95% confidence criteria to 90% and applied a 2 mm distal margin for anterior proton beam planning based on our initial hypothesis. The anterior beam treatment significantly spared the rectum and anterior rectal wall more than the IMRT and bilateral beam treatments at all dose levels. However, bladder and bladder wall dose was greater in the anterior beam treatment than IMRT and bilateral beam treatments nearly all dose levels. No dose was delivered to the femoral heads with the anterior beam treatment while the IMRT and bilateral proton treatments delivered a mean dose of 17.0 CGE and 25.1 CGE to the femoral heads respectively.

5.4.2 Study limitations

Delivery of a highly conformal proton treatment plan with the Eclipse treatment planning system was challenging because of approximations made during the generation of the range compensator. Varian upgraded their software once during this experiment, and the resulting anterior proton plans were noticeably more homogeneous with the updated software. When the user set a particular margin for the target organs, the distance of the prescription isodose to the target organ should be close to this value at all points along the distal target. However, the residual distance between the target and prescription isodose did not always match the specified distal margin. Although the CTV was not always 100 % covered by the anterior plan, the normal tissue dose could potentially be lower with improved software. The TPS generated cold spots were compensated by increasing the dose delivered to the tumors, which in turn generated many hotspots. The compensator was manually edited in problematic areas, greatly increasing the range of the beam in nearby areas where additional margin was not necessarily needed.

5.4.3 Previous dosimetric comparisons

Several authors have investigated the potential of proton therapy relative to IMRT with dosimetric planning studies. Lomax (113) compared proton and photon intensity modulated radiotherapy in nine different patients with a variety of treatment legions including one patient with metastasizing prostate carcinoma treated with a single anterior spot-scanning proton beam. All plans included planning target margins as indicated in ICRU 50 and additional corrections were made for tissue inhomogeneities in the beam path. They reported greater treatment homogeneity in the target volume and nearly a three-fold reduction in the volume of normal tissue at 30% of the prescription for anterior proton treatment over 4-field conformal photon and 9-field IMRT. D_{mean} and $V_{50\%}$ were less for proton treatment over conformal photon and IMRT for all organs at risk; however maximum dose and $V_{70\%}$ were comparable between proton treatment and IMRT. Interestingly, rectum was not included as an organ-at-risk for this patient. Since this particular study treated to a relatively large fraction of the pelvis when compared with our treatment target, it was difficult to draw comparisons between the results.

Cella et al (117) compared 3D conformal photon, bilateral proton, 5 field IMRT, and 5 field IMPT treatments for a single patient. The PTV margin was a 1 cm expansion of the prostate and SV except at the rectal interface where the margin was 6 mm. Both proton arms exhibited increased homogeneity in the target and subsequently greater estimated TCP (95% versus 93%). Rectal sparing was increased at all dose levels below $V_{80\%}$ by the proton treatments. Authors estimated NTCP for late grade-three rectal toxicity with dose escalation to 99 Gy to be 4.7% for IMRT and 3.9% for IMPT. This study used geometric margins for their proton plans which resulted in a much more conformal treatment plan. Therefore the comparison with their intensity-modulated proton plan was not very useful. Their bilateral proton plan was comparable to our own since our lateral margins are set with a geometric expansion. After rescaling their dose volume histogram, the rectal dose on their patient was comparable to our dose population histogram. However, their IMRT results were extremely different. They excluded the anterior rectum from the PTV, resulting in nearly no volume of the rectum receiving dose in excess of 90% prescription. Their IMRT plan also appeared less conformal to the rectum at moderate dose levels (~ 50% prescription), and the bilateral consequently spares much more of the rectum than predicted in our study.

Mock et al (114) compared bilateral proton, 4-field conformal photon, and 7 field IMRT treatments for 5 prostate cancer patients simulating different disease stages by including no SV, proximal SV, or entire SV in the treatment volume. The PTV was generated with a uniform 5 mm expansion of the CTV. Inclusion or exclusion of the SV made little difference in the relative dosimetry between the treatment arms. Proton treatment substantially decreased integral dose at the cost of decreased dose homogeneity in the PTV. Proton treatment provide near equivalent femoral head sparing to IMRT, slightly increased bladder sparing, and substantially increased sparing to the rectal wall (~ absolute reduction of 20% at $V_{50\%}$ and 10% at $V_{90\%}$). This study's methods were closer to our own study. The 5 millimeter clinical target volume expansion they utilized was comparable to our lateral margin; however their IMRT plans spared the rectum considerably less than in our study. Their rectal DVH for the bilateral proton plans were very similar to our own.

Muzik et al (118) compared static and dynamic MLC linac-based IMRT, helical tomotherapy , and spot-scanning proton therapy (2 lateral-oblique beams) for a single deep seated prostate case. Again, their rectal dose for their proton treatment was similar, but their photon therapy rectal doses were considerably higher than our own.

Trofimov et al (115) compared IMRT, bilateral proton therapy, and IMPT for 10 prostate cancer patients. They included compensator smearing in addition to the traditional planning treatment margins for the target organs. Comparison of their IMRT and bilateral treatment arms was similar to our own results. They found little difference between the two treatment techniques for all doses in excess of 40 Gy. Their bladder dose results were also similar to our study. They found that the bladder dose in the bilateral proton arm was slightly higher on average from 40 Gy to prescription dose than in the IMRT arm and less at low doses.

Vargas et al (116) reported the rectal and bladder doses of the first 10 sequentially treated proton cancer patients at their institution. They set a 5mm axial PTV expansion and an 8 mm expansion cranial-caudally. They optimized the proton beam angles to maximally spare the rectum and bladder. They also reduced the lateral aperture margin from 1 cm to 7-8 mm posteriorely. The optimization in beam angle along with the reduction in the lateral aperture at the rectum led to significantly more rectal sparing than in our study.

5.4.4 Bladder and rectal toxicity

The use of the anterior proton therapy beam for prostate treatment has some potential limitations as well. The most obvious limitation is the increased bladder dose. A series of studies at our institution have modeled GU and GI toxicity as functions of bladder and rectal dose respectively (75, 78, 119). Results of these studies suggested that the strongest determinant of late bladder toxicity was the dose to the hottest 2.9% of the bladder. The determinants of late rectal bleeding were uncertain, however, the rectum did appear to exhibit a strong dose-volume effect. These two results in combination suggested a therapeutic gain by reducing the rectal dose-volume at the cost of some bladder dose. However, these studies enrolled 3D-CRT patients without the use of a rectal balloon and therefore may not adequately predict the occurrence and GU and GI toxicity in highly conformal therapy utilizing rectal balloons which can dramatically alter rectal dose(120-122). Oncologists will have to use their own discretion when choosing suitable treatment planning strategies until additional investigations addressing GU and GI toxicity in proton therapy prostate patients with rectal balloons are published.

5.4.5 RBE enhancement in the SOBP

Protons have comparable treatment effect as photons; however, a slight adjustment to the prescription is necessary to account for the slight difference in the relative biological effectiveness (RBE) of protons relative to equivalent photon dose. The dose delivered with proton treatment must be corrected with the experimentally determined RBE and which will convert dose delivered in Gray to cobalt grey equivalent (CGE) dose. The generally accepted value for the RBE of protons in the clinical therapeutic range is 1.1, however there is some uncertainty in this experimentally determined value, particularly at the distal edge of a proton SOBP (123). *In vivo* measurement estimates this enhancement at approximately 10%. *In vitro* studies have estimated distal RBE as great as 1.4.(124) RBE enhancement at the rectal wall could be problematic; however, there is a simultaneous dose fall-off in this region as the intensity of the proton beam drops off. Depending on the safety margin used in our *in vivo* feedback system, it is unclear which factor (RBE enhancement vs. rapid dose falloff) will be the dominant factor for the rectal wall. Nevertheless, this 1-2 cm dose enhancement region would benefit for prostate treatment. Biopsy studies have shown that tumor foci are preferentially located in the peripheral zone of the prostate. (125, 126) The potential biological dose enhancement would improve the therapeutic ratio for proton therapy with an anterior beam arrangement.

5.5 Specific Aim 3 conclusions

In this chapter, the dosimetric benefit of utilizing the *in vivo* proton beam detection device and external proton beam range shifter was determined considering our previous estimation of the technique precision. The estimated precision from the previous two chapters was 2.4 millimeters. We compared treatment with a 2 millimeter anterior proton beam with conventional IMRT and bilateral proton treatments for 90% treatment confidence. Bladder and rectal dose are similar between current IMRT and bilateral proton prostate treatments at dose levels above 30-40 CGE. With the implementation of *in vivo* proton beam detection, anterior proton beam treatment of prostate is a possible treatment alternative, substantial sparing dose to the rectum and femoral heads at the cost of increasing bladder dose. Given the relative amount of sparing of the rectum and increased bladder dose, we anticipate a therapeutic gain with our technique.

Chapter 6: Dissertation conclusion

At the beginning of this thesis, we hypothesized that the use of in vivo proton beam detection within a rectal balloon and dynamic range modulation of an anterior proton beam will enable the use of a reduced distal margin, reducing the mean rectal dose by 20% over conventional bilateral proton treatment and IMRT. To test this hypothesis a scintillation fluid filled endorectal balloon was designed for real-time determination of an anterior proton beam's range. The goal of 2 millimeter precision was nearly met. The estimated 95% confidence interval was 2.4 millimeters. A dual wedge Lucite range degrader was designed with an initial aim of 2 millimeter precision, and the design performance exceeded our expectations with an estimated 0.04 millimeter precision. The dosimetric benefit of utilizing the *in vivo* proton beam detection device and external proton beam range shifter was then determined by comparing treatment with a 2 millimeter anterior proton beam with conventional IMRT and bilateral proton treatments. The anterior beam treatment exceeded the expectations of our hypothesis, halving the dose the rectum receives during treatment. With the implementation of in vivo proton beam detection, anterior proton beam treatment of prostate is a feasible treatment option, substantial sparing dose to the rectum. Further work to translate this technology into clinical use should be promptly completed to reduce incidence of rectal morbidity in patients treated for prostate cancer with radiation therapy.

Bibliography

1. Jemal, A., R. Siegel, E. Ward, Y. Hao, J. Xu, and M. J. Thun. 2009. Cancer statistics, 2009. CA Cancer J Clin 59:225-249.
2. Mendenhall, W. M., R. H. Henderson, and N. P. Mendenhall. 2008. Definitive radiotherapy for prostate cancer. Am J Clin Oncol 31:496-503.
3. Zelefsky, M. J., and A. Harrison. 1997. Neoadjuvant androgen ablation prior to radiotherapy for prostate cancer: reducing the potential morbidity of therapy. Urology 49:38-45.
4. Pilepich, M. V., J. W. Buzydlowski, M. J. John, P. Rubin, D. G. McGowan, and V. A. Marcial. 1995. Phase II trial of hormonal cytoreduction with megestrol and diethylstilbestrol in conjunction with radiotherapy for carcinoma of the prostate: outcome results of RTOG 83-07. Int J Radiat Oncol Biol Phys 32:175-180.
5. Pilepich, M. V., K. Winter, M. J. John, J. B. Mesic, W. Sause, P. Rubin, C. Lawton, M. Machtay, and D. Grignon. 2001. Phase III radiation therapy oncology group (RTOG) trial 86-10 of androgen deprivation adjuvant to definitive radiotherapy in locally advanced carcinoma of the prostate. Int J Radiat Oncol Biol Phys 50:1243-1252.
6. Joon, D. L., M. Hasegawa, C. Sikes, V. S. Khoo, N. H. Terry, G. K. Zagars, M. L. Meistrich, and A. Pollack. 1997. Supraadditive apoptotic response of R3327-G rat prostate tumors to androgen ablation and radiation. Int J Radiat Oncol Biol Phys 38:1071-1077.

7. Blanco, A. I., and J. M. Michalski. 2003. Dose escalation in locally advanced carcinoma of the prostate. Semin Radiat Oncol 13:87-97.

8. Fiveash, J. B., G. Hanks, M. Roach, S. Wang, E. Vigneault, P. W. McLaughlin, and H. M. Sandler. 2000. 3D conformal radiation therapy (3DCRT) for high grade prostate cancer: a multi-institutional review. Int J Radiat Oncol Biol Phys 47:335-342.

9. Lyons, J. A., P. A. Kupelian, D. S. Mohan, C. A. Reddy, and E. A. Klein. 2000. Importance of high radiation doses (72 Gy or greater) in the treatment of stage T1-T3 adenocarcinoma of the prostate. Urology 55:85-90.

10. Hanks, G. E., T. E. Schultheiss, A. L. Hanlon, M. Hunt, W. R. Lee, B. E. Epstein, and L. R. Coia. 1997. Optimization of conformal radiation treatment of prostate cancer: report of a dose escalation study. Int J Radiat Oncol Biol Phys 37:543-550.

11. Zelefsky, M. J., S. A. Leibel, P. B. Gaudin, G. J. Kutcher, N. E. Fleshner, E. S. Venkatramen, V. E. Reuter, W. R. Fair, C. C. Ling, and Z. Fuks. 1998. Dose escalation with three-dimensional conformal radiation therapy affects the outcome in prostate cancer. Int J Radiat Oncol Biol Phys 41:491-500.

12. Pollack, A., G. K. Zagars, G. Starkschall, J. A. Antolak, J. J. Lee, E. Huang, A. C. von Eschenbach, D. A. Kuban, and I. Rosen. 2002. Prostate cancer radiation dose response: results of the M. D. Anderson phase III randomized trial. Int J Radiat Oncol Biol Phys 53:1097-1105.

13. Zietman, A. L., M. L. DeSilvio, J. D. Slater, C. J. Rossi, Jr., D. W. Miller, J. A. Adams, and W. U. Shipley. 2005. Comparison of conventional-dose vs high-dose conformal radiation therapy in clinically localized adenocarcinoma of the prostate: a randomized controlled trial. JAMA 294:1233-1239.

14. Fuks, Z., S. A. Leibel, K. E. Wallner, C. B. Begg, W. R. Fair, L. L. Anderson, B. S. Hilaris, and W. F. Whitmore. 1991. The effect of local control on metastatic dissemination in carcinoma of the prostate: long-term results in patients treated with 125I implantation. Int J Radiat Oncol Biol Phys 21:537-547.

15. Morgan, P. B., A. L. Hanlon, E. M. Horwitz, M. K. Buyyounouski, R. G. Uzzo, and A. Pollack. 2007. Radiation dose and late failures in prostate cancer. Int J Radiat Oncol Biol Phys 67:1074-1081.

16. Valicenti, R., J. Lu, M. Pilepich, S. Asbell, and D. Grignon. 2000. Survival advantage from higher-dose radiation therapy for clinically localized prostate cancer treated on the Radiation Therapy Oncology Group trials. J Clin Oncol 18:2740-2746.

17. Chism, D. B., E. M. Horwitz, A. L. Hanlon, W. H. Pinover, R. K. Mitra, and G. E. Hanks. 2003. Late morbidity profiles in prostate cancer patients treated to 79-84 Gy by a simple four-field coplanar beam arrangement. Int J Radiat Oncol Biol Phys 55:71-77.

18. Lawton, C. A., M. Won, M. V. Pilepich, S. O. Asbell, W. U. Shipley, G. E. Hanks, J. D. Cox, C. A. Perez, W. T. Sause, S. R. Doggett, and P. Rubin

1991. Long-term treatment sequelae following external beam irradiation for adenocarcinoma of the prostate: analysis of RTOG studies 7506 and 7706. Int J Radiat Oncol Biol Phys 21:935-939.

19. Smit, W. G., P. A. Helle, W. L. van Putten, A. J. Wijnmaalen, J. J. Seldenrath, and B. H. van der Werf-Messing. 1990. Late radiation damage in prostate cancer patients treated by high dose external radiotherapy in relation to rectal dose. Int J Radiat Oncol Biol Phys 18:23-29.
20. Dearnaley, D. P., M. R. Sydes, J. D. Graham, E. G. Aird, D. Bottomley, R. A. Cowan, R. A. Huddart, C. C. Jose, J. H. Matthews, J. Millar, A. R. Moore, R. C. Morgan, J. M. Russell, C. D. Scrase, R. J. Stephens, I. Syndikus, and M. K. Parmar. 2007. Escalated-dose versus standard-dose conformal radiotherapy in prostate cancer: first results from the MRC RT01 randomised controlled trial. Lancet Oncol 8:475-487.
21. Hanks, G. E., A. L. Hanlon, T. E. Schultheiss, W. H. Pinover, B. Movsas, B. E. Epstein, and M. A. Hunt. 1998. Dose escalation with 3D conformal treatment: five year outcomes, treatment optimization, and future directions. Int J Radiat Oncol Biol Phys 41:501-510.
22. Zelefsky, M. J., D. Cowen, Z. Fuks, M. Shike, C. Burman, A. Jackson, E. S. Venkatramen, and S. A. Leibel. 1999. Long term tolerance of high dose three-dimensional conformal radiotherapy in patients with localized prostate carcinoma. Cancer 85:2460-2468.
23. Ryu, J. K., K. Winter, J. M. Michalski, J. A. Purdy, A. M. Markoe, J. D. Earle, C. A. Perez, M. Roach, 3rd, H. M. Sandler, A. Pollack, and J. D.

Cox. 2002. Interim report of toxicity from 3D conformal radiation therapy (3D-CRT) for prostate cancer on 3DOG/RTOG 9406, level III (79.2 Gy). Int J Radiat Oncol Biol Phys 54:1036-1046.

24. 2001. Intensity-modulated radiotherapy: current status and issues of interest. Int J Radiat Oncol Biol Phys 51:880-914.

25. Ling, C. C., C. Burman, C. S. Chui, G. J. Kutcher, S. A. Leibel, T. LoSasso, R. Mohan, T. Bortfeld, L. Reinstein, S. Spirou, X. H. Wang, Q. Wu, M. Zelefsky, and Z. Fuks. 1996. Conformal radiation treatment of prostate cancer using inversely-planned intensity-modulated photon beams produced with dynamic multileaf collimation. Int J Radiat Oncol Biol Phys 35:721-730.

26. Zelefsky, M. J., Z. Fuks, L. Happersett, H. J. Lee, C. C. Ling, C. M. Burman, M. Hunt, T. Wolfe, E. S. Venkatraman, A. Jackson, M. Skwarchuk, and S. A. Leibel. 2000. Clinical experience with intensity modulated radiation therapy (IMRT) in prostate cancer. Radiother Oncol 55:241-249.

27. Zelefsky, M. J., Z. Fuks, M. Hunt, Y. Yamada, C. Marion, C. C. Ling, H. Amols, E. S. Venkatraman, and S. A. Leibel. 2002. High-dose intensity modulated radiation therapy for prostate cancer: early toxicity and biochemical outcome in 772 patients. Int J Radiat Oncol Biol Phys 53:1111-1116.

28. Li, J. G., and L. Xing. 2000. Inverse planning incorporating organ motion. Med Phys 27:1573-1578.

29. Samuelsson, A., C. Mercke, and K. A. Johansson. 2003. Systematic set-up errors for IMRT in the head and neck region: effect on dose distribution. Radiother Oncol 66:303-311.

30. Hector, C. L., S. Webb, and P. M. Evans. 2000. The dosimetric consequences of inter-fractional patient movement on conventional and intensity-modulated breast radiotherapy treatments. Radiother Oncol 54:57-64.

31. Kawashima, K. 1980. [Dose specification in external irradiation (I)--with special reference to ICRU report Nol 29: a physical aspect]. Rinsho Hoshasen 25:1253-1254.

32. 1999. ICRU Report 50. Prescribing, Recording, and Reporting Photon Beam Radiotherapy. International Commission on Radiation Units and Measurements, Bethesda, MD.

33. 1999. ICRU Report 62. Prescribing, Recording, and Reporting Photon Beam Radiotherapy (Supplement to ICRU Report 50. International Commission on Radiation Units and Measurements, Bethesda, MD.

34. Purdy, J. A. 2004. Current ICRU definitions of volumes: limitations and future directions. Semin Radiat Oncol 14:27-40.

35. van Herk, M. 2004. Errors and margins in radiotherapy. Semin Radiat Oncol 14:52-64.

36. Rasch, C., R. Steenbakkers, and M. van Herk. 2005. Target definition in prostate, head, and neck. Semin Radiat Oncol 15:136-145.

37. Song, P. Y., M. Washington, F. Vaida, R. Hamilton, D. Spelbring, B. Wyman, J. Harrison, and G. T. Chen. 1996. A comparison of four patient immobilization devices in the treatment of prostate cancer patients with three dimensional conformal radiotherapy. Int J Radiat Oncol Biol Phys 34:213-219.

38. Bentel, G. C., L. B. Marks, and R. Krishnamurthy. 1997. Impact of cradle immobilization on setup reproducibility during external beam radiation therapy for lung cancer. Int J Radiat Oncol Biol Phys 38:527-531.

39. Mitine, C., M. T. Hoornaert, A. Dutreix, and M. Beauduin. 1999. Radiotherapy of pelvic malignancies: impact of two types of rigid immobilisation devices on localisation errors. Radiother Oncol 52:19-27.

40. Malone, S., J. Szanto, G. Perry, L. Gerig, S. Manion, S. Dahrouge, and J. Crook. 2000. A prospective comparison of three systems of patient immobilization for prostate radiotherapy. Int J Radiat Oncol Biol Phys 48:657-665.

41. Pos, F. J., K. Koedooder, M. Hulshof, G. van Tienhoven, and D. G. Gonzalez. 2003. Influence of bladder and rectal volume on spatial variability of a bladder tumor during radical radiotherapy. Int J Radiat Oncol Biol Phys 55:835-841.

42. Nuyttens, J. J., J. M. Robertson, D. Yan, and A. Martinez. 2002. The variability of the clinical target volume for rectal cancer due to internal organ motion during adjuvant treatment. Int J Radiat Oncol Biol Phys 53:497-503.

43. Hoogeman, M. S., M. van Herk, D. Yan, L. J. Boersma, P. C. Koper, and J. V. Lebesque. 2002. A model to simulate day-to-day variations in rectum shape. Int J Radiat Oncol Biol Phys 54:615-625.

44. Langen, K. M., and D. T. Jones. 2001. Organ motion and its management. Int J Radiat Oncol Biol Phys 50:265-278.

45. Byrne, T. E. 2005. A review of prostate motion with considerations for the treatment of prostate cancer. Med Dosim 30:155-161.

46. Crook, J. M., Y. Raymond, D. Salhani, H. Yang, and B. Esche. 1995. Prostate motion during standard radiotherapy as assessed by fiducial markers. Radiother Oncol 37:35-42.

47. Kupelian, P. A., T. R. Willoughby, S. L. Meeks, A. Forbes, T. Wagner, M. Maach, and K. M. Langen. 2005. Intraprostatic fiducials for localization of the prostate gland: Monitoring intermarker distances during radiation therapy to test for marker stability. International Journal of Radiation Oncology Biology Physics 62:1291-1296.

48. Herman, M. G. 2005. Clinical use of electronic portal imaging. Semin Radiat Oncol 15:157-167.

49. Lattanzi, J., S. McNeeley, S. Donnelly, E. Palacio, A. Hanlon, T. E. Schultheiss, and G. E. Hanks. 2000. Ultrasound-based stereotactic guidance in prostate cancer--quantification of organ motion and set-up errors in external beam radiation therapy. Computer Aided Surgery. 5:289-295.

50. Serago, C. F., S. J. Chungbin, S. J. Buskirk, G. A. Ezzell, A. C. Collie, and S. A. Vora. 2002. Initial experience with ultrasound localization for positioning prostate cancer patients for external beam radiotherapy. Int J Radiat Oncol Biol Phys 53:1130-1138.

51. Chandra, A., L. Dong, E. Huang, D. A. Kuban, L. O'Neill, I. Rosen, and A. Pollack. 2003. Experience of ultrasound-based daily prostate localization. International Journal of Radiation Oncology, Biology, Physics. 56:436-447.

52. Langen, K. M., J. Pouliot, C. Anezinos, M. Aubin, A. R. Gottschalk, I. C. Hsu, D. Lowther, Y. M. Liu, K. Shinohara, L. J. Verhey, V. Weinberg, and M. Roach. 2003. Evaluation of ultrasound-based prostate localization for image-guided radiotherapy. Int. J. Radiat. Oncol. Biol. Phys 57:635-644.

53. Teh, B. S., W. Y. Mai, B. M. Uhl, M. E. Augspurger, W. H. Grant, 3rd, H. H. Lu, S. Y. Woo, L. S. Carpenter, J. K. Chiu, and E. B. Butler. 2001. Intensity-modulated radiation therapy (IMRT) for prostate cancer with the use of a rectal balloon for prostate immobilization: acute toxicity and dose-volume analysis. International Journal of Radiation Oncology, Biology, Physics 49:705-712.

54. Ciernik, I. F., B. G. Baumert, P. Egli, C. Glanzmann, and U. M. Lutolf. 2002. On-line correction of beam portals in the treatment of prostate cancer using an endorectal balloon device. Radiotherapy & Oncology. 65:39-45.

55. McGary, J. E., B. S. Teh, E. B. Butler, and W. Grant, 3rd. 2002. Prostate immobilization using a rectal balloon. Journal of Applied Clinical Medical Physics. 3:6-11.

56. Teh, B. S., J. E. McGary, L. Dong, W. Y. Mai, L. S. Carpenter, H. H. Lu, J. K. Chiu, S. Y. Woo, W. H. Grant, and E. B. Butler. 2002. The use of rectal balloon during the delivery of intensity modulated radiotherapy (IMRT) for prostate cancer: more than just a prostate gland immobilization device? Cancer Journal. 8:476-483.

57. Wachter, S., N. Gerstner, D. Dorner, G. Goldner, A. Colotto, A. Wambersie, and R. Potter. 2002. The influence of a rectal balloon tube as internal immobilization device on variations of volumes and dose-volume histograms during treatment course of conformal radiotherapy for prostate cancer. International Journal of Radiation Oncology, Biology, Physics. 52:91-100.

58. Jaffray, D. A. 2005. Emergent technologies for 3-dimensional image-guided radiation delivery. Semin Radiat Oncol 15:208-216.

59. Court, L., I. Rosen, R. Mohan, and L. Dong. 2003. Evaluation of mechanical precision and alignment uncertainties for an integrated CT/LINAC system. Med Phys 30:1198-1210.

60. de Crevoisier, R., A. D. Melancon, D. A. Kuban, A. K. Lee, R. M. Cheung, S. L. Tucker, R. J. Kudchadker, W. D. Newhauser, L. Zhang, R. Mohan, and L. Dong. 2007. Changes in the pelvic anatomy after an IMRT

treatment fraction of prostate cancer. Int J Radiat Oncol Biol Phys 68:1529-1536.

61. Melancon, A. D., J. C. O'Daniel, L. Zhang, R. J. Kudchadker, D. A. Kuban, A. K. Lee, R. M. Cheung, R. de Crevoisier, S. L. Tucker, W. D. Newhauser, R. Mohan, and L. Dong. 2007. Is a 3-mm intrafractional margin sufficient for daily image-guided intensity-modulated radiation therapy of prostate cancer? Radiother Oncol 85:251-259.

62. Wilson, R. R. 1946. Radiological use of fast protons. Radiology 47:487-491.

63. Smith, A. R. 2006. Proton therapy. Phys Med Biol 51:R491-504.

64. Koehler, A. M., R. J. Schneider, and J. M. Sisterson. 1977. Flattening of proton dose distributions for large-field radiotherapy. Med Phys 4:297-301.

65. Chu, W. T., B. A. Ludewigt, and T. R. Renner. 1993. Instrumentation for treatment of cancer using proton and light-ion beams. Review of Scientific Instruments 64:2055.

66. Urie, M., M. Goitein, W. R. Holley, and G. T. Chen. 1986. Degradation of the Bragg peak due to inhomogeneities. Physics in medicine and biology 31:1-15.

67. Schaffner, B., E. Pedroni, and A. Lomax. 1999. Dose calculation models for proton treatment planning using a dynamic beam delivery system: an attempt to include density heterogeneity effects in the analytical dose calculation. Physics in medicine and biology 44:27-41.

68. Urie, M., M. Goitein, and M. Wagner. 1984. Compensating for heterogeneities in proton radiation therapy. Phys Med Biol 29:553-566.

69. Moyers, M. F., D. W. Miller, D. A. Bush, and J. D. Slater. 2001. Methodologies and tools for proton beam design for lung tumors. Int J Radiat Oncol Biol Phys 49:1429-1438.

70. Constantinou, C., J. C. Harrington, and L. A. DeWerd. 1992. An electron density calibration phantom for CT-based treatment planning computers. Med Phys 19:325-327.

71. Schneider, U., E. Pedroni, and A. Lomax. 1996. The calibration of CT Hounsfield units for radiotherapy treatment planning. Phys Med Biol 41:111-124.

72. Rossi, C. J. 1999. Conformal proton beam therapy of prostate cancer-update on the Loma Linda University medical center experience. Strahlenther Onkol Suppl 2:82-84.

73. Slater, J. D., C. J. Rossi, Jr., L. T. Yonemoto, D. A. Bush, B. R. Jabola, R. P. Levy, R. I. Grove, W. Preston, and J. M. Slater. 2004. Proton therapy for prostate cancer: the initial Loma Linda University experience. Int J Radiat Oncol Biol Phys 59:348-352.

74. Nutting, C., D. P. Dearnaley, and S. Webb. 2000. Intensity modulated radiation therapy: a clinical review. Br J Radiol 73:459-469.

75. Cheung, M. R., S. L. Tucker, L. Dong, R. de Crevoisier, A. K. Lee, S. Frank, R. J. Kudchadker, H. Thames, R. Mohan, and D. Kuban. 2007. Investigation of bladder dose and volume factors influencing late urinary

toxicity after external beam radiotherapy for prostate cancer. Int J Radiat Oncol Biol Phys 67:1059-1065.

76. Fiorino, C., C. Cozzarini, V. Vavassori, G. Sanguineti, C. Bianchi, G. M. Cattaneo, F. Foppiano, A. Magli, and A. Piazzolla. 2002. Relationships between DVHs and late rectal bleeding after radiotherapy for prostate cancer: analysis of a large group of patients pooled from three institutions. Radiother Oncol 64:1-12.

77. Huang, E. H., A. Pollack, L. Levy, G. Starkschall, L. Dong, I. Rosen, and D. A. Kuban. 2002. Late rectal toxicity: dose-volume effects of conformal radiotherapy for prostate cancer. Int J Radiat Oncol Biol Phys 54:1314-1321.

78. Tucker, S. L., R. Cheung, L. Dong, H. H. Liu, H. D. Thames, E. H. Huang, D. Kuban, and R. Mohan. 2004. Dose-volume response analyses of late rectal bleeding after radiotherapy for prostate cancer. Int J Radiat Oncol Biol Phys 59:353-365.

79. Birks, J. B. 1964. The theory and practice of scintillation counting. Pergamon Press; [distributed in the Western Hemisphere by Macmillan, Oxford, New York,.

80. Knoll, G. F. 2000. Radiation detection and measurement. Wiley, New York.

81. Lambert, J., T. Nakano, S. Law, J. Elsey, D. R. McKenzie, and N. Suchowerska. 2007. In vivo dosimeters for HDR brachytherapy: a comparison of a diamond detector, MOSFET, TLD, and scintillation detector. Med Phys 34:1759-1765.

82. Archambault, L., J. Arsenault, L. Gingras, A. S. Beddar, R. Roy, and L. Beaulieu. 2005. Plastic scintillation dosimetry: optimal selection of scintillating fibers and scintillators. Med Phys 32:2271-2278.

83. Archambault, L., A. S. Beddar, L. Gingras, R. Roy, and L. Beaulieu. 2006. Measurement accuracy and cerenkov removal for high performance, high spatial resolution scintillation dosimetry. Med Phys 33:128-135.

84. Beddar, A. S., S. Law, N. Suchowerska, and T. R. Mackie. 2003. Plastic scintillation dosimetry: optimization of light collection efficiency. Phys Med Biol 48:1141-1152.

85. Beddar, A. S., N. Suchowerska, and S. H. Law. 2004. Plastic scintillation dosimetry for radiation therapy: minimizing capture of Cerenkov radiation noise. Phys Med Biol 49:783-790.

86. Beddar, A. S., M. Salehpour, T. M. Briere, H. Hamidian, and M. T. Gillin. 2005. Preliminary evaluation of implantable MOSFET radiation dosimeters. Phys Med Biol 50:141-149.

87. Briere, T. M., A. S. Beddar, and M. T. Gillin. 2005. Evaluation of precalibrated implantable MOSFET radiation dosimeters for megavoltage photon beams. Med Phys 32:3346-3349.

88. Briere, T. M., J. Lii, K. Prado, M. T. Gillin, and A. Sam Beddar. 2006. Single-use MOSFET radiation dosimeters for the quality assurance of megavoltage photon beams. Phys Med Biol 51:1139-1144.

89. Lee, A. K., R. Kudchadker, B. Choi, S. Choi, J. Bluett, R. Zhu, and L. Dong. 2008. The Effectiveness of Rectal Balloon and Orthogonal Imaging for

Proton Therapy of Prostate Cancer. Int J Radiat Oncol Biol Phys 72:S553-S554.

90. Kapany, N. S. 1967. Fiber optics; principles and applications. Academic Press, New York,.

91. Court, L. E., and L. Dong. 2003. Automatic registration of the prostate for computed-tomography-guided radiotherapy. Med Phys 30:2750-2757.

92. Birks, J. B. 1953. Scintillation counters. McGraw-Hill, New York,.

93. Michaelian, K., and A. Menchaca-Rocha. 1994. Model of ion-induced luminescence based on energy deposition by secondary electrons. Phys Rev B Condens Matter 49:15550-15562.

94. Kirov, A. S., S. Shrinivas, C. Hurlbut, J. F. Dempsey, W. R. Binns, and J. L. Poblete. 2000. New water equivalent liquid scintillation solutions for 3D dosimetry. Med Phys 27:1156-1164.

95. Ponisch, F., L. Archambault, T. M. Briere, N. Sahoo, R. Mohan, S. Beddar, and M. T. Gillin. 2009. Liquid scintillator for 2D dosimetry for high-energy photon beams. Med Phys 36:1478-1485.

96. Archambault, L., J. C. Polf, L. Beaulieu, and S. Beddar. 2008. Characterizing the response of miniature scintillation detectors when irradiated with proton beams. Phys Med Biol 53:1865-1876.

97. Beddar, S., L. Archambault, N. Sahoo, F. Poenisch, G. T. Chen, M. T. Gillin, and R. Mohan. 2009. Exploration of the potential of liquid scintillators for real-time 3D dosimetry of intensity modulated proton beams. Med Phys 36:1736-1743.

98. Ayotte, G., L. Archambault, L. Gingras, F. Lacroix, A. S. Beddar, and L. Beaulieu. 2006. Surface preparation and coupling in plastic scintillator dosimetry. Med Phys 33:3519-3525.

99. Lu, H. M. 2008. A point dose method for in vivo range verification in proton therapy. Physics in medicine and biology 53:N415-422.

100. Lu, H. M. 2008. A potential method for in vivo range verification in proton therapy treatment. Phys Med Biol 53:1413-1424.

101. Enghardt, W., J. Debus, T. Haberer, B. G. Hasch, R. Hinz, O. Jakel, M. Kramer, K. Lauckner, and J. Pawelke. 1999. The application of PET to quality assurance of heavy-ion tumor therapy. Strahlenther Onkol 175 Suppl 2:33-36.

102. Knopf, A., K. Parodi, H. Paganetti, E. Cascio, A. Bonab, and T. Bortfeld. 2008. Quantitative assessment of the physical potential of proton beam range verification with PET/CT. Phys Med Biol 53:4137-4151.

103. Parodi, K., and W. Enghardt. 2000. Potential application of PET in quality assurance of proton therapy. Phys Med Biol 45:N151-156.

104. Parodi, K., N. Saito, N. Chaudhri, C. Richter, M. Durante, W. Enghardt, E. Rietzel, and C. Bert. 2009. 4D in-beam positron emission tomography for verification of motion-compensated ion beam therapy. Med Phys 36:4230-4243.

105. Raju, M. R. 1980. Heavy particle radiotherapy. Academic Press, New York.

106. Leo, W. R. 1994. Techniques for nuclear and particle physics experiments : a how-to approach. Springer, Berlin ; New York.

107. Arjomandy, B., N. Sahoo, X. R. Zhu, J. R. Zullo, R. Y. Wu, M. Zhu, X. Ding, C. Martin, G. Ciangaru, and M. T. Gillin. 2009. An overview of the comprehensive proton therapy machine quality assurance procedures implemented at The University of Texas M. D. Anderson Cancer Center Proton Therapy Center-Houston. Med Phys 36:2269-2282.

108. Pedroni, E., R. Bacher, H. Blattmann, T. Bohringer, A. Coray, A. Lomax, S. Lin, G. Munkel, S. Scheib, U. Schneider, and et al. 1995. The 200-MeV proton therapy project at the Paul Scherrer Institute: conceptual design and practical realization. Med Phys 22:37-53.

109. Paganetti, H. 1998. Calculation of the spatial variation of relative biological effectiveness in a therapeutic proton field for eye treatment. Phys Med Biol 43:2147-2157.

110. Paganetti, H. 1998. Monte Carlo method to study the proton fluence for treatment planning. Med Phys 25:2370-2375.

111. Newhauser, W., N. Koch, S. Hummel, M. Ziegler, and U. Titt. 2005. Monte Carlo simulations of a nozzle for the treatment of ocular tumours with high-energy proton beams. Phys Med Biol 50:5229-5249.

112. Newhauser, W. D., J. Burns, and A. R. Smith. 2002. Dosimetry for ocular proton beam therapy at the Harvard Cyclotron Laboratory based on the ICRU Report 59. Med Phys 29:1953-1961.

113. Lomax, A. J., T. Bortfeld, G. Goitein, J. Debus, C. Dykstra, P. A. Tercier, P. A. Coucke, and R. O. Mirimanoff. 1999. A treatment planning inter-

comparison of proton and intensity modulated photon radiotherapy. Radiother Oncol 51:257-271.

114. Mock, U., J. Bogner, D. Georg, T. Auberger, and R. Potter. 2005. Comparative treatment planning on localized prostate carcinoma conformal photon- versus proton-based radiotherapy. Strahlenther Onkol 181:448-455.

115. Trofimov, A., P. L. Nguyen, J. J. Coen, K. P. Doppke, R. J. Schneider, J. A. Adams, T. R. Bortfeld, A. L. Zietman, T. F. Delaney, and W. U. Shipley. 2007. Radiotherapy treatment of early-stage prostate cancer with IMRT and protons: a treatment planning comparison. International journal of radiation oncology, biology, physics 69:444-453.

116. Vargas, C., A. Fryer, C. Mahajan, D. Indelicato, D. Horne, A. Chellini, C. McKenzie, P. Lawlor, R. Henderson, Z. Li, L. Lin, K. Olivier, and S. Keole. 2008. Dose-volume comparison of proton therapy and intensity-modulated radiotherapy for prostate cancer. International journal of radiation oncology, biology, physics 70:744-751.

117. Cella, L., A. Lomax, and R. Miralbell. 2001. Potential role of intensity modulated proton beams in prostate cancer radiotherapy. Int J Radiat Oncol Biol Phys 49:217-223.

118. Muzik, J., M. Soukup, and M. Alber. 2008. Comparison of fixed-beam IMRT, helical tomotherapy, and IMPT for selected cases. Med Phys 35:1580-1592.

119. Tucker, S. L., L. Dong, R. Cheung, J. Johnson, R. Mohan, E. H. Huang, H. H. Liu, H. D. Thames, and D. Kuban. 2004. Comparison of rectal dose-wall histogram versus dose-volume histogram for modeling the incidence of late rectal bleeding after radiotherapy. Int J Radiat Oncol Biol Phys 60:1589-1601.

120. Teh, B. S., L. Dong, J. E. McGary, W. Y. Mai, W. Grant, 3rd, and E. B. Butler. 2005. Rectal wall sparing by dosimetric effect of rectal balloon used during intensity-modulated radiation therapy (IMRT) for prostate cancer. Med Dosim 30:25-30.

121. Teh, B. S., J. E. McGary, L. Dong, W. Y. Mai, L. S. Carpenter, H. H. Lu, J. K. Chiu, S. Y. Woo, W. H. Grant, and E. B. Butler. 2002. The use of rectal balloon during the delivery of intensity modulated radiotherapy (IMRT) for prostate cancer: more than just a prostate gland immobilization device? Cancer J 8:476-483.

122. Teh, B. S., S. Y. Woo, W. Y. Mai, J. E. McGary, L. S. Carpenter, H. H. Lu, J. K. Chiu, M. T. Vlachaki, W. H. Grant, 3rd, and E. B. Butler. 2002. Clinical experience with intensity-modulated radiation therapy (IMRT) for prostate cancer with the use of rectal balloon for prostate immobilization. Med Dosim 27:105-113.

123. Paganetti, H., A. Niemierko, M. Ancukiewicz, L. E. Gerweck, M. Goitein, J. S. Loeffler, and H. D. Suit. 2002. Relative biological effectiveness (RBE) values for proton beam therapy. Int J Radiat Oncol Biol Phys 53:407-421.

124. Courdi, A., N. Brassart, J. Herault, J. M. Gabillat, D. Mari, J. P. Pignol, and P. Chauvel. 1996. Changes in biological effectiveness with depth of the Medicyc neutron therapy beam. Bull Cancer Radiother 83 Suppl:47s-49s.

125. Chen, M. E., D. A. Johnston, K. Tang, R. J. Babaian, and P. Troncoso. 2000. Detailed mapping of prostate carcinoma foci: biopsy strategy implications. Cancer 89:1800-1809.

126. Greene, D. R., T. M. Wheeler, S. Egawa, R. P. Weaver, and P. T. Scardino. 1991. Relationship between clinical stage and histological zone of origin in early prostate cancer: morphometric analysis. Br J Urol 68:499-509.

Vita

Adam David Melancon was born on July 25, 1981 to David Kent Melancon and Jacquiline Shortt Melancon in New Iberia, LA. He has one brother, Jared Scott Melancon, and one sister, Sarah Catherine Melancon. He grew up in Lafayette, LA where he attended Lafayette High School and graduated Valedictorian in 1999. Adam studied physics at Louisiana State University and graduated with a Bachelor's degree of Science in 2003. Adam enrolled in the University of Texas Graduate School of Biomedical Sciences in the fall of 2003 in the program of Medical Physics. He met Marites Pasuelo in graduate school; they were married in 2005 at St. Vincent de Paul Catholic Church in Houston, TX. In 2006, he completed his Master's degree of biomedical sciences in the Medical Physics program under the mentorship of Dr. Lei Dong. In April 2007, his daughter, Sophie Therese Melancon, was born. Adam completed his Doctorate of biomedical sciences degree in the program of Medical Physics in May, 2010. He currently resides in Houston, TX and anticipates beginning the Radiation Physics Residency Program at the University of Texas M D Anderson Cancer Center. In his spare time, Adam enjoys reading fiction, weightlifting, cooking, and playing poker. He also has a keen interest in martial arts, having studied shotokan, amateur wrestling, judo, brazilian jiu-jitsu, and thai boxing in the past.